Improving the detection, characterization and assessment of defective composites based on non-destructive measurements

By
Xiaonan Li

A thesis

Submitted to

The University of Liverpool

And

National Tsing Hua University

in accordance with the requirements of both the institutions for the degree of Doctor in Philosophy

March 2023

Abstract

This thesis summarises the research on the development of structural assessment of carbon fibre reinforced composites using non-destructive based techniques. Carbon fibre reinforced composites are widely used in the aerospace industry because of their high stiffness and low weight. However, the performance of composite parts is affected by defects induced during the manufacturing stage. The aim of this thesis is to improve the structural assessment of aerospace composites based on non-destructive measurements, such that defect identification in industry can be enhanced and better analysis of component failure can be achieved.

A novel technique for identifying defects in carbon fibre reinforced plates has been developed when investigating the resonance behaviour of defective composites with in-plane fibre waviness. Amplitude-fluctuation electronic speckle pattern interferometry combined with modal analysis were used to obtain the mode shapes of composite plates first. Then the contours of the nodal regions visible in the mode shapes were extracted using a specially developed algorithm based on density-based spatial clustering of applications with noise. Fourier descriptors were used to decompose the contours to reduce data dimensionality and make comparisons. The differences in contours can be used for identifying the presence of defects. This technique for nodal region comparison was found to greatly simplify the comparison of fringe patterns for the purpose of damage assessment and could potentially be used as part of validation procedures for finite element models.

This thesis also investigates the prediction of residual strains caused by fibre waviness using finite element models. Based on the prediction accuracy by comparing with experimental data, a novel method for identifying the most effective algorithm for characterising fibre orientation for the geometric ply map using ultrasonic C-scan data has been developed. Finite element models were generated based on the fibre-orientation data from three different algorithms: the Radon transform, 2D fast Fourier transform, and Sobel filter. Residual strains on the surface of the specimens were obtained from calculations based on the out-of-plane displacements measured using a digital image correlation system. The predicted and measured residual strain maps were decomposed into feature vectors using orthogonal polynomials to reduce data dimensionality and make quantitative comparisons.

The measured residual strains and the predictions based on models using optimised parameters showed good agreement. The differences in performance were quantified based on the accuracy of the predicted residual strains, which showed that the Radon transform performed best.

The performance of defective composites under mechanical loadings were investigated. Four severities of in-plane waviness were induced in composite specimens. The specimens were loaded to failure using four-point bending tests, and progressive changes in strain in both the bottom and top ply of the specimen during the tests were obtained using digital image correlation (DIC). For specimens with lower level of waviness, delamination was the dominant failure mode. For specimens with higher level of waviness, micro-buckling of carbon fibres occurred first at the defective regions then propagated through the surface of the ply under compression, and local delaminations were also observed. Finite element analysis was used to predict the failure behaviour. A cohesive zone model was used to model the delaminations and Hashin-Rotem damage criterion was applied via a UMAT (User Material Subroutine) to model the intra lamina failure. The model was shown to be effective for predicting the failure of different severities of waviness. The investigation on the delaminations and micro buckling behaviour is crucial for understanding the failure mechanism of composites containing in-plane fibre waviness. The results should also be useful in designing and repairing composite components with in-plane fibre waviness to prevent potential occurrence of such damages.

中文摘要（Abstract in Chinese）

本論文總結了應用非破壞性檢測技術對於碳纖維增強複合材料的結構分析。由於碳纖維增強複合材料具備了較高的強度和較低的重量，因此該材料被廣泛應用於航天領域。但是，在製造複合材料過程中引入的一些缺陷會影響到複合材料部件的在實際應用中的表現。本論文的研究目的爲應用非破壞性檢測技術改善對航天複合材料部件的結構分析，以此來改進對缺陷在工業界內的檢測方法和提高對部件破壞行爲的分析手段。

本論文研發出一項創新的技術可以用來檢測碳纖維增強層壓板內的缺陷。這項技術的實現基於對含有面內波紋缺陷的共振行爲的研究。首先，振幅變動電子光斑影像干涉術和模態分析法結合起來獲取到了複合材料層壓板的振型。其次，在振型中可識別的節線區域的輪廓線被提取出來。提取輪廓線應用了專門爲此編寫的一套算法，該算法基於密度空間的聚類分析（Density-based spatial clustering of applications with noise）。傅裏葉描述子被用來分解提取到的輪廓線，以此來降低數據維度和進行數據對比。振型輪廓線的區別被用來識別缺陷是否存在於碳纖維層壓板內。這項對比節點區域輪廓線的技術可以極大地簡化條紋圖像的對比，來達到損傷檢測的目的。這項技術在驗證有限元模型的有效性方面同樣顯示出很大的潛力。

本論文也探討了應用有限元模型進行預測波紋缺陷導致的殘餘應變的研究。有限元模型預測的準確性可以通過與實驗數據進行對比得出。在此基礎上，本論文發明了一項創新的方法用來識別對超聲波 C 掃描數據進行處理的最佳算法。這些算法可以通過表徵超聲波 C 掃描數據獲得碳纖維的方向，以此來繪製出纖維取向圖。有限元模型的建立基於纖維取向圖，而纖維取向圖可以通過三種算法得到，分別是：拉冬變換（Radon transform）, 二維快速傅裏葉變換（2D fast Fourier transform），和索貝爾濾波器（Sobel filters）。試樣表面的殘餘應變可以通過對試樣在靜態下的面外位移的計算得到，面外位移可以通過數字影像相關法測量得到。模型預測得到的殘餘應變圖與實驗得到的殘餘應變圖可以被正交多項式分解成特徵向量來降低數據維度和進行量化對比。實驗數據與應用到優化參數的模型預測結果符合程度良好。通過對三種算法得到的有限元模型的預測表現進行對比，拉冬變換（Radon transform）表現最佳。

本論文研究了有缺陷的碳纖維層壓板在受力情況下的表現。四種不同程度的缺陷被引入到試樣中。通過四點彎折實驗，這些試樣被折斷。數字影像相關法（DIC）測量得到了在加載過程中試樣的上、下表面產生的逐漸變化的應變。對於含有少量缺陷的試樣，分層損傷是主要的破壞方式。對於含有大量缺陷的試樣，碳纖維的微屈曲先在缺陷區域發生，然後在受力面是壓應力的板層進行擴展，與此同時局部的分層損傷也會產生。有限元模型被用來預測斷裂行爲。內聚力模型被用來預測分層損傷，哈辛-羅特姆（Hashin-Rotem）斷裂準則應用到了 UMAT（用戶自定義材料子程序）裡來模擬層內損傷。該模型有效地預測了含有不同程度缺陷的複合材料的斷裂行爲。這項關於分層損傷和微屈曲的研究對於了解含有面內波紋缺陷的複合材料的斷裂行爲至關重要。這些研究成果對於設計和維修含有面內波紋缺陷的複合材料部件來阻止上述斷裂行爲的產生也很重要。

Acknowledgements

First and foremost, I would like to express my gratitude to my supervisors Dr. William Christian, Professor Eann Patterson and Professor Wei-Chung Wang for their support, encouragement, and guidance through the years I have spent at the University of Liverpool and National Tsing Hua University. Their insightful comments and suggestions are indispensable for me to become an independent researcher.

Also, I would like to thank Dr. Khurram Amjad, Dr. Po-Yu Chen and Dr. Po-Chi Sung for teaching me how to use the equipment. I am grateful to Jiji Mathews for his assistance during my experimental work. Thanks to Dr. Chi-Hung Hwang for his suggestions on ESPI analysis. I would also like to thank Eric Chai for his help in preparing some specimens.

I have received a scholarship from University of Liverpool and National Tsing Hua University, and I am grateful to both universities for their financial support.

Finally, I would like to thank my families, without their love, support and understanding I would not finish my study. Special thanks given to my wife, Fei Guo, who dedicated to taking care of the families while I am studying abroad. Additionally, I am grateful to my son, Zhi Li, for his understanding and support during this time, despite not being able to spend as much time together as I would have liked.

Table of Contents

List of Figures

List of Tables

1. Introduction

1.1. Background

The advances in materials have boosted the development of modern technology. Engineers and scientists have been endeavouring to invent new materials to satisfy the increasingly challenging industrial requirements. Traditional materials, such as metals, ceramics and polymers are becoming less competitive compared to their new counterpart: composites. A composite material consists of two or more materials forming a structural unit, which enables it to outperform traditional materials. This is because a composite has better properties arising from the combination of its constituents than can be achieved by any one of the constituents alone. Natural composites, e.g., wood, bone, and man-made ones in ancient times, e.g., clay with straws, have something in common with modern composites because they contain a 'matrix' reinforced with 'fibres' that give them superior properties. This provides inspiration for researching and designing advanced composites. In the early 1930s, glass fibre was invented by Games [1] from Owens Illinois Glass Company. This invention laid the foundation for a new type of popular composite, known as fibre reinforced polymers in the later decades. With the commercialisation of unsaturated polyester resin in the 1940s, glass fibre reinforced polymers were widely recognised for their outstanding properties and thus were utilised in the aerospace industries for manufacturing the fuselage and wings of airplanes. Later in the 1960s, one alternative material for replacing glass fibre in composites was discovered: carbon fibre. In comparison with glass fibre, laminates reinforced with carbon fibre can be more than three times stronger but with 20% lower weight [2]. Despite a higher manufacturing cost, carbon fibre is gradually replacing glass fibre in the aerospace industries. In the recent two decades, due to the improvement in processing and synthesis technology, carbon fibre has also been successfully used in many civil applications: sports equipment, wind turbine blades, automobiles, pressure vessels, etc.

Carbon fibre reinforced polymers have been used extensively in the aerospace industry due to their relatively high specific strength. In addition to good mechanical properties, they can also have good corrosion resistance and electrical and thermal insulation properties. Using carbon fibre reinforced composites can greatly reduce the weight of aircraft, therefore increasing the fuel efficiency and saving energy costs. To satisfy industrial demands,

appropriate designs of carbon fibre reinforced polymer (CFRP) structures need to be carefully considered. However, it is commonly found in industry that even after the correct design has been selected and applied, properties of the manufactured CFRP components are often lower than desired. Defects such as: voids [3], disbonds [4], delaminations [5] and cracks [6] introduced during the manufacturing process are often the cause. Apart from the aforementioned defects, there is a growing awareness that the misalignment of fibres, often referred to as fibre waviness, can also lead to significant reductions in strength. Therefore, fibre waviness was selected as the type of defect to be investigated in this thesis. Fibre waviness is defined as occurring when some fibres deviated from its designed placing directions in the manufacturing process. There are two types of fibre waviness: in-plane and out-of-plane fibre waviness. The former type is formed within a plane, while the latter type is formed in the thickness direction of a laminate, also known as wrinkles. Fibre waviness can act as an initiation site for damage that may lead to total failure. Thus, components with fibre waviness often have a lower strength than expected. Although fibre waviness causes a reduction in strength and influences the performance of composite components, the onset of the first damage and the following failure mechanisms of defective components subjected to load are not fully understood.

Characterisation of fibre waviness is crucial for investigating the failure behaviour of composites. Researchers in the past used visual inspection and optical microscopy to perform characterisation, it is popular nowadays to use non-destructive techniques to characterise waviness defects. Three commonly used non-destructive techniques are: ultrasonic inspection, eddy current testing, and X-ray computed tomography. They all performed well in providing accurate fibre orientation results without destroying the specimens being inspected. Considering the ease-of-use, efficiency and safety reasons, ultrasonic inspection was selected in this study to characterise the waviness defects. Christian et al. [7] applied pulse-echo ultrasonic inspection to characterise in-plane fibre waviness and they found that residual strains correlated well with the ultimate strength of the material. This thesis extends their findings by developing better algorithms to process ultrasound data and importing the results into finite element models to predict residual strains and failure behaviour. The optimised algorithms are also useful for understanding the mechanism of the initiation and propagation of damage in composites.

Digital image correlation(DIC) and electronic speckle pattern interferometry(ESPI) are two non-contact techniques for performing displacement measurements. The two techniques can provide full-field measurements of displacement and deformation for objects under various loading conditions thus are helpful in investigating the failure behaviour of composites subjected to load. Damage analysis is performed by conducting strain assessment from measurements of DIC. It will be the first time that DIC is used to analyse the micro buckling failure mechanism caused by a high level of in-plane fibre waviness in defective CFRP laminates. ESPI is widely used for taking displacement measurements for objects under vibration loads, thus mode shapes can be obtained. Wang et al. [8] applied ESPI to obtain mode shapes from defective CFRP plates under a vibration load at various resonant frequencies, and identified pre-embedded delaminations by visually inspecting the change in fringe patterns. This thesis extends their method for identifying a different defect, fibre waviness in composite plates. However, a technique is needed for quantitatively analysing the difference in fringe patterns between defective and defect-free plates to reveal the severity of the defect. This thesis develops such a technique that can discern even a minor difference caused by waviness defects, which is believed to be applicable to detect other types of defects.

1.2. Aim and Objectives

The aim of this thesis is to develop experimental and numerical techniques to improve the detection, characterisation, and assessment of defective composites, with the focus on fibre waviness. To achieve this aim, three objectives were set:

- Develop a non-destructive technique for identifying and quantifying the severity of defects in composites.
- Develop a method for better utilising non-destructive evaluation data for characterising defects in composites.
- Enhance the assessment of the performance of defective composite components subjected to loads.

2. Literature Review

This chapter is a review of literature related to assessing composites with defects both experimentally and numerically, with the focus on fibre waviness. The chapter is split into six sections. The first section focuses on the formation and effects of fibre waviness. The second section reviews characterisation techniques of defects in composites. The third section covers reviews of non-contact measurement techniques. The fourth section focuses on fracture and failure criteria for composites. The fifth section reviews shape descriptors for representing images. Knowledge gaps are identified in the sixth section.

2.1. Formation of fibre waviness and its effect

Fibre reinforced composites are widely used in the aerospace industry and other high-tech fields due to their relatively high specific stiffness and strength. A typical continuous fibre composite consists of multiple laminae stacked with a pre-determined sequence to achieve desired properties. Each lamina consists of reinforced fibres embedded in a matrix material, in which the fibres strengthen the lamina in the direction in-which they have been placed and the matrix plays a role in holding the fibres together and protecting them from external damage. The reason for using multiple laminae is that a lamina is strong in the longitudinal direction where fibres are aligned, but weak in the transverse direction. Thus, several laminae need to be stacked with a designed sequence to form a structural unit that can achieve balanced properties in all the desired directions. Based on classical lamination theory, once the materials for a composite laminate are selected, the properties of the laminate are determined by the ply orientations and stacking sequences of the plies [9]. However, not all fibres can be ideally placed in the designed direction neither within a ply nor in the thickness direction of a laminate during the manufacturing process. Specifically, the former type of misorientation of fibres is known as in-plane fibre waviness and the latter is out-of-plane fibre waviness. Fibre waviness plays a major role in influencing the mechanical performance of composites, hence is the focus of this thesis.

The formation of fibre waviness is closely related to the manufacturing process in industry. In a recent comprehensive literature review, Kulkarni et al. [10] summarised four mechanisms of fibre waviness formation in continuous-fibre composites. The first mechanism is that the formation of fibre waviness is a result of thermal stress, and this stress can lead to

a local thermal distortion, which can become a source of fibre waviness [11]. It has been reported by Parlevliet et al. [12] that thermal stress in composites can be divided into three levels: micromechanical, macro-mechanical and global. In the micromechanical level, a thermal stress may arise due to the difference in thermal expansion coefficients between the fibre and the matrix. In the macro-mechanical level, a thermal stress can form due to the difference of thermal expansion coefficients in the longitudinal and transverse direction of a lamina. In the global level, the cooling speeds for the surface and the core of a laminate are different, and this gradient in cooling speed may lead to a thermal stress. The second mechanism for forming fibre waviness is that for composite components under compressive consolidation, excess pressure applied on the components may cause inter-ply friction to exceed a limit causing out-of-plane fire waviness be created. In-plane fibre waviness may also be created due to an excess resin pressure when resin transfer moulding process is applied [13]. Excess resin pressure causes a rapid resin flow during the resin transfer moulding process, which may lead to undesired fibre waviness. The third mechanism is similar to the first mechanism, the difference is that for the third one, discrepancies of thermal expansion coefficients may exist between the tool and component being manufactured. Thus during the cooling stage, volume shrinkage is different for the tool and the component, which may lead to the creation of fibre waviness. The fourth mechanism is that buckling of continuous fibres may occur when they are forced to form a curved shape, resulting in fibre waviness. Based on the formation mechanisms of fibre waviness, it is evident that fibre waviness is inevitable during the manufacturing process of a composite component. For instance, it is impossible to fully eliminate the difference in thermal expansion coefficient between fibres and a matrix in composites, or between a composite component and a tool. Therefore, instead of being treated as a type of defect, fibre waviness is often considered to be an unavoidable feature in composites. Hence, the tolerance of fibre waviness depends on establishing evaluation criteria for judgment about whether to accept or reject a composite part, which brings forward the necessity to investigate the effects of the defect.

Over the past three decades, numerous studies have adopted analytical, numerical, and experimental methods to investigate the effects of fibre waviness. It has been well acknowledged that fibre waviness leads to reductions in mechanical properties and correlates with failure initiation. The magnitude of performance reduction varies with the property

types and the tests that have been undertaken. One early study of the effects of fibre waviness on stiffness and strength can be dated back to 1992, when Bogetti et al. [14] reported that the geometric shape of fibre waviness correlated with mechanical properties reduction. Their findings were based on an analytical model using sinusoid waves to represent waviness shapes, where the amplitude and half wavelength of a sinusoid were used as two primary geometric parameters. A 60% reduction in the Young's modulus in the longitudinal direction was observed in a graphite composite with some cases of fibre waviness. However, Young's modulus in the transverse direction, Poisson's ratio, and in-plane shear modulus were not affected significantly. Uniaxial compression and biaxial compression tests were performed to investigate the strength reduction. A maximum of 65% reduction in the compressive strength was found for the uniaxial tests and a maximum of 35% compressive strength reduction in the longitudinal direction was observed for the biaxial tests. However, compressive strength in the transverse direction for the biaxial tests was barely affected.

In 1996, a similar analytical model was developed by Hsiao and Daniel [15], who also used sinusoidal waves to represent the physical shape of fibre waviness. Amplitudes and wavelengths of the sinusoidal waves, combined with classical lamination theory, were used to deduce expressions of Young's modulus, Poisson's ratio, and shear modulus. It was found that the calculated properties based on the analytical model matched well with the properties obtained from tests. The researchers also reported that the Young's modulus in the longitudinal direction decreased significantly in the unidirectional composites with the increase of fibre waviness. However, this property was less affected by fibre waviness in the cross-ply composites, which shows that the stacking sequence of defective composites with fibre waviness should not be overlooked.

One attempt at using finite element models to investigate the effect of fibre waviness was conducted in 2004, when Garnich and Karami [16] developed a micromechanical model based on a unit cell consisting of unidirectional waved fibres embedded within matrix. The fibres were packed hexagonally in the unit cell, and the geometric shape of the unit cell was a sinusoidal shape with the wavelength and amplitude as variable parameters. The researchers reported that the major influence of fibre waviness was on the axial properties, i.e., the Young's modulus in the longitudinal direction. The model could also predict local stresses when performing a structural analysis, which is crucial for predicting failure. The

methodology of using sinusoidal functions representing waviness shapes has also been taken by Zhu et al. [17] in 2015, who developed similar analytical models to investigate the relationship between fibre waviness and properties. Their findings confirm that Young's modulus in the longitudinal direction significantly decreases with the increase of fibre waviness and the effect of fibre waviness on properties varies with different stacking sequences. However, they observed a significant increase of shear moduli in the plane perpendicular to the transverse direction with the increase of fibre waviness, which may be helpful in designing an ideal laminate. They also discovered that the effect of fibre volume fraction on the stiffness of defective composites with fibre waviness is barely noticeable. While their work has shown the effect of different parameters of fibre waviness on mechanical properties using analytical models, the results lack experimental validations.

Investigations of the dynamic response of defective composite laminates with fibre waviness have been focussed mostly on the resonant behaviour. Studies have shown that natural frequencies and vibration modes of unidirectional CFRP laminates change with different fibre orientations, e.g. 0°, 45° and 90°, and that the change in the stiffness of the laminates was the main cause [18]. Similar findings in [19] show a reduction in resonant frequencies of the first two modes for laminates made of glass fibre reinforced polymers, due to an increase in fibre orientation from 0° to 90°, when five fibre orientations were investigated: 0°, 30°, 45°, 60° and 90°. These findings consider the effects of specific fibre orientations, but fibres with random alignments, such as when fibre waviness is present, have not been experimentally studied. The most recent work conducted to investigate the effect of fibre waviness on vibration behaviour was in [20], where using analytical and numerical methods, it was found that fibre waviness caused a reduction in resonant frequencies for certain modes. This effect was predicted to be more significant if the waviness defect occurred in the plies that contributed more to the stiffness of the laminate. They also found that bending modes are more susceptible to waviness defects that occurred in the 0° ply. However, whether the mode shapes of CFRP components would be affected by fibre waviness has not been explored in any research.

It is important when investigating the effect of fibre waviness in a laboratory to be able to reproduce defined levels of waviness. One technique is to stack prepreg over a glass rod to create out-of-plane waviness, and then roll the uncured laminates on a flat surface to

produce in-plane fibre waviness [21]. Another method involves a two-step forming process [22]: first, a V-shape is created in the central region of a laminate by compression moulding; and second, the laminate is flattened in a hot press. In-plane fibre waviness can also be created by laying up prepreg on aluminium formers with various arc shapes, and then flattening them manually before curing [7]. The arc shapes of the aluminium formers controlled the levels of fibre waviness that were induced into composites. This is because when a prepreg laid up on an aluminium former with an arc shape, a length difference was created between the bottom plies and the topmost ply. Once the prepreg was flattened on a flat surface with a minimal force provided manually, fibres in the topmost ply buckled to compensate for the length difference. This buckling of fibres created in the topmost ply of the prepreg was maintained after curing, from which in-plane fibre waviness was formed. The nominal waviness level was controlled by two parameters, which are the arc radius of the aluminium formers and the uncured laminated thickness. This method described in [7] is more flexible in creating different levels of fibre waviness with an ease.

2.2. Characterisation techniques for defects in composites

Characterisation of defects in composites is essential for quality control and design purposes. There are techniques for characterising defects in composites such as voids [3], disbonds [4], delamination [5], and cracks [6], and some of the techniques for characterising these defects are also suitable for fibre waviness. However, characterisation of fibre waviness has never been an easy task as the scale of fibre size is small and there exists uncertainties and measurement errors that cannot be overlooked, especially for low degrees of fibre waviness with random orientations. Conventionally, characterisation of orientations of single fibres is not practical as fibres are often bundled together in fibre tows. Therefore, to obtain the orientation distribution of fibre waviness experimentally, the orientations of the fibre tows in the localised defective regions is often the focus. Characterisation of fibre orientations can be divided into two steps: the first step is obtaining raw image data with techniques that can interact with composites optically, electrically or acoustically in order to “capture” the morphology that contains orientation information of fibres; while the second step is applying various image processing algorithms to reveal fibre orientations from these image data.

In 1987, Yurgartis [23] developed a technique that can determine the fibre angle distributions using microscopy. In his research, a plane was cut at a small angle of 5 ° with

respect to the mean fibre direction, leading to the cross-sections of fibres at the sectioned plane appeared to be ellipses. The fibre angle distribution was then calculated by measuring the major axis of the ellipse at the sectioned plane and the fibre diameter. Although it provides a method to measure the misalignment angles of fibres, the disadvantages are that specimen preparation and manual data collection are time consuming, and the method can only provide fibre orientation without giving the morphology of fibre waviness. Furthermore, for determining the fibre orientations, this technique destroys the specimen.

Creighton et al. [24] developed a method called multiple field image analysis (MFIA) in 2001, which is an image analysis algorithm that can determine the fibre misalignment angles. The images were obtained using an optical microscope to view the surfaces of specimens which were ground and polished first to achieve a good contrast of fibres and matrix. The dark elongated features in the images were considered to represent bundles of fibres or matrix between fibres. The images were divided into a number of facets that covered the entire field, and a 1-D pixel array of a certain length was created that superimposed on each facet. Light intensities were sampled along the pixel arrays. By rotating a facet through a series of angles and calculating the light intensity variation of the pixels in the facet superimposed on the induced pixel array, a minimum light intensity variation can be identified. The fibre orientation in a facet thus was identified at the rotation angle when a minimum light intensity variation was achieved, which means that most of the fibres within the facet of interest were parallel to the induced pixel array, as shown in Figure 1. This method is believed to be applicable to a large volume of composites with relatively low magnification photographs, but the preparation of specimens with good contrast is destructive as grinding and polishing of the specimens are required. Additionally, the effect of pixel array length and facet size is not fully understood.

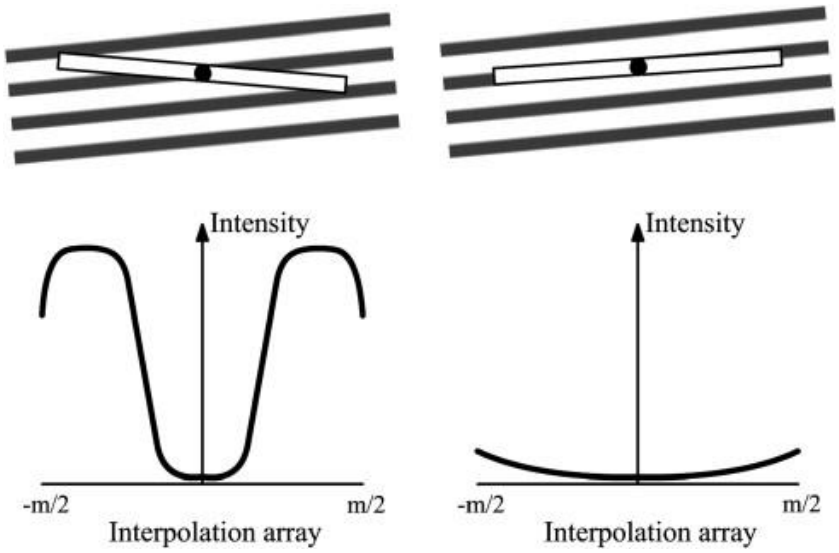

Figure 1: Intensity distributions along two interpolation arrays with different angles relative to the fibre orientation. The more parallel an interpolation array is to the fibre orientation the smaller the intensity variation [24].

Sutcliffe [25] improved the MFIA algorithm by boosting its calculating efficiency and increasing the accuracy of the results. They applied an autocorrelation function on the data processed by MFIA, which can characterise the width and length of a waviness region. The algorithms were applied on images obtained from a microscope and a micro-CT X-ray imaging system. The characterised waviness based on both techniques show a good agreement. The MFIA algorithm has been further improved by Kratmann et al. [26], who combined the 2D fast Fourier transformation (FFT) with MFIA to characterise the misalignment of fibres. The micrograph of a polished section of a specimen contained much noise affecting the accuracy. Therefore, the FFT was used to transform the section from the spatial domain to frequency domain to filter out the noise. They also applied an object filter to remove short objects from the section to further improve the image quality for applying the MFIA. The short objects in the images could be the fibres that were not fully revealed by the polishing process of the specimen, leading to part of the fibres being captured by the imaging system. The computation time and memory usage has been reduced greatly without losing accuracy using the two algorithms combined.

The methods discussed previously are mostly based on optical microscopy. The advantages of using an optical microscope are that the equipment is available in most laboratories and operating procedures are user friendly, while the drawback is that it requires well prepared specimens, normally grinding and polishing of the surface of the specimens are

necessary for good quality images. Therefore, optical microscopy is often considered as a cumbersome technique unsuitable for processing large quantities of composite specimens or complex components. X-ray computed tomography, eddy-current testing, and ultrasonic testing are three widely used non-destructive methods for characterising fibre orientation. X-ray computed tomography can provide images of the 3D microstructure of a specimen from which waviness can be measured [10]. However, it is difficult to distinguish some fibres, such as carbon fibres, from the resin matrix as the fibres and the matrix often have similar radiodensities [27]. Eddy-current testing can be utilized to characterise the fibre orientations based on the directional electrical conductivity of CFRP material [28], and both in-plane and out-of-plane fibre waviness can be detected by the technique [29]. However, eddy current testing has two significant limitations: the measured signal is difficult to interpret, and the lift-off effect needs to be considered [30]. Ultrasonic C-scans can also be used to measure the fibre orientation and ply stacking sequence [31]. The feasibility and easier applicability of ultrasonic testing make it a favoured method in industry to characterise fibre orientation.

In comparison with the algorithms based on MIFA, there are some other image analysis algorithms that can be used to characterise fibre orientations. The most commonly applied algorithms are the Radon transform (RT) [32] and 2D fast Fourier transform (FFT) [33]. These algorithms have been successfully applied to characterising fibre orientation in: optical micrographs [34], electron microscopy images [34], eddy-current testing images [35], and ultrasound images [31]. Comparisons of the two algorithms were made by Hughes et al. [35], who concluded that the RT outperformed the FFT. The reason for this finding was that RT can generate sharper orientation peaks and had a higher computational efficiency in image processing than FFT. Schaub et al. [36] also compared the two algorithms, and found RT was a more stable function for analysing fibre alignment as it had less noise and could assess smaller changes in fibre alignment than FFT. When applying RT and FFT for image processing, facet size is an important parameter that controls spatial resolution, but analysis of an appropriate facet size for characterisation of fibre orientation has not been considered by any of the prior research. Gabor filters have also been implemented to process the ultrasound data to generate fibre orientation map, which is found to be more noise resistant than RT [37]. However, due to the large number of filters required to form a Gabor filter bank, the computation time is much higher.

To summarise, the potential methods that can be used in characterising fibre waviness in CFRP specimens are: Yurgartis's techniques, multiple field image analysis (MFIA), Fast Fourier Transformation (FFT), and Radon Transformation (RT). The above techniques can be applied to images from optical microscopy, scanning electron microscope (SEM), X-ray computed tomography, ultrasonic testing and eddy-current testing. Ultrasonic testing is considered to be the best option as it is: non-destructive, can provide 3D information and has easier applicability. FFT and RT appear to be the two optimal techniques for characterising fibre waviness considering their accuracy and computing time. However, the comparisons of the two algorithms in performance have not been made quantitatively in the studies.

2.3. Non-contact measurement techniques

The measurement of response from a structural material under different loading conditions is important for determining its properties and evaluating its performance. Non-contact techniques have become very popular recently to perform these measurements. Without physically touching the objects being measured, non-contact techniques are able to perform measurements on objects that are sensitive to pressures, and the measured data normally provides full-field information. Among the rising non-contact techniques that have been developed in the last half century, digital image correlation (DIC), and electronic speckle pattern interferometry (ESPI) are two popular ones that have been used significantly in studies.

DIC was firstly proposed in 1983 by Sutton et al. [38], when they developed a digital correlation algorithm that can be applied to comparing two digital images before and after loading to calculate surface deformations. The algorithm has improved rapidly since then and now it has been adopted by many researchers in both the academic and industrial fields. The principle of DIC is to correlate digital images recorded before and after deformation to calculate displacements. The correlation is based on tracking a subset of the images, which requires each subset to be assigned unique features that can be distinguished from one another. A pattern is created by spraying background paint on the surface first and then creating distinct speckles, so that the grey scale of every subset in the images varies. Full-field measurements can be obtained by tracking the subsets before and after deformation. The tracking process is shown in Figure 2 [39]. Figure 2(a) shows a reference subset image, and Figure 2(b) shows a deformed image of the same subset. The reason for selecting a square

subset instead of an individual point is because a subset of points is more distinctive and easier to track. By predefining the matching criterion, e.g., cross-correlation criterion or sum-squared difference, the same subset in the deformed image can be correlated and its displacement can be calculated [40].

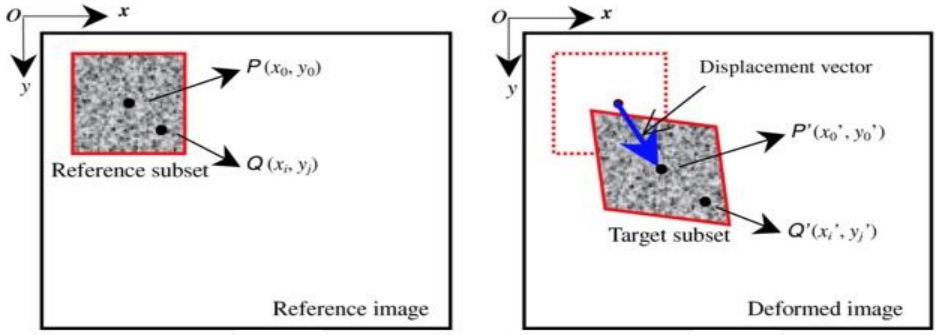

(a) (b)

Figure 2: (a) Reference image of a subset for DIC analysis; (b) Deformed image of the same subset for DIC analysis [39].

DIC can be used to measure both in-plane and out-of-plane displacement, from which strain calculations can be performed. This makes DIC a very suitable tool in fracture mechanics of composites based on displacement or strain assessment. Catalanotti et al. [41] developed a method to calculate the crack resistance curve for carbon fibre reinforced composites. The curve has been correlated with the fracture toughness and used to identify parameters of softening laws. In their research, DIC was used to measure the displacement jump associated with crack propagation during compact tension and compact compression tests to locate the crack tips. The strains calculated based on DIC measurements were used to deduce the J-integral, which was combined with crack length to generate resistance curves in real time for the tests. The results calculated using DIC matched well with those obtained from numerical methods using finite elements analysis. Unfortunately, this method did not work properly when dealing with failures associated with delaminations.

Godara and Raabe [42] used DIC to measure the strain distribution for composites with two fibre orientation lay-ups at eight stages during tensile tests. They found that for composites with fibre orientations of 0°/90°, the strain distribution was heterogeneous at each tensile stage. However, for composites with fibre orientations of ±45° there was a transformation of strain distribution from homogeneous to heterogeneous. The reason for this phenomenon was because at the initial stage of testing, transmission of the loads was

fibre dominated for the 0°/90° case while was matrix dominated for the ±45° case. This theory was confirmed by fractography of the composites using a scanning electron microscope (SEM). The findings reveal the effect of fibre orientations on the strain distribution and fracture morphology when carrying a tensile load. Their methods show that DIC is a useful tool for measuring full-field strains simultaneously while performing tests, which is important for understanding the failure mechanism of composites.

DIC equipped with high-speed cameras can enable full field measurement of displacement during fast events. This can greatly enhance its ability in analysing the damage occurrence and evolution in composites, as crack propagation speed in composite can be as fast as the speed of sound [43]. Sun and Hallett [44] used three DIC systems with four standard cameras and two high-speed cameras to investigate the damage initiation and evolution in composites subject to compression tests. The composite specimens had been impacted to induce barely visible impact damage into them prior to the compression tests. The two standard DIC systems were used to take measurements from both the front and back surface, while the high-speed DIC system was used to obtain the deflection of either the front or the back surface at the instant when the fracture occurred. It was shown that when the frame speed was set to 30,000 fps, the high-speed DIC system captured the local buckling band growth over a time interval of 0.06 ms. The experimental results matched well with those from simulation using finite element analysis, which showed that DIC measurements can be used for quantitative validation of model predictions. One limitation for their investigation is that only one high-speed DIC system was employed to analyse one side of the specimen, therefore whether it was the growth of the buckling band on the front surface or the back surface that triggered the final failure could not be understood.

Electronic speckle pattern interferometry (ESPI) is a non-contact and full-field measurement technique that can be used to measure small displacements with a high spatial resolution [45], with the sensitivity of measurement of the order of tens nanometres [46]. The invention of ESPI for displacement measurements dates back to the 1970s, when Leendertz [47] pointed out that when a surface was illuminated by a highly coherent light, e.g. a helium-neon laser, a speckle pattern representing the distribution of light intensity can be obtained. The intensity was determined by the amplitude and phase of the light. If two speckle patterns were superimposed, the summed pattern contained information of the

relative phase of the two light waves. Displacement measurement can thus be performed by recording the change in the relative phase before and after deformation, as this change is correlated with the deformation. An exemplar ESPI set-up for measuring out-of-plane displacement is shown in Figure 3 [48]. The interference of the object and reference beam shown in Figure 3 can generate a speckle pattern. By subtracting the speckle pattern after deformation from the speckle pattern before deformation, a fringe pattern representing the surface contour of out-of-plane displacements can be obtained. Similarly, by changing the arrangements of the optical components, in-plane-displacement can also be measured.

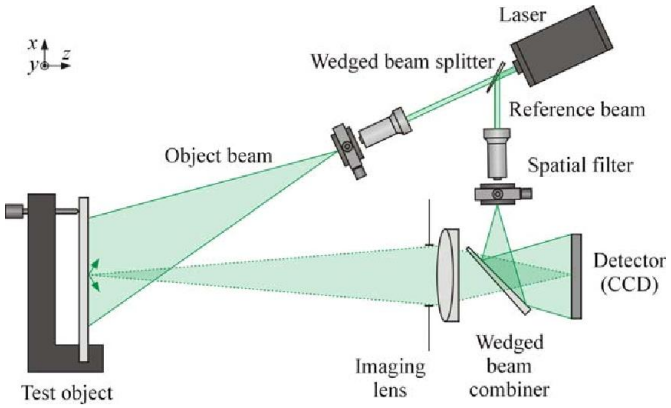

Figure 3: Electronic speckle pattern interferometry set-up for measuring out-of-plane displacement [48].

An early attempt at strain measurement using ESPI was made by Moore and Tyrer [49] in 1994, when they developed a novel method to measure in-plane displacements in two directions simultaneously. The in-plane normal strains and shear strains could thus be calculated from the measured displacements. Four beams from the same laser source were adopted in their method, where two beams were paired to measure displacement in the horizontal direction and the other two were paired to measure displacement in the vertical direction. The splitting of the four-beam system into two two-beam systems was achieved by using a polarizer, which enabled the first two beams to be orthogonally polarized to the second two beams, therefore speckle patterns obtained from each pair were separated. The accuracy of the displacement measurements was ±0.03 μm, while for the strain measurement it was ±6 με. The measured strain distribution matched well with those obtained from analytical solutions.

ESPI can also be used to detect damage. In 1998, Zhang et al. [50] reported that both fringe patterns and phase maps obtained using ESPI revealed the location and area of internal damage in composite plates. The detection process included impacting the composites plates to induce damage first and exciting the damaged plates mechanically with a hammer subsequently. ESPI was then used to measure the out-of-plane displacements during the excitation process. Phase maps were extracted from the intensity fringe patterns using a phase-stepping method. The method was developed using a piezoelectric transducer to move a mirror a precise distance in the reference beam to create three intensities, which were used to calculate the optical phase. The intensity fringe patterns showed the damage in real time but with noise, while the phase maps were able to provide non-real-time detection with noise-free results. The detection results from ESPI were compared with ultrasonic inspections and a sectioning technique, which showed a good agreement. The researchers claimed that the technique could also be used to quantify the level of damage. Similarly, Pagliarulo et al. [51] investigate the possibility of using ESPI to identify delaminations in composites. In their research, a composite specimen was first subjected to a three-point bending load and then analysed by the ESPI technique. Prior to performing the displacement measurement using ESPI, a thermal load was applied to the specimen to create a perturbation. Both the abnormal fringe pattern and unwrapped phase map indicated the existence of delaminations. It was believed that the technique could also be used for detecting micro-cracks and residual stresses.

Apart from measuring displacement under static conditions, ESPI is also popular in measuring the dynamic surface displacements when investigating the resonant behaviour. The high spatial resolution enables ESPI to measure the vibration mode shapes of materials in real time. Time-averaged ESPI has been used to obtain mode shapes of a vibrating plate, which were compared with results from analytical methods and showed good agreement, but the authors noticed a decrease in contrast for some fringes [52]. Both the visibility and spatial resolution of the fringe pattern can be significantly improved when using amplitude-fluctuation electronic speckle pattern interferometry (AF-ESPI) [53]. For vibration measurement, AF-ESPI differs from normal ESPI in taking the reference image at a vibrating state rather than the stress-free state. The quality of fringe patterns can be further improved by also using radial basis functions as a pre-filtering method to remove noise [54]. AF-ESPI has

been used to identify pre-cut square and circular defects in composite plates based on changes in mode shapes, with the effects of the defects being more visible in the fringe patterns for higher modes [8]. Interfacial cracks can also be detected using AF-ESPI by comparing the fringe patterns of specimens with and without defects [55]. Whilst these studies could identify defects by comparing fringe patterns for defective and non-defective specimens, these comparisons were made qualitatively.

To summarise, DIC and ESPI are two non-contact techniques to measure both in-plane and out-of-plane displacements. DIC equipped with high-speed cameras can be used to analyse a transient process. AF-ESPI is an improved way of performing ESPI analysis, which is often used to detect defects in composites. However, the detection based on the comparison of fringe patterns between defective and non-defective specimens is made qualitatively rather than quantitatively.

2.4. Fracture and failure analysis for composites

2.4.1. Failure modes

Fracture and failure analysis in composite laminates is complicated due to composites being made of two or three different materials, and each material behaves differently under load. Nevertheless, the failure of continuous fibre reinforced laminates can be classified into two modes: intralaminar and interlaminar. Intralaminar mode include failures that occur and propagate within a ply, such as: matrix damage, fibre breakage, fibre pull-out, fibre kinking, fibre debonding etc. While the interlaminar mode is mainly about delamination that occurs and propagates between plies causing the adjacent plies to detach from each other. One exemplar micrograph of the two failure modes including three failure types is shown in Figure 4 [56].

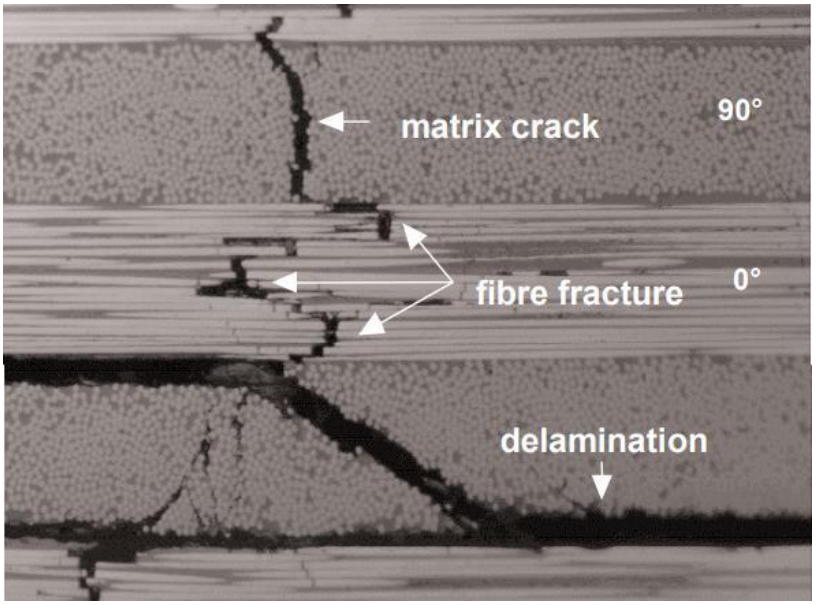

Figure 4: Two failure modes including three failure types in composite laminates [56].

The failure behaviour of defective laminates with fibre waviness has aroused a growing academic interest in recent years. In 2015, Mukhopadhyay et al. [57] investigated the compressive failure behaviour of laminates with out-of-plane fibre waviness. Three levels of out-of-plane waviness were created by varying the thickness and width of the inserted strips between plies to induce the defects. The tangential angle of the wavy plies was used to quantify the severities of the waviness defect, which were 5.6°, 9.9°, and 11.4° respectively for the three levels. A high-speed camera was used to capture footage of the failure events at one edge of the specimens. The compressive test results indicated that failure progression was different for the three levels of defective specimens. For the specimens with the lowest fibre waviness, fibre failure occurred first in the axial plies due to the compression load exceeding a critical value, which then led to delaminations and matrix cracks in the adjacent plies. While for the other specimens with higher levels of fibre waviness, transverse cracks and delamination in the 90° plies occurred first and then led to the fibre failure in the axial plies. The failure behaviour was verified by numerical analysis using finite element models. It was also noted that there existed a threshold severity represented by the tangential angle of the wavy plies. The failure modes changed according to the severity of defects. Exactly the same method for inducing out-of-plane fibre waviness into laminates was adopted in [58], where failure behaviour was investigated for defective laminates having three levels of waviness defect subject to tensile loads. In comparison with [57], there were no differences in the failure mode for specimens with different levels of waviness. All the specimens

experienced a matrix failure first and then the matrix crack propagated with increasing tensile load. Surface split and delaminations occurred afterwards.

The effect of in-plane fibre waviness on the compressive properties of composites was investigated by Sitohang et al. in 2021 [59], when they found that effect of in-plane fibre waviness on the global laminate stiffness was negligible. However, they pointed out that the waviness defect led to the initiation of damage and the subsequently formed kink band was the dominant failure type. During the compression tests, a high-speed camera system was used to capture the footage at the instants when damage occurred, and DIC was used to obtain the surface strains. The high-speed camera system captured the instants when fracture initiated at the wavy plies and delamination occurred in the through-thickness direction. Additionally, a post-mortem analysis showed evidence of kink bands by using SEM to characterise the wavy regions. Finite element analysis was performed to investigate the dominant stress component that caused the initiation of failure. It was observed from both the simulation and DIC results that regions with large in-plane shear stresses corresponded with the kink bands, which were formed at the locations of large misalignment angles. One limitation of their research was that only the elastic deformation was simulated, but not the whole process including the progressive failure after the damage initiation. Hence, the progressive failure cannot be verified by the numerical analysis. Moreover, more evidence is required to explain the initiation of damage caused by in-plane fibre waviness. This is because the high-speed camera system only captured the footage of one edge of the specimens to show the initiation of damage. Therefore, the in-plane damage in the specimens was not detected. Since in-plane fibre waviness mainly occurs within a ply, it would have been more useful if high-speed camera systems had been set up to capture footage of failure events on the surface of either the top or bottom ply. The research indicated that the number of wavy plies affected the strength. However, the specimens being tested were all quasi-isotropic specimens. It appears that the effect of waviness defects on other common stacking sequences remains unexamined.

Although kink bands are considered to be the dominant failure mechanism for defective composite laminates with in-fibre waviness, it is not always the case for other mechanical tests. Sitohang et al. [60] investigated the first ply failure associated with in-plane waviness in 2022, when they applied a four-point test and an end-loaded bending tests to

load the laminates to failure. They found that the severity of in-plane fibre waviness influences the failure behaviour. For specimens with smaller waviness angles, kink bands occurred first then followed by matrix failure and delamination. While for specimens with larger waviness angles, only kink band failure was observed. For specimens containing wavy regions having waviness angles larger than 45° and with another wavy region having smaller waviness angles, no kink band was observed. However, the authors suggested that more work on laminates with larger waviness angles were needed to confirm this. The high-speed camera images and micrographs of the fractured specimens showed the failure progression. However, the high-speed camera only captured images from the edge view, therefore, the initiation and propagation mechanism of in-plane damage is still unclear.

2.4.2 Failure criteria for composites

Many failure criteria have been established for composites, however, there is not a universal one that can explain all failure behaviour under different loading scenarios. Each criterion has its own advantages in explaining some phenomenon and each has its limitations. The earliest failure criterion for orthotropic laminae was proposed in 1920 by Jenkins [61], when he suggested using maximum stresses to evaluate failures. To avoid failure, the criterion was expressed as follows:

$$\begin{aligned} -s_L^{(-)} < \sigma_1 < s_L^{(+)} \\ -s_T^{(-)} < \sigma_2 < s_T^{(+)} \\ |\tau_{12}| < s_{LT} \end{aligned} \tag{1}$$

where σ_1 and σ_2 represent the principal stress components in the longitudinal direction and transverse direction; $s_L^{(-)}$ and $s_L^{(+)}$ represent longitudinal compressive strength and longitudinal tensile strength; $s_T^{(-)}$ and $s_T^{(+)}$ represent transverse compressive strength and transverse tensile strength; τ_{12} represents shear stress component and s_{LT} represents shear strength.

Similarly, in 1967, Waddoups [62] proposed the maximum strain criterion for predicting failures in composites. To avoid failure in composites, the criterion was described by the following inequalities:

$$-e_L^{(-)} < \varepsilon_1 < e_L^{(+)}$$

$$-e_T^{(-)} < \varepsilon_2 < e_T^{(+)} \tag{2}$$

$$|\gamma_{12}| < e_{LT}$$

where ε_1 and ε_2 represent the principal strain components in the longitudinal direction and transverse direction; $e_L^{(-)}$ and $e_L^{(+)}$represent longitudinal ultimate strains in the two principal directions; $e_T^{(-)}$and $e_T^{(+)}$ represent transverse ultimate strains in the two principal directions; γ_{12} represents shear strain component and e_{LT} represents ultimate shear strains. One major drawback of the maximum stress and maximum strain criterion is that these two criteria do not consider the interaction between the stress components or between the strain components. Therefore, they are only suitable for cases when unidirectional laminates are subjected to unidirectional loading.

Hill [63] in 1948 developed a new failure criterion based on the maximum stress criterion, while in 1968 Tsai [64] further improved it. The upgraded criterion is known as the Tsai-Hill criterion. When only plane stress was considered, the Tsai-Hill criterion can be expressed as follows:

$$\frac{\sigma_1^2}{s_L^2} - \frac{\sigma_1\sigma_2}{s_L^2} + \frac{\sigma_2^2}{s_T^2} + \frac{\tau_{12}^2}{s_{LT}^2} < 1 \tag{3}$$

The main improvement of the Tsai-Hill criterion is that it takes the interactions between stress components into consideration. This enabled the Tsai-Hill criterion to predict failure in orthotropic and transversely isotropic laminates [65].

All the failure criteria discussed so far do not consider the shear coupling effect, which can cause shear strains in an anisotropic material and lead to failure. To overcome this problem, in 1971, Tsai and Wu [66] developed a new failure criterion to predict failure in anisotropic laminates. When only plane stress was considered, the Tsai-Wu criterion can be expressed as follows:

$$F_{11}\sigma_1^2 + F_{22}\sigma_2^2 + F_{66}\sigma_6^2 + F_1\sigma_1 + F_2\sigma_2 + F_{12}\sigma_1\sigma_2 < 1 \tag{4}$$

where σ_6 represents shear stress component. The value of F_{ij} and F_i can be obtained using the following equations:

$$F_{11} = \frac{1}{s_L^{(+)} s_L^{(-)}} \text{ and } F_1 = \frac{1}{s_L^{(+)}} - \frac{1}{s_L^{(-)}}$$

$$F_{22} = \frac{1}{s_T^{(+)} s_T^{(-)}} \text{ and } F_2 = \frac{1}{s_T^{(+)}} - \frac{1}{s_T^{(-)}} \tag{5}$$

$$F_{66} = \frac{1}{s_{LT}^2}$$

F_{12} can be obtained using a biaxial test according to Tsai and Wu. However, Tsai and Hahn [67] suggested using a simplified equation instead to obtain F_{12}:

$$F_{12} = -\frac{(F_{11}F_{22})^{\frac{1}{2}}}{2} \tag{6}$$

In 1973, Hashin and Rotem [68] developed a criterion (hereinafter called Hashin-Rotem criterion) predicting fibre failure and matrix failure separately. The criterion is expressed in the following equations.

Fibre failure under tension ($\sigma_{11} > 0$):

$$F_{ft} = \left(\frac{\sigma_{11}}{X_T}\right)^2 + \frac{\tau_{12}^2 + \tau_{13}^2}{S_L^2} = 1 \tag{7}$$

Fibre failure under compression ($\sigma_{11} < 0$):

$$F_{fc} = \left(\frac{\sigma_{11}}{X_C}\right)^2 = 1 \tag{8}$$

Matrix failure under tension ($\sigma_{22} > 0$):

$$F_{mt} = \left(\frac{\sigma_{22} + \sigma_{33}}{Y_T}\right)^2 + \frac{{\tau_{23}}^2 - \sigma_{22}\sigma_{33}}{S_T^2} + \frac{{\tau_{12}}^2 + {\tau_{13}}^2}{S_L^2} = 1 \tag{9}$$

Matrix failure under compression ($\sigma_{22} < 0$):

$$F_{mc} = \left[\left(\frac{Y_C}{2S_T}\right)^2 - 1\right]\frac{\sigma_{22}+\sigma_{33}}{Y_C} + (\frac{\sigma_{22}+\sigma_{33}}{2S_T})^2 + \frac{{\tau_{23}}^2 - \sigma_{22}\sigma_{33}}{S_T^2} + \frac{{\tau_{12}}^2 + {\tau_{13}}^2}{S_L^2} = 1 \quad (10)$$

In the above equations, X_T and X_C represent tensile and compressive strengths in the fibre direction; Y_T and Y_C represent tensile and compressive strengths in the perpendicular direction; S_L and S_T represent the longitudinal and transverse shear strengths; σ_{11}, σ_{22}, σ_{33}, τ_{12}, τ_{13}, τ_{23} represent the six stress components in three-dimensional stress state. Either fibre damage or matrix damage starts due to tension or compression when one of the corresponding failure indicators F_{ft}, F_{fc}, F_{mt}, F_{mc} is greater than 1. The benefit of using Hashin-Rotem criterion [68] is that fibre and matrix failure are considered separately, which is closer to experimental results.

Recently, a comparison of failure criteria for composites was performed in the "World Wide Failure Exercise II Competition", where twelve leading criteria were tested for their prediction of the response of composites made of different materials, with various lay-ups, and under diverse three-dimensional stress states. The results were summarised in [69]. In the competition, no criterion was found to outperform the others for all the test cases. Therefore, there still exists a need to develop a unified failure criterion that can predict all damage behaviour in composites.

2.5. Shape descriptors and image decomposition

A great number of images can be generated when using optical techniques, e.g., digital image correlation (DIC) and electronic speckle pattern interferometry (ESPI), to take full-field measurements. However, using such a great amount of image data for comparisons or validation of model predictions can be time-consuming and sometimes unnecessary. Therefore, image data reduction is indispensable to simplify the comparison of full-field data. Industrial digital camera sensors capture light intensity over an array of pixels. The pixel location can be denoted by their spatial coordinates x and y, and the pixel intensity at each location can be represented by a range of grey levels. Normally for an 8-bit camera, the grey level ranges from 0 to 255. This means that an image can be presented by a two-dimensional function $f(x, y)$. However, this function is not the only way to convey information in an image. Alternatively, images can be presented differently without losing important

information. Shape descriptors are one of the tools that can be used to process images and generate numerical values that still carrying the same information. Shape descriptors can be used for applications such as: pattern recognition [70], feature extraction [71], or edge detection [72] etc. While in the engineering field, shape descriptors are more widely used for the validation of model predictions using measurements [73].

Shape descriptors can be classified into two groups: contour-based and region-based [74]. This classification is based on whether the shapes are extracted from the contours or from the whole regions, in other words, whether the interior content of the extracted shape is represented or not. Of all the contour-based shape descriptors invented, Fourier descriptors might be the most widely used for applications such as recognition of three-dimensional objects [75] and two-dimensional image classifications [76]. Fourier descriptors are rotation, scaling, and translation invariant when describing images [77]. However, conventional Fourier descriptors can only be used to represent a closed curve. Thus for representing broken shapes, auxiliary methods need to be developed [78]. Another problem is that conventional Fourier descriptors, like all the other contour-based shape descriptors, can only be used to represent the one-dimensional boundary of a shape. This makes it unsuitable for analysing cases when the interior content within a shape is not negligible, for example, when analysing full-field strain maps.

Region-based shape descriptors, instead of only processing the boundary information, take all the pixels within a shape into account. Orthogonal moments, such as Zernike moments and Chebyshev polynomials are region-based shape descriptors. They are invariant to translation, scaling and rotation, which enable them to be widely used to process structural responses, such as strain maps when subjected to static loadings or mode shapes obtained from modal analysis to reduce data dimensionality. One attempt of using Zernike moments to decompose strain maps was made by Patki and Patterson [79] in 2010. They found that although Zernike moments can be used to decompose and reconstruct strain maps with ease and data reduction can be achieved, they cannot be used to deal with strain maps with discontinuities, for example, a hole at the centre of a specimen causing sharp discontinuities in the strain maps. This is because the Zernike moment descriptors are only orthogonal over a unit circle. The problem was overcome by using a two-dimensional discrete Fourier transform on the strain maps with discontinuities first, then performing the decomposition

using Zernike moments on the magnitude of the frequency domain generated from the Fourier transformation. This new method was named by the authors as Fourier-Zernike descriptors. The Fourier-Zernike descriptors were then used to decompose three strain maps obtained using DIC for three composite specimens subjected to tensile loads. One specimen had an impacted hole, one specimen had a machined hole and the other one was a virgin specimen. By comparing the Fourier-Zernike descriptors for the three strain maps, it was observed that although the two holes have approximately the same size, there existed a difference in the descriptors plot. Their findings indicated that Fourier-Zernike descriptor can be used to decompose discontinuous strain maps with a high accuracy and provide a way to assess damage in structures. They also proposed that this descriptor could be used for validation of finite element models with experimental data. In 2015, Lampeas et al. [80] developed an alternative approach of using Zernike moments to decompose displacement or strain images for validation of models. They proposed to select the most important Zernike moments according to their magnitudes, which can reduce the number of moments for representing the images from 400 to less than 50, although this caused a slight increase of reconstruction error. Their results were proved to be robust and effective for validations of models and overcame the complexity of pointwise comparisons between models and experimental data. They also developed two approaches to decompose displacement or strain maps with discontinuity when using Zernike moments, for example, a hole in the middle of the maps. The first approach was to partition the maps with a hole into several regions but excluding the hole, then perform the decomposition and comparison separately. Although this approach might exclude some critical regions, the situation could be improved by adding additional “patches” to cover more regions with a relatively higher computational cost. The second approach was to interpolate the hole with neighbouring values around it, and then perform the decomposition and comparisons. However, this approach might bring too much extrinsic information to the original image if the discontinuous areas are too big or the gradients between the boundaries are severe. The solutions to this could be examining the interpolation outcome with care and making sure the reconstruction error is not affected. The two approaches were shown to be consistent in validating the models with experimental results.

In 2012, Sebastian et al. [81] proposed an approach for validating model predictions with experimental data. Their approach was based on image decomposition of strain maps using Chebyshev polynomials. The measured strain map was obtained using DIC for a composite bar under tensile loading, while the predicted strain map was obtained by simulating the tensile test using finite element analysis. The decomposition of the strain map resulted in a series of numerical values representing the coefficients of the Chebyshev polynomials. A scatter plot was made by plotting the resulting coefficients for the predicted strain map against those for the measured strain map. To investigate the validity of the model predictions, a confidence interval was drawn on the scatter plot. The width of the interval was based on the experimental uncertainty and the average squared residual between the reconstructed and original strain map. Therefore, they established an integral way of investigating the reliability of the model predictions. Good predictions were defined as when all the scattered data points representing the coefficients of Chebyshev polynomials were located within the confidence interval. While perfect predictions were achieved if all the scattered points lie on a straight line of a gradient of unity, however, in practise this will never happen. It can be observed that their method is capable of eliminating the influence of data redundancy when validating model predictions with experiment derived strain maps. More importantly, the method can provide robust evidence on the reliability of model predictions. In 2014, a wide range of organizations, institutions, and universities [82] drafted and approved an agreement on validating computational solid mechanics models. In this agreement, they further improved the method in [81] by providing detailed instructions on image decomposition and correlation of data from model and experiment. In addition to this, they also provided calibration procedures for optical systems using specialised reference materials, allowing the measurement uncertainty to be calculated. The approaches they proposed in the agreement can be helpful for decision makers in quantifying the confidence of the model predictions.

2.6. Knowledge Gaps

There is a growing body of literature recognising that fibre waviness affects the mechanical properties of composite materials. Nevertheless, limited studies have investigated the residual strains caused by fibre waviness. Evidence has shown that fibre waviness can cause residual strains, which is strongly correlated with the final failure of

composites [7]. Therefore, failure in composites could be predicted using models incorporating residual strains. However, no such models have been developed for predicting residuals strains in defective composite laminates with fibre waviness based on non-destructive characterisation of the defects. Algorithms such as Fourier transformation and Radon transformation have been implemented to characterise fibre orientations from morphological data obtained using various measurement techniques, while the performance comparisons of the algorithms have been made qualitatively. This implies a need for better utilising of the characterisation data of waviness defects for developing models to predict residual strains. This is identified as the first knowledge gap. This knowledge gap can be filled by completing the second objective, which will be discussed in Chapter 5.

A number of studies have suggested using sinusoidal functions to represent the geometric shape of fibre waviness. The severity of the waviness defect thus can be quantified using the wavelengths and amplitudes of the sinusoidal functions, which has been correlated with the effect on the performance. However, the morphology of actual fibre waviness in industry is often more complex than deliberately induced waviness defect with regular shapes produced in laboratories. Actual fibre waviness often contains random orientations that cannot be represented by simple sinusoidal functions. Therefore, a more general method for characterising and assessing the severities of fibre waviness is needed. This is identified as the second knowledge gap.

Resonant behaviour of defective composite laminates has been investigated both experimentally and numerically. Most research focused on the influence of defects on the resonant frequencies, seldom has research analysed the effect on the mode shapes. Fibre waviness affects the stiffness and density distribution of composite laminates; thus it must affect the mode shapes. However, there has been little quantitative analysis of how fibre waviness affects mode shapes. It is also unclear if abnormal resonant behaviour of defective composites can be used to identify the presence of defects. This is identified as the third knowledge gap. This knowledge gap together with the second one can be filled by completing the first objective, which will be discussed in Chapter 4.

The onset and propagation of damage in defective composites with fibre waviness has not been experimentally investigated in any prior research, in particular the progression of

failure is still unclear in a fracture process. Current research focuses more on out-of-plane deformation, while the in-plane damage has not been explored in real time. Besides lacking experimental investigation, there has been little modelling work based on characterisation of actual fibre waviness and incorporating these defects into finite element models for predicting the failure behaviour. Failure criterions have been developed for predicting failure of composites under various loading conditions. However, whether the existing failure criterions are applicable for predicting all failure behaviour of laminates with fibre waviness has not been investigated. This is identified as the fourth knowledge gap. This knowledge gap can be filled by completing the third objective, which will be discussed in Chapter 6.

3. Experimental techniques

This chapter summarises the experimental techniques that will be used in this thesis. The orientation information of fibre waviness is crucial in determining the strength and governing the failure behaviour. Pulse-echo ultrasonic inspection was thus used to obtain the fibre orientation of the defective surface of the laminates. DIC was used in this study for two purposes. One is to measure the surface shape of specimens in order to calculate the residual strains. The other one is to capture failure scenes and to obtain full-field strains in both the top and bottom surface of specimens being loaded to first ply failure when under a four-point bending test. AF-ESPI was used to obtain mode shapes of CFRP laminates under vibration loads at different resonant frequencies to investigate the vibration behaviour of defective composites with fibre waviness.

3.1. Pulse-echo ultrasonic inspection

Pulse-echo ultrasonic inspection was used in this study to characterise the waviness defect in the CFRP specimens. A water immersion ultrasonic method was used, as shown in Figure 5, where water was used as a couplant. The reason for using a couplant is because the acoustic impedance mismatch between air and solid objects being tested is very high, resulting a great loss of ultrasonic energy so that most of the energy is reflected and only a small amount transmitted. Water was thus used to provide low attenuation and consistent coupling between the transducer and the specimens. A pulse-echo ultrasound A-scan is the most basic way for detecting defects in components. When using an A-scan, the transducer emits ultrasonic pulses that reach the interface between the couplant and the top surface of a specimen, causing the pulse to be partially reflected and the rest is transmitted through the specimen. The first reflected pulse is named as the front wall echo. The transmitted pulse also reflects later after hitting the back wall, and this is known as back wall echo. The layered structure of a CFRP laminate produces small echoes between the front and back wall echoes due to the interface of plies, and these small echoes become gradually weaker with depth. A-scan can be used to show the existence and depth of defects, for example, cracks or voids, by identifying the appearance of new echoes between the front wall echo and the back wall echo. However, an A-scan cannot provide the morphology of defects. A C-scan, on the other hand, can provide the morphology of a scanned cross-section. A C-scan presents ultrasound signals time gated at a constant depth and display the signals' amplitudes as an image. In-

plane fibre waviness is only significant at the surface of a laminate; therefore, the time gate is to set to collect the ultrasound signals at the interface between the top defective ply and the subsequent ply lying beneath. The amplitude of the ultrasound signals can be presented as a grey-scale image revealing the fibre orientations in the cross-section. The setting details of the ultrasonic pulse-echo C-scan system are introduced in Section 5.2.3.

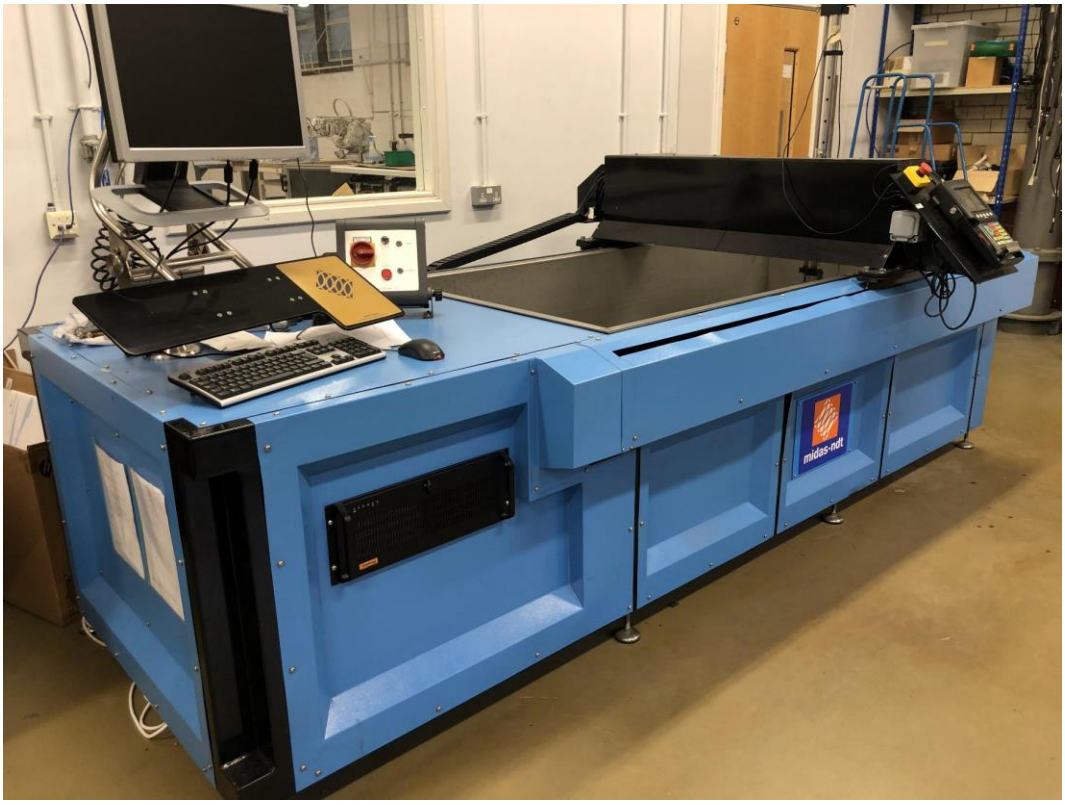

Figure 5: Automated ultrasonic inspection system used by the author.

3.2. Digital Image Correlation

Stereoscopic DIC was used to measure the surface profiles and deformation of specimens subjected to bending loads in this study. An example DIC system for measuring displacement in three dimensions is shown in Figure 6. Using two cameras three-dimensional information about the surfaces being measured can be obtained. The measured surface needs to have a random pattern on it, this is typically achieved by applying a speckle pattern on the surface using spray-paint. The random pattern thus can be divided into a number of overlapping facets that cover the whole surface. Each facet needs to have unique speckle information that can be converted into a unique grey-scale image by the CCD cameras. The matching of the facets between images is achieved by minimising the error function of the same facet between the start of the test and any loading stages. One classic error function is

the sum of squared differences of the pixel values, and smaller function values means better matching has been achieved. Therefore, each facet's movement can be tracked. Three dimensional stereoscopic DIC system with two cameras were used as the morphology of the surface and out-of-plane displacements during loading were of interest. Each facet's movement is captured by the two cameras at different loading stages, from which the three-dimensional displacements of each facet at these loading stages can be obtained. Therefore, a displacement vector field for the whole surface can be obtained by analysing the results from all the facets. Strain maps for the whole surface can also be obtained by calculating the derivatives of the displacement fields. Setting details of DIC are introduced in Sections 5.2.2 and 6.2.3.

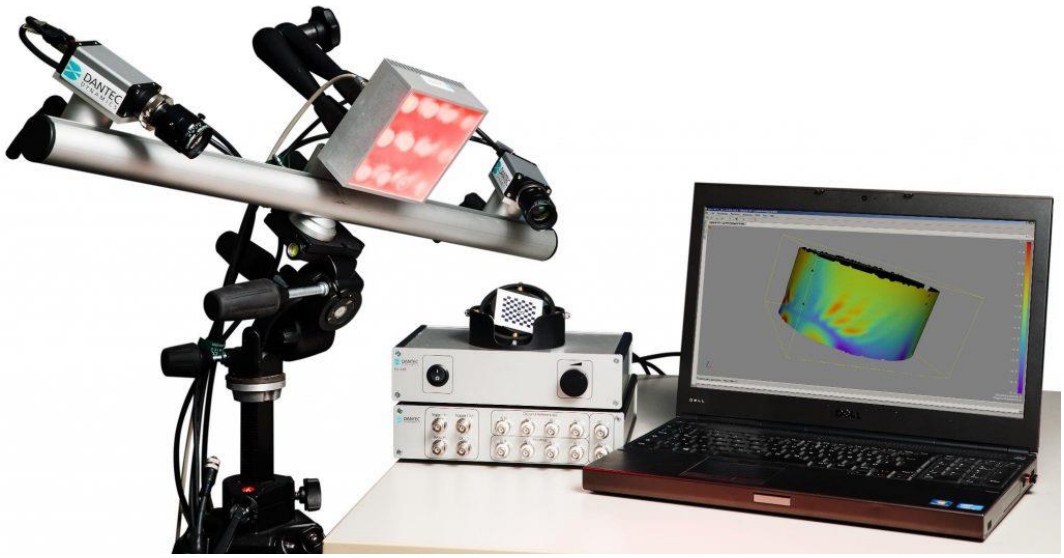

Figure 6: Three-dimensional displacement measured by a stereo DIC system with two cameras [83].

3.3. Amplitude fluctuation electronic speckle pattern interferometry

AF-ESPI was used to obtain the mode shapes for specimens under vibration loads at resonant frequencies. The set-up of the AF-ESPI system is shown in Figure 7. AF-ESPI is a non-contact technique for measuring surface displacements of objects under various loading conditions. In this thesis, the real-time measurements of out-of-plane displacement are used to generate fringe patterns that represent mode shapes. To perform the AF-ESPI analysis, some requirements need to be satisfied. The first requirement is that the optical paths of the

reference and object beams must be the same. This was satisfied by adjusting the mirror set locations shown in Figure 7. The second requirement is that the light intensity of the reference and object beam detected by the CCD camera must be the same. This was satisfied by putting a polariser in the optical path of the reference beam. The light intensity of the reference beam thus can be tuned to match that of the object beam by adjusting the rotation angles of the polariser. The third requirement is that a good contrast fringe pattern must be generated for every test. This was achieved by spraying a white powder coating on the surface of the specimens being measured, and by placing a ground glass in the optical path of the reference beam. Thus, uniform light from both object beam and reference beam can be assured. The detailed procedures of using the AF-ESPI are described in Section 4.2.3.

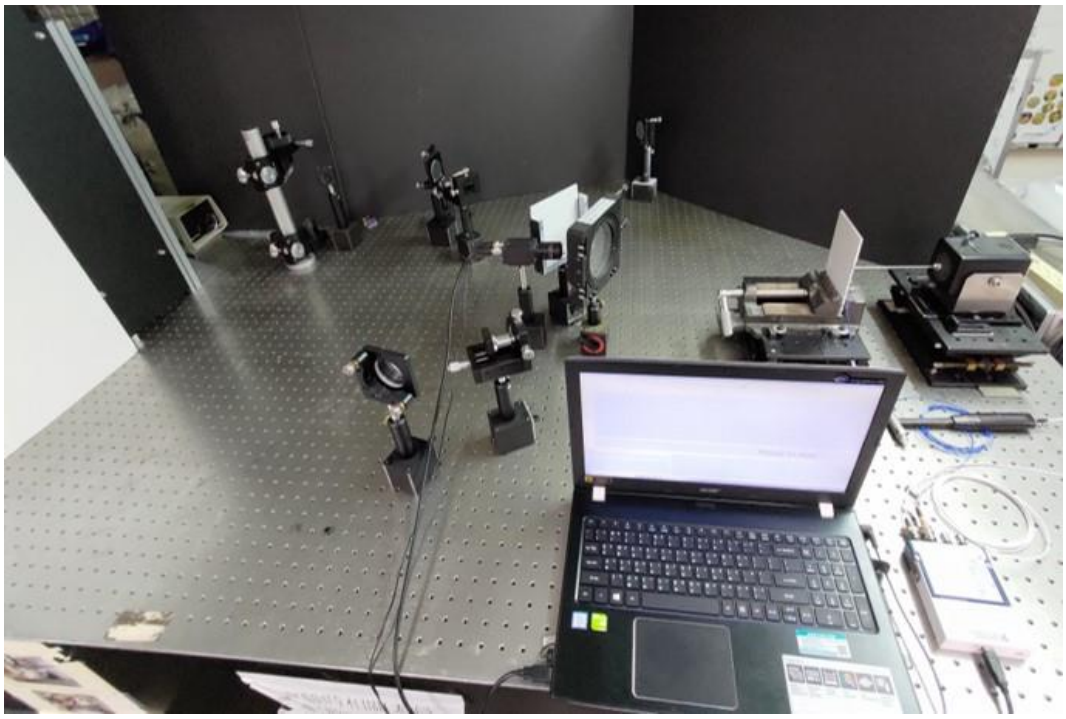

Figure 7: AF-ESPI set-up for obtaining mode shapes for a specimen under vibration loads at the resonant frequencies used by the author. Annotations of the components are introduced in Figure 10.

4. Identification of defects in composite laminates by comparison of mode shapes from electronic speckle pattern interferometry

4.1. Introduction

The most recent work conducted to investigate the effect of fibre waviness on vibration behaviour was in 1994 [20], where using analytical and numerical methods, it was found that fibre waviness caused a reduction in resonant frequencies for certain modes. This effect was predicted to be more significant if the waviness defect occurred in the plies that contributed more stiffness to the laminate. They also found that bending modes are more susceptible to waviness defects that occurred in the 0° ply. However, whether the mode shapes of CFRP components would be affected by fibre waviness has not been explored by any subsequent research, and this has been identified as one of the knowledge gaps.

As reported in the literature survey, amplitude fluctuation electronic speckle pattern interferometry (AF-ESPI) has been used to identify pre-cut square and circular defects in composite plates based on changes in mode shapes, with the effects of the defects being more visible in the fringe patterns for higher modes [8]. Interfacial cracks can also be detected using AF-ESPI by comparing the fringe patterns of specimens with and without defects [55]. Whilst these studies could identify defects by comparing fringe patterns for defective and non-defective specimens, these comparisons were made qualitatively. In order to make quantified comparisons, this chapter introduces a novel image processing technique that combines the density-based spatial clustering of applications with noise (DBSCAN) algorithm and contour decomposition using Fourier descriptors. This was used to quantify the difference between the nodal regions of mode shapes and thus identify the presence of fibre-waviness defects.

This chapter is based on the following paper, written by the author of this thesis:

Xiaonan Li, Po-Chi Sung, E.A. Patterson, Wei-Chung Wang, W.J.R. Christian. “Identification of defects in composite laminates by comparison of mode shapes from electronic speckle pattern interferometry”. *Optics and Lasers in Engineering*. 163:107444, 2023. The entire original draft of the paper was written by Xiaonan Li. The contribution of Xiaonan Li to this paper also include conceptualization, methodology, investigation, software. Xiaonan Li has

obtained the agreement from the other authors to include the contents from the published work in this thesis.

4.2. Experimental Methods

4.2.1. Specimen preparation

Carbon fibre reinforced cross-ply laminates, with a stacking sequence of $[0_2/90_2/0_2/90_2]_s$, were manufactured using unidirectional prepreg (RP542-4UT300, PRF, UK). Three defect-free specimens were first manufactured to serve as a benchmark set. Three defective composite specimens were then manufactured using the method described in [7] to induce a band of in-plane fibre waviness across the width of the laminates. The waviness defects were formed using a special aluminium former, as shown in Figure 8 left. Each ply was laid on top of the former in the predetermined stacking sequence to create a laminate. The V-shaped laminate was then removed from the former and flattened by hands. The fibres in the top ply, at the tip of the V-shape, buckled to compensate for the length difference between the top ply and the plies beneath it after the laminate had been flattened. This created a localised band of in-plane waviness at the middle of each specimen on the top ply, as shown in Figure 8 middle.

The laminates were cured in a hot press (APV-2525, Meyer, Germany), by heating them up to 120 ℃ from room temperature (23 ℃), at a heating rate of 1 ℃/min. After heating, they were held at 120 ℃ for 1 hour. The hot press pressure was set to 2.5 bar during heating, curing and cooling. Once the laminates were cured, the hot press was left to naturally cool to room temperature. After being removed from the hot press, each specimen was cut using a wet diamond saw (Versatile 103450, Vitrex, USA) to a size of 150 mm by 100 mm. The average thickness of the specimens was 3.72 mm. A typical defective specimen is shown in Figure 8, with one side having in-plane fibre waviness in the top ply and the plies beneath it containing no waviness. The top surface of each specimen was then sprayed with a layer of white powder (D-70, Mel-L-Chek, USA) to prevent specular reflections during the AF-ESPI testing.

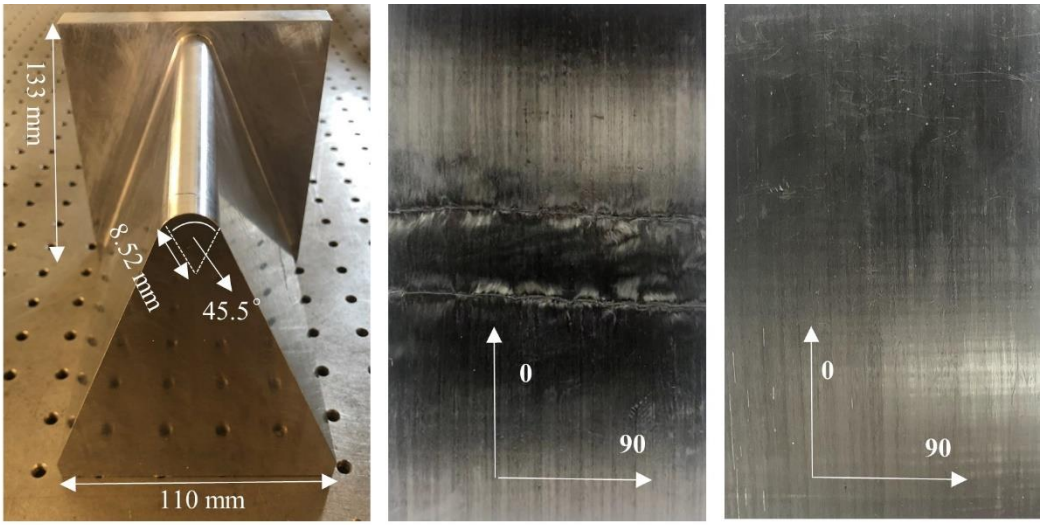

Figure 8: An aluminium former for creating localised fibre waviness (left), the top surface of a defective specimen with in-plane waviness in the top ply (middle), and the bottom side (right). The 0° fibres were aligned along the length of the laminate.

4.2.2. Modal analysis by impact excitation

Modal analysis by impact excitation was performed on each specimen to find its resonant frequencies. Each specimen was impacted by a hammer (PCB, 086B01, USA) at one point and the response was measured at another point by an accelerometer (PCB, 352C22, USA). The impact and measurement points were determined after a few pre-tests to make sure that clear peaks in the frequency response function (FRF) curve were observed. The selected points are shown in Figure 9. Each specimen being tested was clamped by a vice and attached to a stinger. The vice was attached to an optical table and the stinger was connected to a shaker (Labworks, ET-132, USA). The impact-based modal analysis was conducted on the specimens whilst the shaker remained inactive. In the case of defective specimens, the accelerometer and stinger were affixed to the non-wavy side, which coincided with the side impacted by the hammer. The accelerometer output was recorded by a data acquisition system (National Instruments, NI 9234, USA), connected via a USB adaptor (National Instruments, NI USB-9162, USA). Subsequently, the acquired data was processed by a commercial software (M+P International, Germany) on a laptop. This process facilitated the calculation of frequency response functions and the determination of the first five resonant frequencies for each specimen The schematic drawing of the modal analysis by impact excitation is shown in Figure 10.

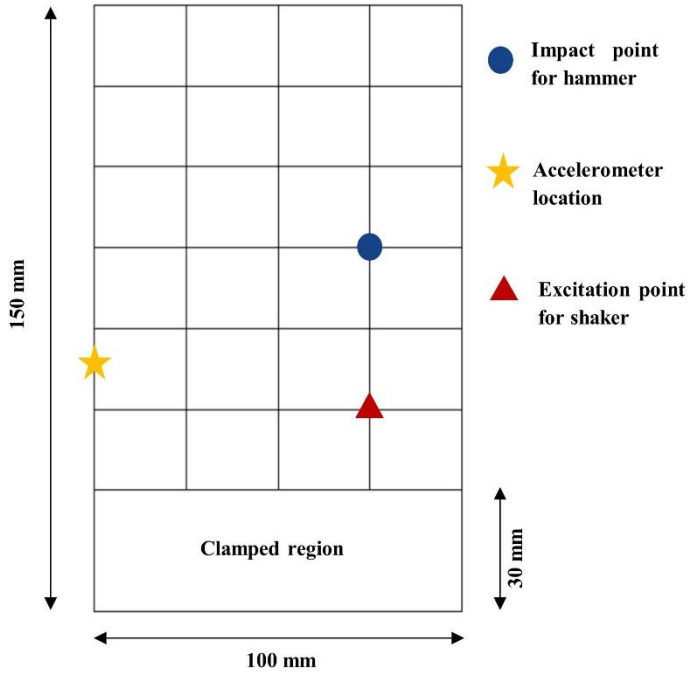

Figure 9: Diagram showing the excitation positions for the impact and shaker, accelerometer location and clamped region of each specimen.

4.2.3. Modal analysis by shaker excitation combined with AF-ESPI technique

The specimens underwent excitation using a shaker connected to the excitation point through a stinger. Sine waves provided by a function generator (Agilent, 33220A, USA) were set sequentially to the five resonant frequencies obtained by the impact-based modal analysis for each specimen, and the analogue signals were amplified using a power amplifier (Labworks, PA-138, USA) before being transmitted to the shaker. For each resonant frequency, AF-ESPI was performed on the specimens while they were loaded by the shaker. The AF-ESPI set-up is depicted in Figure 10. A He-Ne laser (Spectra-Physics, model 12735, USA) provided coherent light, which was split into two beams - one acting as the reference beam and the other as the object beam. The object beam was directed towards the specimen, where it was reflected. The reflected object beam together with the reference beam went back to a camera (Intelliwave, RS170, USA) generating interference speckle patterns, which contained information on the interferometric measurement of surface displacements during vibrations at the resonant frequencies.

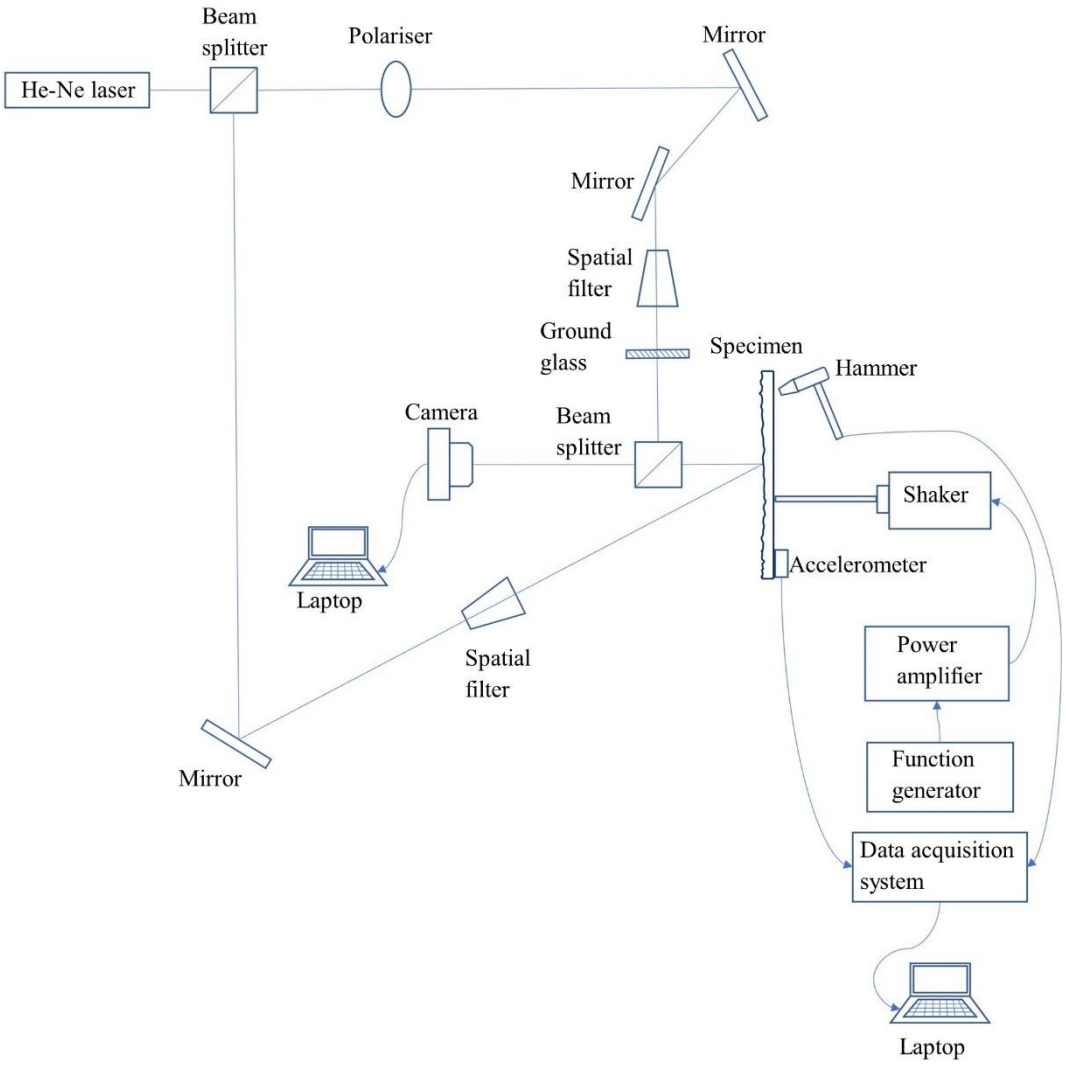

Figure 10: Schematic of the AF-ESPI and modal analysis set-ups.

Unlike traditional ESPI using video-signal-addition or video-signal-subtraction methods, the reference image was not taken when the shaker was turned off and the specimen was stationary. Instead, for the AF-ESPI technique, a reference image was taken at each resonant frequency of the specimen at one instant during the vibrations, and another image was taken afterwards at the same frequency and subtracted from the reference image. The difference between these two image signals was converted into a greyscale image using the image processing system (Intelliwave, v6.7.1, USA), resulting in an interference fringe pattern.

4.3. Results

An example of the FRF for one of the specimens is shown in Figure 11. The FRF was obtained by analysing the acquired data from modal analysis by impact excitation. The FRF

was divided into a real part and an imaginary part. The first five resonant frequencies were identified as the peaks of the curve in the imaginary part, which also corresponded to abrupt changes to the curve in the real part. The first five resonant frequencies for all the specimens are shown in Table 1.

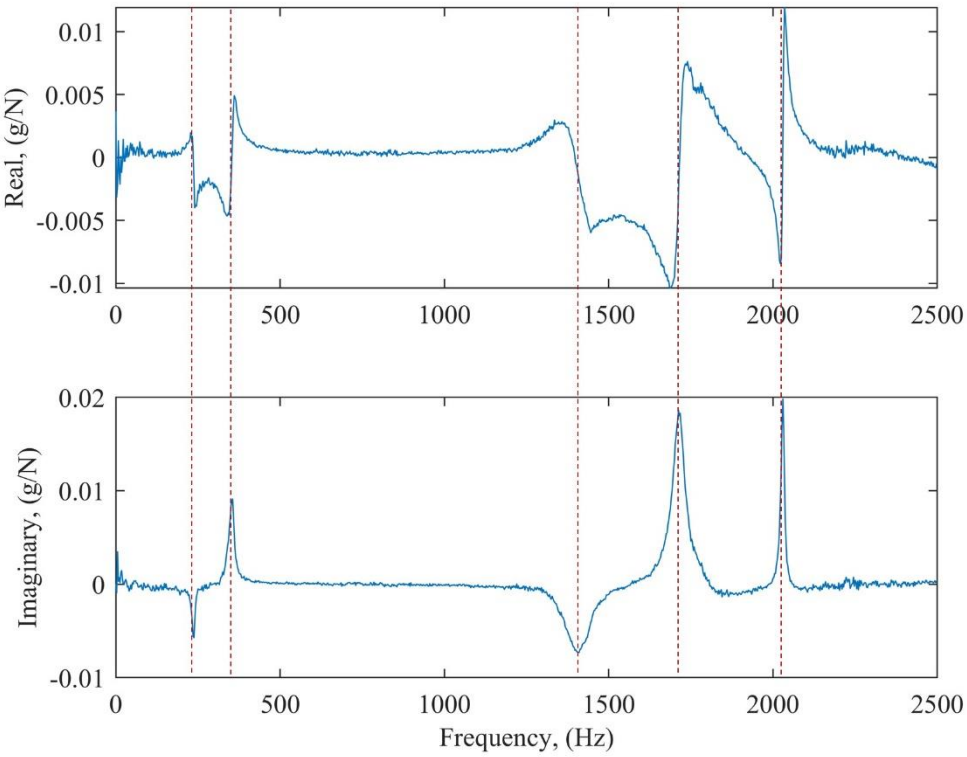

Figure 11: Frequency response function of a defect-free specimen with top plot showing the real part and bottom showing the imaginary part. The first 5 resonant frequencies are indicated by dashed lines.

Fringe patterns were obtained from the modal analysis combined with the AF-ESPI technique when each specimen was excited using the shaker, as shown in Figure 12, representing the five vibration modes for all the specimens. The fringe patterns for the defect-free specimens are shown in the left three columns, while the fringe patterns for the defective specimens are shown in the right three columns. Each one of the five rows of the patterns shows the mode shapes from the 1st mode to the 5th mode respectively. It can be observed that both the 1st and the 3rd mode are pure bending modes, both the 2nd and the 5th mode are pure twisting modes, and the 4th mode is a mixed mode of bending and twisting. For the sake of reproducibility of the tests and repeatability of the results, the experimental set-ups have been dismantled and reassembled six times. Modal analysis combined with the AF-ESPI technique were also performed six times on one defective specimen and one defect-free

specimen to ensure that the resonant frequencies and fringe patterns obtained for the first five modes were consistent.

Table 1: Resonant frequencies of the first five modes obtained from the modal analysis by impact excitation for the three defect-free and three defective specimens.

Specimen Type and No.	1^{st} mode (Hz)	2^{nd} mode (Hz)	3^{rd} mode (Hz)	4^{th} mode (Hz)	5^{th} mode (Hz)
No defect #1	240	350	1405	1718	2028
No defect #2	238	355	1425	1725	2024
No defect #3	238	355	1410	1712	2030
Defective #1	238	348	1490	1715	2115
Defective #2	255	375	1558	1725	2123
Defective #3	255	378	1550	1733	2113
Mean of no defect	239	353	1413	1718	2027
Mean of defective	249	367	1533	1724	2088
Difference between the two means in percent	4.2%	4.0%	8.5%	0.3%	3.0%

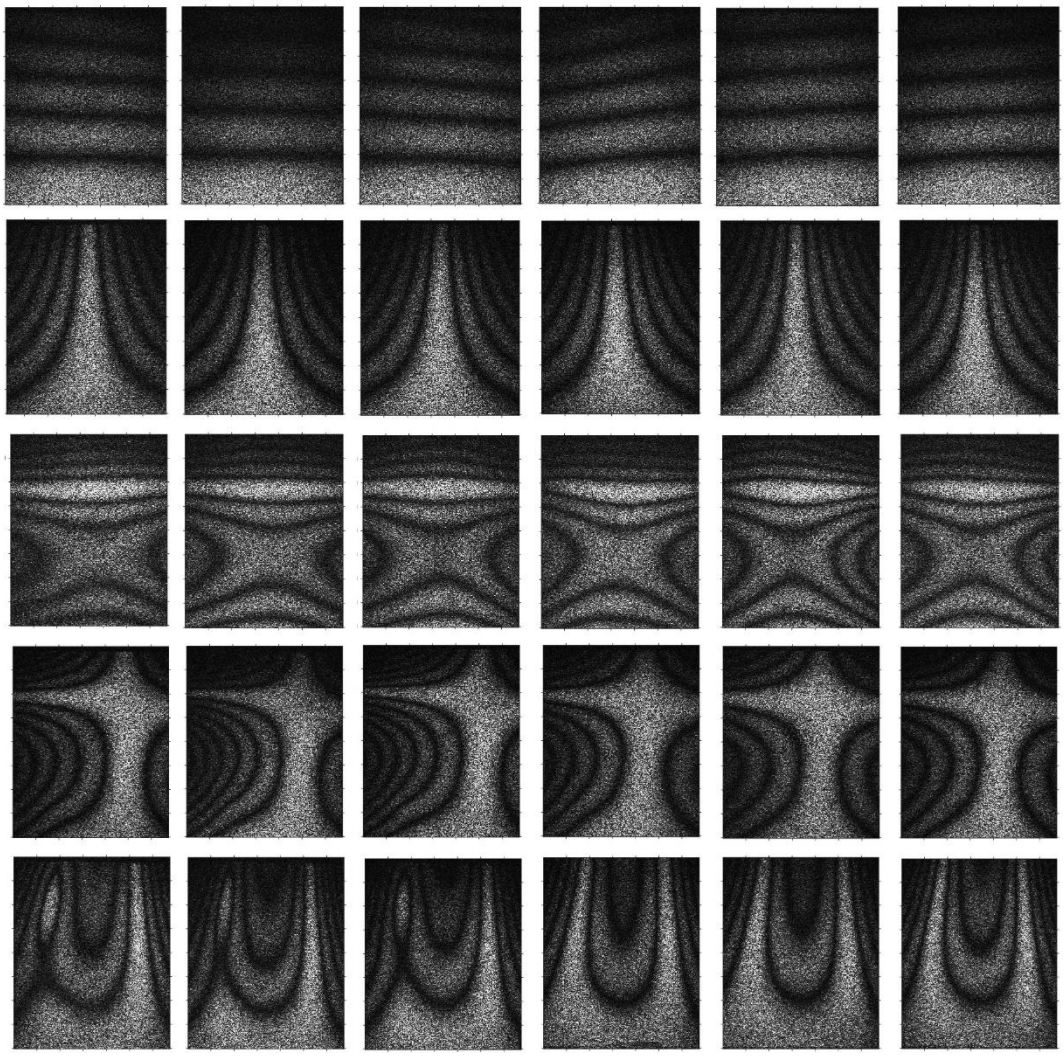

Figure 12: Electronic fringe patterns obtained using AF-ESPI at the resonant frequencies for the six specimens. Each row shows the fringe patterns corresponding to the 1st (top) to the 5th (bottom) mode shape. The left three columns of the fringe patterns show the mode shapes for the defect-free specimens, the right three columns show the mode shapes for the defective specimens.

The extraction process for the contour of the nodal region was performed by a specially developed algorithm, as shown in Figure 13. The original fringe pattern is a greyscale image. The largest bright fringe is not clearly separated from the other fringes, therefore the mean image intensity was subtracted from every individual pixel, which is a common procedure in the field of computer vision and deep learning to reveal features of interest [84]. The mean-subtracted image was then binarized by adaptive thresholding. The threshold was set by calculating the mean pixel intensity within a window of size, *s*, around each pixel. The value of each pixel was set to black if its value was lower than the threshold for its window, otherwise it was set to white. The window size, *s* was set to 1/8 of the image width, as suggested in [85]. The binarized image was then divided into several clusters using the

density-based spatial clustering of applications with noise algorithm (DBSCAN), where each colour represented a cluster, as shown in Figure 13. DBSCAN is a data clustering algorithm to divide points into separate groups based on the density, which means points closely packed are considered as belonging to a group, while points distant from others are outliers. Two important parameters for using the DBSCAN algorithm are the searching radius and the minimum number of points to be considered as a cluster. The principle of DBSCAN is to identify three different types of points: the core points, which are the minimum number of points within the searching radius to form a cluster, thus each cluster has the same density; the border points, which are located at the searching radius of the core points, but do not have the minimum number of points in their own searching radius to form a cluster; and noise points, which are outliers [86]. The core points are the interior points of clusters, and the border points are the boundaries of the clusters. Clusters cannot be combined into a single cluster if they do not share a core point. The minimum number of points to form a cluster was set to the default value of 4, as the data was two-dimensional [87]. For each point in the binarized image, the 4^{th} nearest point to it was found and the Euclidean distance between them was calculated as the 4^{th} nearest distance for this point. The searching radius was determined by calculating the 4^{th} nearest distances for all the points and sorting the points by ascending order of the 4^{th} nearest distances, resulting in the curve shown in Figure 14. The point at which the curve starts to significantly increase, referred to as the knee point of the curve, was identified by finding the location on the curve which formed the largest perpendicular distance to a straight line connecting the start and end point of the curve, as shown in Figure 14. The searching radius was set to the 4^{th} nearest distance corresponding to this knee point. The nodal region can then be easily identified as the cluster with the largest area. The algorithm can automatically select the nodal regions from most of the fringe patterns, except for those of the defect-free specimens for the 5^{th} mode. This is because there is a small bright fringe close to the largest bright fringe with approximately the same level of brightness, which was identified as a detached part of the main nodal region. Therefore, the cluster formed from this small fringe for the 5^{th} mode of the defect-free specimens was manually selected. The contour representing the nodal region was extracted as the borderline of the cluster.

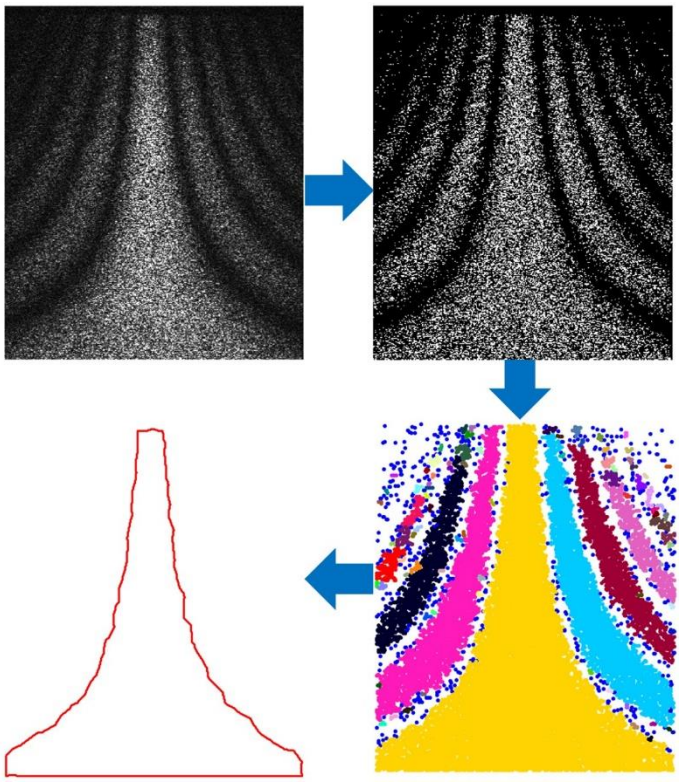

Figure 13: The extraction process of the nodal region from a fringe pattern of the 2nd mode showing: the original fringe pattern in greyscale (top left); binarised fringe pattern (top right); clustered areas after applying the DBSCAN algorithm (bottom right); contour extraction (bottom left).

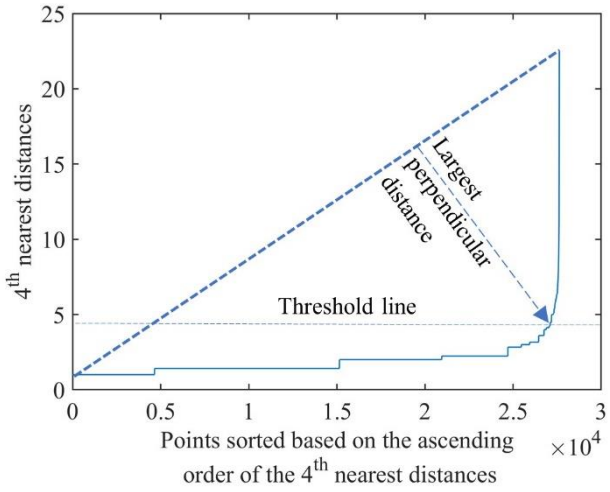

Figure 14: The determination of the threshold value for the searching radius when forming a cluster. All the points of a contour were sorted based on the 4th nearest pairwise Euclidean distance of each point in ascending order and plotted. The threshold was identified by finding the largest perpendicular distance from the line linking the start and end point of the curve to any point on the curve.

The comparison of the fringe patterns representing mode shapes was performed by comparing the extracted contours of the nodal regions. The contours for the 1st and the 3rd

mode shape of all the specimens appear to be largely horizontal lines that lack significant features which can be used for comparison. Therefore, only the 2nd, 4th and 5th modes were selected for comparisons, where the 2nd mode was mainly used as a benchmark mode. Each contour for the three selected mode shapes was decomposed into a number of Fourier descriptors. First, the Fourier spectrum was obtained by applying the discrete Fourier transform to the complex form of the Cartesian coordinates defining the contour. The terms in the Fourier spectrum were listed as follows:

$$FS = [F_0, F_1, F_2, \dots, F_{L-1}] \tag{11}$$

The length of the Fourier spectrum, L, was equal to the number of points in the coordinate system. The sequence of the terms in the Fourier spectrum was then rearranged as:

$$FS_{rearranged} = \left[F_{\frac{L}{2}}, \dots, F_{L-2}, F_{L-1}, F_0, F_1, F_2, \dots, F_{\frac{L}{2}-1}\right] \tag{12}$$

The Fourier descriptors were calculated from $FS_{rearranged}$ using the equation given in [88], with the notation modified for clarity as:

$$FD = \frac{1}{|F_1|} \cdot \left[\left|F_{\frac{N}{2}}\right|, \dots, |F_{N-2}|, |F_{N-1}|, |F_2|, |F_3|, \dots, \left|F_{\frac{N}{2}-1}\right|\right] \tag{13}$$

where F_i is the i^{th} term in the Fourier spectrum, N is an even number, representing the number of Fourier descriptors, and $N \leq L$. It was not possible to reconstruct the contours directly from the Fourier descriptors as they were real valued, which was not an appropriate input for the inverse discrete Fourier transform. Therefore, when reconstructing a contour, the same range in the Fourier spectrum as the Fourier descriptors was used, i.e., the terms from $F_{\frac{N}{2}}$ to $F_{\frac{N}{2}-1}$ in the $FS_{rearranged}$. These terms were converted into the complex form of the Cartesian coordinates using the inverse discrete Fourier transform, and the reconstruction was obtained by plotting the real components against the imaginary components.

The contours are all closed curves except for the three 5th mode nodal regions of the defect-free specimens, which each have two separate contours. Fourier descriptors can only be used to decompose a closed contour [78], so two dummy lines were used to link the two

separate contours. The two dummy lines were created by finding the two nearest points, A and B, on the two separate contours, and then the separate contours were made into a closed one by creating a loop using the two dummy lines A-B and B-A. It should be noted that there are no points between A and B on the dummy lines. An example of the fixed contour for the 5^{th} mode is shown in Figure 15. The quality of the reconstruction from the feature vector varied with the number of terms in the vector. To evaluate the quality of the reconstruction, each image was meshed into 2500 facets, using a facet size equal to 2% of the length of the binary image. The facets which had both the original and reconstructed contours passing through them were considered matched facets, and the facets through which only the original contour passed through were considered mismatched facets. The percentage of the mismatched facets P was then calculated as follows:

$$P = \frac{Number\ of\ mismatched\ facets}{Number\ of\ matched\ facets + Number\ of\ mismatched\ facets} \quad (14)$$

A criterion of $P \leq 10\%$ was used to identify that the reconstruction was acceptable. For the contour shown in Figure 15, the criterion was satisfied when 90 terms were used, as shown in Figure 16. The reconstructions using 10, 90 and 380 terms respectively are shown in Figure 15. Ninety terms were found to be sufficient to achieve an acceptable reconstruction for all of the contours, therefore 90 Fourier descriptors were used for decomposing all of them.

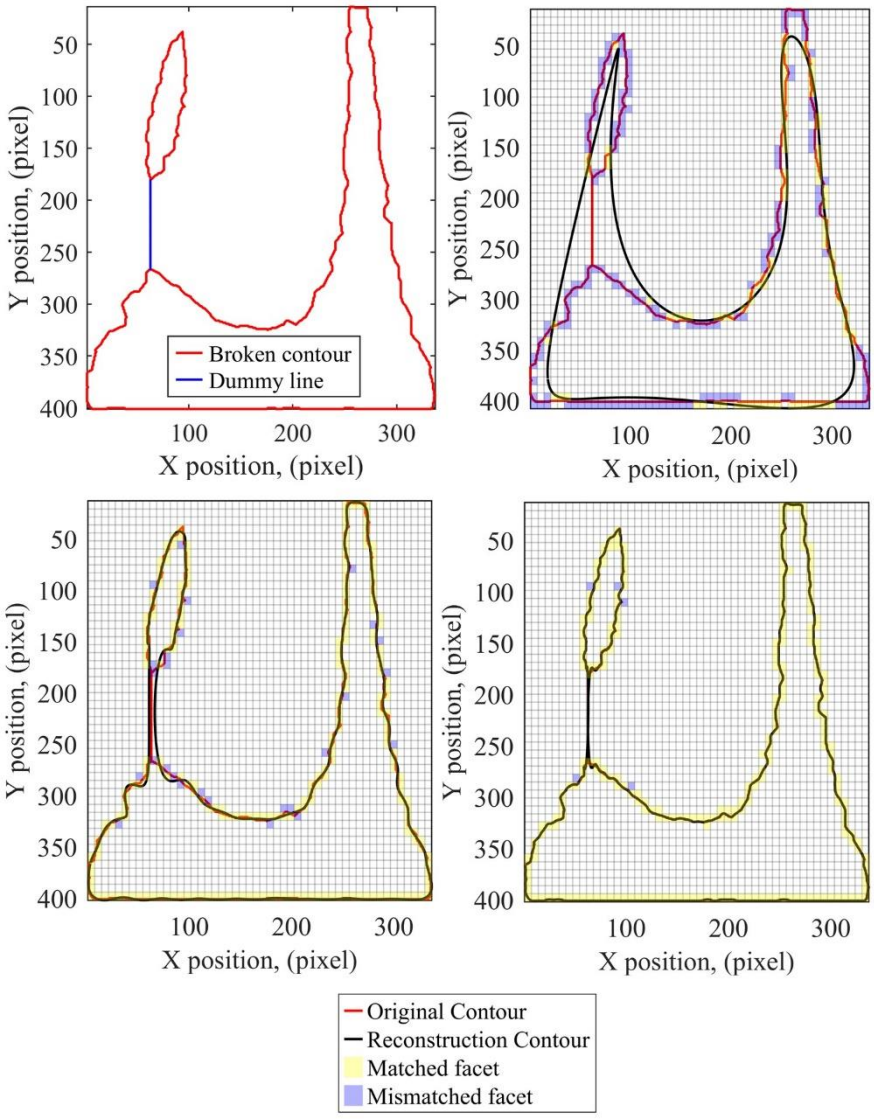

Figure 15: The approach for combining the broken contours of the 5th mode shape of a defect free specimen before decomposing using Fourier descriptors (top left). The original and reconstructed contours using 10 terms (top right), 90 terms (bottom left) and 380 terms (bottom right). The contour map was meshed into 2500 facets, with the matched facets labelled yellow and mismatched facets labelled blue.

The Fourier descriptors as calculated using expression (13) are scale invariant, rotation invariant and translation invariant when being used to represent images [74]. This invariance characteristic was verified by processing two contours representing the 2nd and 4th mode shape of one defect-free specimen in three ways: firstly, by rotating the contour by 30° anticlockwise; secondly, by translating the contour down and to the right by 50 pixels; and thirdly, by rescaling the contour to be 50% of its original size. The original and three new contours of the 4th mode are shown in Figure 17. Each contour was then decomposed into 90 Fourier descriptors to yield feature vectors. The Euclidean distance between pairs of these

feature vectors was calculated and is shown as a correlation matrix in Figure 18. Another popular distance metric, known as the Pearson correlation coefficient, was not selected in this chapter to measure the similarities between the feature vectors, due to the fact that it measures the linear correlation between any two sets of data. This means the Pearson correlation coefficient cannot provide enough contrast to distinguish between feature vectors when used to generate a correlation matrix.

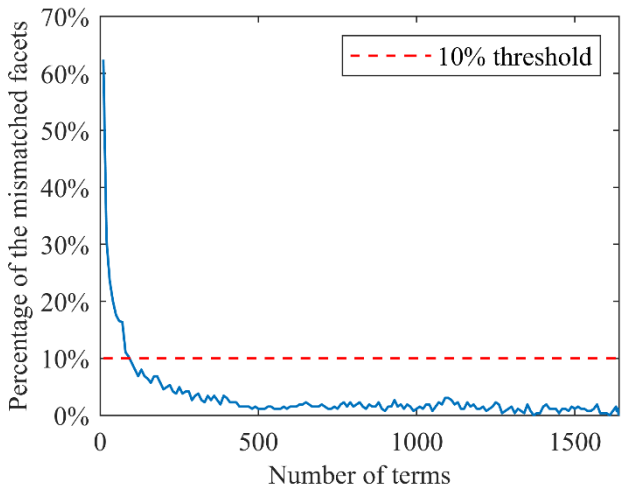

Figure 16: The diagram showing the relationship between the number of Fourier descriptors and the reconstruction quality of the contour shown in Figure 15. The reconstruction quality is represented by the percentage of mismatched facets. The threshold is set to 10% to identify when an acceptable representation is attained.

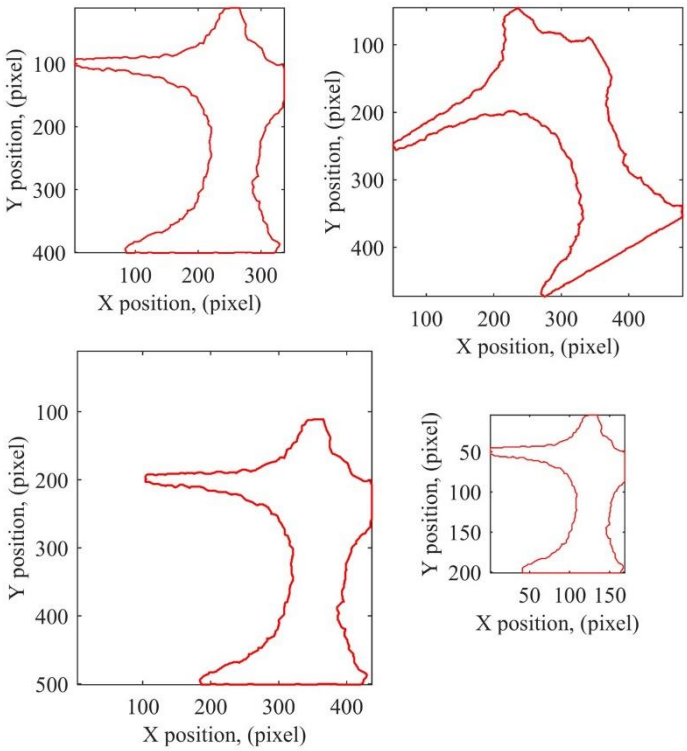

Figure 17: The original contour of the 4th mode for a defect free specimen (top left). The contour transformed by being: rotated 30° anticlockwise (top right), translated towards the bottom right corner vertically and horizontally by 50 pixels (bottom left), and scaled by shrinking by 50% (bottom right).

As shown in Figure 19, three correlation matrices were obtained by comparing the contours of the 2nd, 4th, and 5th vibration mode for the three defective specimens and three defect-free specimens. Each value in the correlation matrices is the Euclidean distance between pairwise feature vectors. The Euclidean distance between any pair of feature vectors representing defect-free specimens was considered as background noise, ed_{noise}; whereas the Euclidean distance between any pair of feature vectors representing defective and defect-free specimens was considered as desired signals, ed_{signal}. Therefore, a ratio r_i, analogous to a signal to noise ratio, was defined as follows:

$$r_i = \frac{E_i\left[ed_{signal}\right]}{E_i\left[ed_{noise}\right]} \tag{15}$$

where i is the number of modes, and the value of i is 2, 4, and 5 respectively; E_i refers to the expected value. The ratios calculated from the correlation matrices in Figure 19 are that r_2 is 1.88, r_4 is 4.67, and r_5 is 6.14.

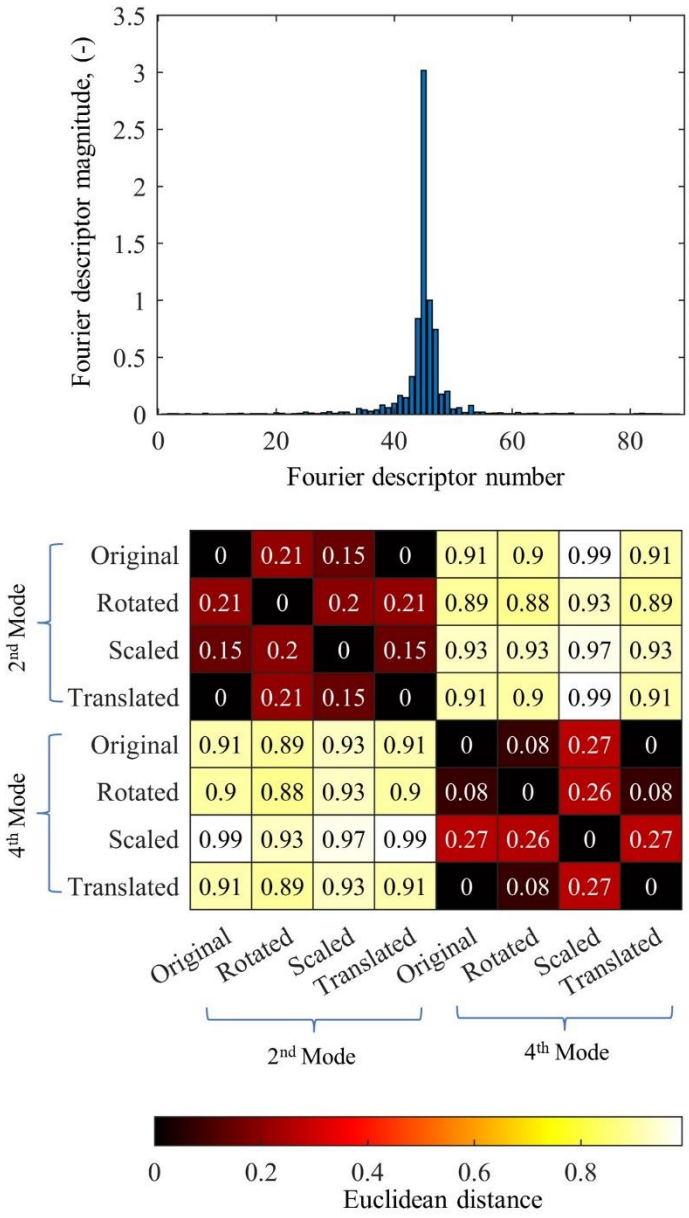

Figure 18: The 90 Fourier descriptors representing the original contour in Figure 17 (top). The correlation matrix showing the Euclidean distances between the feature vectors for the four contours at the 4th mode in Figure 17 and four contours processed using the same ways for the 2nd mode (bottom).

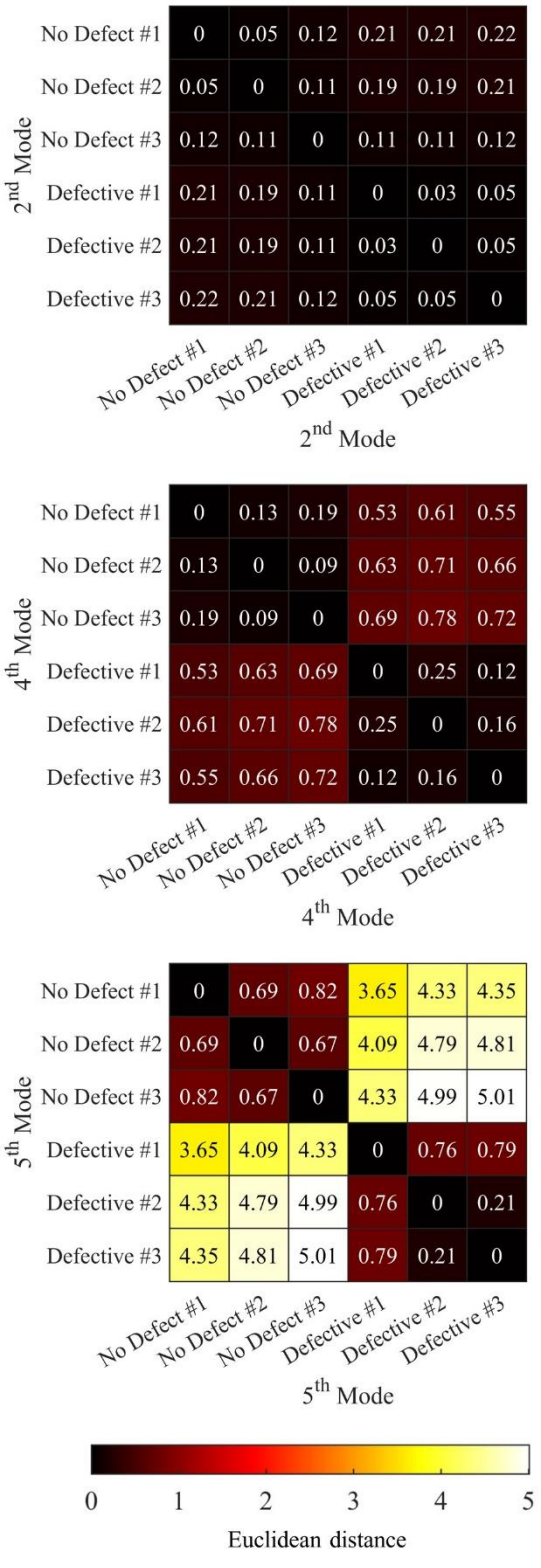

Figure 19: The correlation matrices showing the pairwise comparisons of the contours for the 2nd mode (top), 4th mode (middle) and 5th mode (bottom) for the whole set of specimens. Each value in the box is the Euclidean distance calculated between the feature vectors.

4.4. Discussion

The influence of in-plane waviness on the resonant frequencies was found to differ across various modes. As shown in Table 1, the disparities between the average resonant frequency of the defect-free and defective specimens at their 1st, 2nd, 4th, and 5th mode are less than 5%, and that the difference for the 3rd mode is approximately 8%. This variation can be attributed to the arrangement of fibre waviness, wherein the most misaligned fibres were oriented along the 90° fibre direction in the top ply, as illustrated in Figure 8. Consequently, this led to a significant alteration in the stiffness of the defective ply. Of all the modes, the 3rd mode exhibited the most substantial difference in average resonant frequencies, which aligns with the understanding that bending modes are particularly sensitive to fibre waviness [20]. Furthermore, it is consistent with previous findings that AF-ESPI is more responsive to defects at higher modes [8].

The nodal regions in each of the specimens are similar for the 1st, 2nd and 3rd modes, whilst more differences are observed for the 4th and 5th modes. This is based on visually inspecting the fringe patterns in Figure 12. The reason for selecting the nodal regions for comparison is that they are a key characteristic of a vibrating system, which is affected by changes in the stiffness of specimens due to the existence of defects such as fibre waviness. The procedure for extracting the nodal region is shown in Figure 13, where not only the general shape of the nodal region is extracted from the fringe patterns, but also the details of its contour are acquired. It should be noted that some of the roughness on the contours resulted from the measurement technique, which caused additional random electronic speckles in the fringe patterns. So, the extracted contour is a close approximation of the true nodal region. The aim of comparing the contours of mode shapes was to investigate if fibre waviness existed, so the focus was on comparing the general shape of the nodal regions, not small variations along the contour.

Rather than using intuition to select the number Fourier descriptors to use during decomposition, a new method was introduced in this chapter to identify whether the contour is accurately represented. Figure 15 and Figure 16 depict this method for selecting the optimal number of Fourier descriptors. The analysis showed that increasing the number of Fourier descriptors resulted in a reduction of mismatched facets until no mismatches were observed. Using the percentage of mismatched facets as a criterion for the acceptability of the

reconstruction is graphically straightforward and reliable. To identify the correct mesh density and mismatched facet threshold, a heuristic approach was applied. The chosen values were 2% of the contour size for the mesh density and 10% of the mismatched facets for the threshold. As discussed previously, the focus was to compare the general shapes of the nodal region, not the roughness of the contours, therefore the chosen values were appropriate for selecting a minimum number of Fourier descriptors whilst ensuring a reasonable quality reconstruction.

The reasons for using Fourier descriptors are: firstly, data dimensionality was reduced from 10^3 points representing the contour to 10^1 Fourier descriptors; secondly, using the same number of Fourier descriptors made the comparison easier; and thirdly, Fourier descriptors were found to be invariant to simple transformations of the contour. The contours for modes of different specimens are composed of various numbers of points from approximately 1200 to 1900, which makes direct comparison of contours difficult. Therefore, each contour was decomposed into 90 Fourier descriptors for easier comparison. Fourier descriptors in this chapter were made rotation invariant by using the absolute value of the terms, scale invariant by dividing each descriptor by $|F_1|$, and translation invariant by omitting the term $\frac{|F_0|}{|F_1|}$. This invariance was verified by decomposing the four contours at the 4th mode in Figure 17 and four contours at the 2nd mode. The comparisons made in Figure 18 show that no matter which one of the three modifications is made to the original contour of the 2nd mode and the 4th mode, the Euclidean distances between the contours of either the 2nd mode or the 4th mode are small, i.e., less than 0.3. These invariance characteristics provide more flexibility when performing the experiment. For instance, minor changes in fringe patterns may occur if the camera position or the attachment point of the stinger on the specimen is altered when switching between specimens. However, with the technique presented in this chapter, the feature vector of the transformed fringe pattern would remain relatively unchanged, enabling meaningful comparisons to be made despite these variations. It could also simplify the comparison of fringe patterns from experiments with simulated mode shapes, by eliminating the need to carefully align the datasets prior to making comparisons. The Euclidean distance between the contours of the 2nd mode and the 4th mode is three to four times larger than that between the contours of either the 2nd mode or the 4th mode, as shown in the correlation

matrix in Figure 18. This indicates that the technique can also be used to distinguish different mode shapes quantitatively.

The research demonstrates that the detection of in-plane fibre waviness can be achieved by comparing specific mode shapes using the Euclidean distance to assess similarity between two contours representing nodal regions in mode shapes. The contours for the 1st and the 3rd mode shape of all the specimens appear to be largely horizontal lines that lack significant features which can be used for comparison, therefore no correlation matrices were generated for these two modes. To quantify the contrast between defective and defect-free specimens in the correlation matrices displayed in Figure 19, the ratio r_i was introduced. The value of r_i increases as the vibration mode number increases, from 1.88 to 4.67, and then to 6.14 for the 2nd, 4th, and 5th mode respectively. This indicates that the presence of fibre waviness has no significant effect on the contours for the 2nd mode. However, both the 4th mode and the 5th mode show strong evidence that fibre waviness has a significant effect, and that the 5th mode is the most affected by waviness. The technique offers a high sensitivity that can discern differences between the fringe patterns that are not obvious. This is because by manually observing the fringe patterns for the 4th mode in Figure 12, the difference between the defect-free and defective specimens is not noticeable. However, the technique still captured this minor difference and generate the distinct correlation matrix shown in Figure 19. The study represents an advance compared with earlier work [8] because, not only are the differences in mode shapes caused by defects captured by AF-ESPI, but these differences are quantified. The technique is robust for identifying in-plane waviness in carbon fibre reinforced laminates, which could be further utilised as a quality inspection technique in industry for identifying defective components. The technique could also be used to quantify the severity of defects based on how much they change the mode shape of a component.

The timescales for acquiring resonant frequencies, obtaining fringe patterns of mode shapes, and image processing are of the order of seconds once the experimental set-up has been completed. Hammer-based modal analysis was adopted in this chapter for simplicity; however, the whole process of detection could be made into a fully automated system by changing the excitation method from hammer-based to loudspeaker-based. Thus, the technique could be developed to be contact-free and boost the detection efficiency further. Currently, the most commonly used non-destructive techniques for detecting fibre waviness

are ultrasonic C-scan [89], eddy current testing [29] and X-ray computed tomography [25]. Ultrasonic C-scan and eddy current testing require the movement of probes to scan every region of a component to identify the existence of defects, and the frequencies of the probes need to be changed often to achieve the desired penetration depths in order to generate a 3D fibre orientation map. These procedures are time-consuming and thus unsuitable for fast on-site inspections. X-ray computed tomography is not applicable for large components and special care needs to be taken due to radiation risks. Additionally, all three techniques demand a high level of expertise and detailed knowledge to analyze the generated images effectively and interpret whether the detected defects are critical or not. In contrast, the technique developed in this chapter, while not providing a full-scale image of the composite being inspected, offers increased efficiency and the ability to reveal the overall impact of waviness defects. Most importantly, it allows for the quantification of defect severities, which is crucial for establishing clear acceptance or rejection criteria for decision-makers.

4.5. Summary

A novel technique using AF-ESPI based modal analysis has been developed for identifying the existence of in-plane fibre waviness in carbon fibre reinforced laminates. Modal analysis was used to obtain the first five resonant frequencies, and the AF-ESPI technique was used to obtain the fringe patterns representing the corresponding mode shapes. The nodal regions were extracted from the fringe patterns using a specially-developed algorithm incorporating DBSCAN. Fourier descriptors were used to reduce data dimensionality and quantify the difference between contours of the nodal regions. A method for selecting an appropriate number of Fourier descriptors to represent a contour by a feature vector was also introduced, which can provide the minimum number such that the nodal region is acceptably represented. The method is based on thresholding the percentage of mismatched facets, which is graphically straightforward and robust. The contours of the nodal regions were compared by calculating the Euclidean distance between pairwise feature vectors, which showed that higher vibration modes can be used for identifying the presence of fibre waviness. This technique could be used for quality assurance of composite components after they have been manufactured. The first objective about developing a non-destructive technique for identifying and quantifying defects in composites thus has been

achieved. The characterisation of defects and the assessment on the performance of defective composites will be discussed in Chapter 5 and 6.

5. Prediction of residual strains due to in-plane fibre waviness

5.1. Introduction

As identified in the knowledge gaps, residual strains correlate strongly with the ultimate failure load of specimens containing fibre waviness [7]. Therefore, the measurement and prediction of residual strains is crucial for estimating the performance of composites. Some studies have reported that fibre waviness, based on non-destructive characterisation of fibre orientation, can be incorporated into 3D finite element models to predict the performance of composite structures [31], which indicates a route to also predicting residual strains in two steps: the generation of geometric ply information and simulations of the cooling process through which the residual strains are induced. However, to the author's knowledge, no prior studies have attempted to model residual strains in composite specimens that contain fibre waviness.

This chapter introduces a method of generating finite element models for predicting residual strains in defective carbon fibre composites based on fibre orientation data measured using ultrasound. Three algorithms: RT, FFT and Sobel filters, were used to process the ultrasound images to reveal fibre orientation data. A novel technique based on stratified leave-one-out cross validation was used for quantifying the performance of the models, which was calculated as the Euclidean distance between feature vectors representing the predictions and measurements. The identification of the optimal parameter values for the models was also investigated by finding the minimum Euclidean distance. The findings in this chapter demonstrate that stratified leave-one-out cross validation is effective for comparing the performance of algorithms and thus identifying the best algorithm for generating finite element models.

This chapter is based on the following paper, written by the author of this thesis:

Xiaonan Li, E.A. Patterson, Wei-Chung Wang, W.J.R. Christian. "Prediction of residual strains due to in-plane fibre waviness in carbon-fibre reinforced polymers using models based on ultrasound data". *Journal of Nondestructive Evaluation*. 42(1):2, 2022. The entire original draft of the paper was written by Xiaonan Li. The contribution of Xiaonan Li to this paper also include conceptualization, methodology, investigation, software. Xiaonan Li has obtained the

agreement from the other authors to include the contents from the published work in this thesis.

5.2. Experimental Methods

5.2.1. Specimen preparation

Quasi-isotropic carbon fibre reinforced laminates, with a stacking sequence of $[0_2/90_2/45_2/\text{-}45_2]_s$, were manufactured using RP507UT210 prepreg (PRF, UK). Specimens were made using a set of aluminium formers with various shapes to induce fibre waviness, and one of the formers is shown in Figure 20. The central arc radius of the former and the thickness of the uncured specimen affect the waviness severity and this is discussed in detail in [7]. Each ply was laid on top of an aluminium former in a predetermined stacking sequence to create a laminate. The arc-shaped laminate was then removed from the former and flattened by hand. During this process, the fibres of the top ply buckled to accommodate the length difference between the top and the plies beneath it, leading to localized in-plane waviness defects at the centre of each specimen in the top 0° ply. Following the flattening process, only minor levels of out-of-plane waviness were observed. In a previous study [7], a similar specimen was sectioned, and no in-plane waviness was found below the top 0° ply. Therefore, compared with the severity of the in-plane fibre waviness, the out-of-plane waviness was assumed to be insignificant. The severity of the in-plane fibre waviness, referred to as nominal waviness, was quantified based on the thickness of the laminates before curing, t_u, and the central arc radius, r, using,

$$Nominal\ Waviness = \frac{t_u}{r + t_u} \tag{16}$$

Given that the thickness of the uncured laminates for a given stacking sequence did not change significantly, the nominal waviness can thus be varied by changing the central arc radius of the former, r. Three levels of nominal fibre waviness were induced in a set of specimens: 17.5%, 20% and 25%, with six specimens having each level of waviness giving 18 specimens in total. The formers for creating the three levels of nominal fibre waviness had central arc radii of 17.2 mm, 14.6 mm, and 11.0 mm respectively.

The laminates were cured in a hot press (APV-2525, Meyer, Germany), according to the manufacturer's instructions. Specifically, they were heated up to 130 ℃ from room

temperature (23 °C), with a heating rate of 10 °C/min. After heating, they were held at 130 °C for 45 min. The hot-press pressure was set to 2.5 bar during heating, curing and cooling. Once the laminates were cured, the hot press was left to cool to room temperature. The laminates were cooled naturally while the press was in the closed position, and the cooling rate was approximately 10 °C/h. After removal from the hot press, each specimen was cut by a wet diamond saw (Versatile 103450, Vitrex, USA) into a size of 220 mm by 40 mm, with the 0° fibres orientated parallel to the x-direction, as shown in Figure 21. The average thickness of all specimens was 2.96 mm.

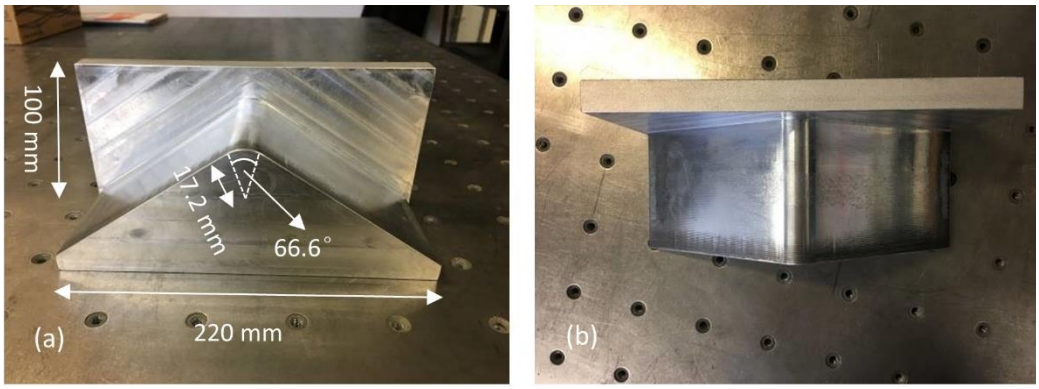

Figure 20: An aluminium former for creating localised fibre waviness shown from the front (a) and top (b).

Figure 21: An exemplar 220 mm by 40 mm quasi-isotropic specimen with a $[0_2/90_2/45_2/\text{-}45_2]_s$ layup showing the speckled region. The 0° fibres were orientated parallel to the x-direction.

5.2.2. Digital image correlation characterisation

Digital Image Correlation (DIC) was employed to measure the out-of-plane deformation of laminates upon cooling, enabling the calculation of surface strains. The calculated surface strains were used as benchmarks for validating the finite element models. The specimens were prepared for DIC measurements by applying a speckle pattern to an 80 mm by 40 mm area on the face of the specimen opposite to the side with induced waviness. The process involved spraying the specimens with white paint (Matt White,

PlastiKote, USA) followed by spraying black speckles (Pro Paint Acrylic Black Matt, CRC, USA) on top. This resulted in a pattern typified by the one shown in Figure 21, where the nominal diameter of the black speckles was 0.25 mm. To capture the images, a Q-400 DIC system (Dantec Dynamics, Germany) was utilized, comprising two digital cameras (Stingray F-125, Allied Vision, Germany) positioned 140 mm apart. The stereo angle between the two cameras was 52°. Illumination was provided by a light emitting diode lamp (Dantec Dynamics, Germany). The images were processed by the Istra software (Dantec Dynamics, Germany) using a facet size of 23 pixels and grid spacing of 15 pixels. The residual strains were calculated from the shape data measured using the DIC system as [90],

$$\varepsilon_{x,res} = -\frac{t_c}{2}\frac{\partial^2 w}{\partial x^2} \tag{17}$$

where $\varepsilon_{x,res}$ is the residual strain in the x-direction, t_c is the cured thickness of the specimens, and w is the out-of-plane displacement from a flat plane. Equation (17) was applied to shape data obtained from both the DIC measurements and the predictions from finite element models. A central difference method was used to estimate the second partial derivative of the out-of-plane displacement as,

$$\frac{\partial^2 w}{\partial x^2} \approx \frac{w(x+h) - 2w(x) + w(x-h)}{h^2} \tag{18}$$

using a step size, h, of 9 mm.

The measurement uncertainty of the DIC system was obtained by calculating the root mean square of the surface strains of a quasi-flat surface from a block specimen made of rolled steel. For a flat surface, the measured residual strains should be zero, while the root mean square of the measured strain for the quasi-flat steel was calculated to be 66.6 με. Therefore, the measurement uncertainty was taken as 66.6 με. DIC can only provide information about the surface shape and deformation of the laminate and cannot be used to characterise the fibre waviness; hence, this was performed using ultrasound.

5.2.3. Ultrasonic Inspection

Pulse-echo ultrasonic C-scans were used to characterise the fibre waviness in the specimens. Each ply in the laminate featured a thin resin-rich layer that separated adjacent plies. This resin-rich layer reflects the ultrasound and the amplitude of the reflection is

approximately proportional to the thickness of the layer; hence, an amplitude C-scan corresponds to a map of resin-layer thickness. The thickness of the resin layer contains an imprint of the fibre tows in the plies above and below the layer. Ultrasound cannot resolve individual fibres because they are very thin (5~50 μm), so only fibre tows, which consist of bundles of fibres, can be resolved. The width of the fibre tows was approximately 0.6 mm. In this chapter, a focused 10 MHz probe attached to a flaw detector (Epoch 4+, Olympus, Japan), was used to record the variation in amplitudes of the reflections received from the specimens. The choice of frequency was a critical consideration as it impacted the resolution and focal sharpness, with higher frequencies providing better resolution but reduced penetration power [91]. For the defective specimens in this chapter, the in-plane fibre waviness was only significant in the top 0° ply with a thickness of approximately 0.37 mm, thus the required penetration depth can be easily achieved and permitted the use of a high frequency probe. Each specimen was immersed in a water tank with the wavy side faced up, and the probe was placed vertically above the specimen with no tilt angle. The probe crystal diameter was 10 mm and the focal length was 50 mm. The probe was moved along a raster pattern by a multi-axis scanner (Midas-NDT, UK), as shown in Figure 5. The system was set to record the instantaneous amplitude from a 0.1 mm thick portion of the specimen at a depth of 0.37 mm, which is approximately equal to the depth of the first ply interface. This resulted in images showing the tows in the defective ply of the specimen. The amplitude was recorded at 0.1 mm increments along lines with a spacing of 0.2 mm. The images had a lateral spatial resolution of 10 pixels/mm.

5.3. Characterisation of fibre orientation and finite element analysis

A time gate was applied to only detect the reflected amplitude at the interface of the front ply, which resulted in C-scan images of the ply with a depth of 0.37 mm. A C-scan ultrasound image, $f(x, y)$, can be represented in greyscale so that the fibre tows can be observed in the texture of the image, as shown in Figure 22(a). To measure the fibre orientations, a multi-step process was employed. Initially, the ultrasound image was divided into several square facets that overlapped each other. Subsequently, each facet underwent processing using one of three algorithms: the Radon transformation (RT), 2D Fast Fourier transformation (FFT), and Sobel filters (SF). A 2D fibre orientation map was obtained by combining the orientation data of every facet. To determine the optimal facet size for

characterising the ultrasound images, nine facet sizes were explored for the three algorithms where the length dimension of the facets was varied from 5 pixels (0.5 mm) to 85 pixels (8.5 mm) and was optimised using an algorithm described later in this section. The grid spacing of the facets was kept constant at 1 mm.

5.3.1. Radon transformation-based algorithm

The Radon transformation (RT) was applied to the ultrasound facets of all the specimens to reveal fibre orientation. The basis of the RT is an integral transform of $f(x,y)$ along lines defined by θ and r, where θ is the angle between the lines from the centre of $f(x,y)$ and the *x*-direction, and r is the distance from the facet centre. The Radon transform is defined as,

$$R(r,\theta) = \iint f(x,y)\delta(xcos\theta + ysin\theta - r)dxdy \tag{19}$$

where δ is the Dirac delta function, which allows the summation of $f(x,y)$ along the θ direction, and θ ranges from 0° to 180°. The dominant fibre orientation corresponded to the projection angle where the variation in image intensity was a maximum. The absolute first derivative along every angle, $G(r,\theta)$, was calculated using an equation derived based on the method described in [35, 36],

$$G(r,\theta) = \left|\frac{[R(r+1,\theta) - R(r-1,\theta)]}{2}\right| \tag{20}$$

The angular distributions, $a(\theta)$, were then obtained by calculating a sum along each projection divided by the total for every projection,

$$a(\theta) = \frac{\sum_{r=1}^{N} G(r,\theta)}{\sum_{r=1}^{N}\sum_{\theta=1}^{180} G(r,\theta)} \tag{21}$$

where N is the number of points for each projection.

5.3.2. 2D fast Fourier transformation-based algorithm

The 2D fast Fourier transformation (FFT) was used to characterise the fibre orientations for all the specimens. The ultrasound facets in the spatial domain, $f(x,y)$, were transformed using the 2D fast Fourier transform into the frequency domain, $F(u,v)$. Before performing the FFT, a radial Hahn window was applied to reduce the spectral leakage and

give a broad peak at the centre of the frequency spectrum [7]. An angular distribution was then calculated by radially summing the pixel intensities from the centre of the FFT transformed image $F(u, v)$, based on the equation [33],

$$a(\theta) = \sum_{L=1}^{D/2} F(N/2 + r\cos\theta\,,\quad N/2 - r\sin\theta\ ) \tag{22}$$

where D is the facet length, r is the distance from the centre and θ is the angle between the radius and the x-direction, and θ ranges from 0° to 180°.

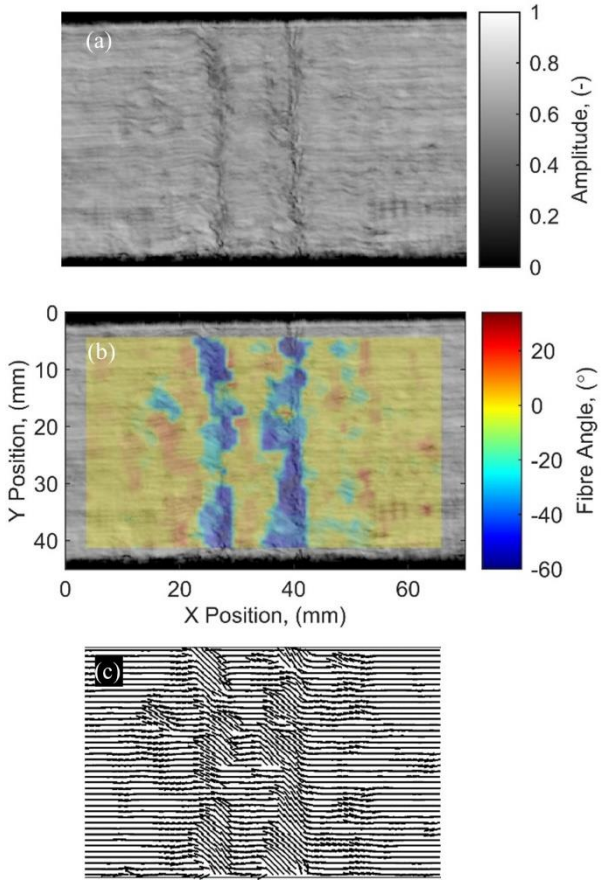

Figure 22: An ultrasound image of the inspected region on the front surface of a 25% nominal waviness specimen (a), the fibre orientation map for the specimen calculated using the Fourier transform based algorithm (b), and the orientations as input into the finite element model (c).

5.3.3. Sobel filter-based algorithm

Sobel filters (SF) were employed to process ultrasound facets for all the specimens, enabling the determination of fibre orientations. SF is an edge detecting algorithm which is widely used in image processing and computer vision. The principle is to calculate the gradients in an image by convolving the image with two Sobel filters [92]. These filters were

respectively used to calculate the gradients along the x-direction and y-direction: $S_x(x, y)$ and $S_y(x, y)$, and then the fibre orientation was calculated using the equation,

$$\theta(x, y) = round\left(arctan\frac{S_x(x, y)}{S_y(x, y)}\right) \quad (23)$$

The $round$ function was used to round off the resulting orientations into 180 integers from 1° to 180°. After convolving an ultrasound facet with Sobel filters, the facet was transformed into a map of fibre orientations. An angular distribution $a(\theta)$ thus can be obtained by computing the histogram of $\theta(x, y)$. The facet size affects the spatial resolution of the orientation map. A smaller facet size resulted in a high spatial resolution orientation map, but also produced more noise, while a larger facet size led to less noise, but a lower spatial resolution.

5.3.4. Finite Element Analysis

The characterization of fibre waviness began with C-scans, and the resulting images were further analysed using the three algorithms to obtain fibre orientations. These fibre orientations were then incorporated into finite element models. The finite element models were created using Abaqus 6.14 (Dassault Systèmes, France), and employed to simulate the deformation of the specimens after cooling from the curing temperature to room temperature. Each specimen was simulated using 70,400 C3D8R elements. These elements were initially given the transversely isotropic material properties shown in Table 2 [93]. The temperatures for the initial and final conditions were set at 130 ℃ and 23 ℃, respectively, for the entire specimen. To simulate the defect, a discrete field was created at the centre of the top 0° ply, with the number of elements in this discrete field matching the number of data points in the orientation map. Then the measured local fibre orientation was assigned to each element in the discrete field. Stratified leave-one-out cross validation (SLOOCV) was used to identify the optimal facet size for the fibre measurement algorithms and the coefficient of thermal expansion required for the finite element models. The method was also used to evaluate the performance of the calibrated models.

Table 2: Material properties of a similar composite material to the one used in this chapter [93], E_i represents Young's modulus; ν_{ij} represents Poisson's ratio; G_{ij} represents shear modulus.

E_1 (MPa)	E_2 (MPa)	E_3 (MPa)	ν_{12}	ν_{13}	ν_{23}	G_{12} (MPa)	G_{13} (MPa)	G_{23} (MPa)
132,000	10,300	10,300	0.25	0.25	0.38	6500	6500	3910

As described in [12], one possible cause of the formation of residual stresses in composites is the difference in the coefficients of thermal expansion in the transverse and longitudinal directions for different plies at the macro-mechanical level. Therefore, in the present research, the major focus of optimising the finite element model was to calibrate the coefficients of thermal expansion. The coefficients for the unidirectional plies to be calibrated were in the fibre longitudinal direction, α_1; the transverse direction, α_2; and along the thickness direction, α_3. As the unidirectional plies can be considered transversely isotropic, α_2 was set to be equal to α_3. The coefficient of thermal expansion for carbon fibres is very small compared with the epoxy matrix, resulting in α_1 of a unidirectional ply being more than one order of magnitude smaller than α_2 and α_3 [94]. This causes α_1 to have a negligible effect on the residual strains and thus is often not considered when calculating residual strains [95]. Therefore, when optimising the models, only one parameter, α_2 (equal to α_3) was calibrated.

The procedure for calibrating and evaluating the finite element models is shown in the flow chart in Figure 23. Ultrasonic C-scan data from the 18 specimens were processed using the RT, FFT, and the SF algorithms to generate finite element models to predict residual strains, and DIC measurements from the 18 specimens were used to determine residual strains on the surface. The ultrasound and DIC data were firstly divided into three classes according to their nominal waviness levels, and then were split into six data sets, with each set having a dataset from one specimen selected randomly from each class. Five sets were then used to calibrate the models and one set was used to evaluate the performance of the models. Both the calibration and evaluation processes involved comparing the measured residual strains with the simulated residual strains obtained from the finite element models. Residual strain calculations were performed using Equation (17) and were based on the surface displacements measured by DIC. The finite element model's simulated strains were calibrated against the measured strains obtained from DIC. The calibration and evaluation

were conducted for two parameters. The first parameter was the facet size used for the fibre orientation algorithms, which was varied from 5 pixels to 85 pixels with a step size of 10 pixels. The second parameter that was calibrated was the coefficient of thermal expansion along the transverse direction. This was performed by varying α_2 across a predefined range: 1×10^{-6} °C^{-1} to 10×10^{-6} °C^{-1}, with a step size of 0.1×10^{-6} °C^{-1}. The range was defined based on a typical transverse coefficient of thermal expansion for a unidirectional ply, which is on the order of 10^{-6} °C^{-1} [96]. A sensitivity study on the coefficient showed that outside this range the differences between the measured and predicted fields of residual strain either monotonically increased or decreased. The differences between the measured and predicted fields of residual strain were quantified by representing each field using a feature vector, S_E and S_M respectively and calculating the Euclidean distance $d(S_E\ ,\ S_M)$ between the vectors,

$$d(S_E,\ S_M) = \|S_E - S_M\| \tag{24}$$

where $\|\cdot\|$ is the vector norm, which is the square root of the sum of the squared elements [97]. The Euclidean distance is the minimum distance between two vectors in multi-dimensional space [97], and was used as a measure of concordance between S_E and S_M. This distance quantified the extent to which the predictions accurately represented the measurements. The feature vectors were obtained using the image decomposition method described in [82]. Based on prior experience, Chebyshev polynomials of order ten were used to decompose the maps of measured and predicted residual strains. The appropriateness of using polynomials of this order was evaluated by comparing the accuracy of the reconstructed images with the original maps. The root mean squared difference between the original maps and the reconstructed maps was calculated and considered acceptable when it fell below the measurement uncertainty. The Euclidean distance between the feature vectors S_E and S_M for every specimen in the five calibration sets, for facet sizes from 5 pixels to 85 pixels and α_2 values from 1×10^{-6} °C^{-1} to 10×10^{-6} °C^{-1}, was calculated. The average Euclidean distance of the specimens in the calibration sets for every one of the nine facet sizes was calculated. The optimum facet size and value of the coefficient of thermal expansion after calibration were identified, which corresponded to the minimum of the average Euclidean distance achieved for the five calibration sets. To validate the quality of the combined fibre-orientation algorithm and model, the feature vectors from the measured and predicted residual strain maps were compared for the validation set using the optimized facet size and coefficient of

thermal expansion obtained from the calibration sets. The calibration and validation process were iterated six times, where each data set was used to calibrate the model five times and validate it once. Automation of the entire process was achieved by utilizing Abaqus for finite element analysis, Python for post data processing on finite element results, and MATLAB for image processing, including image decomposition.

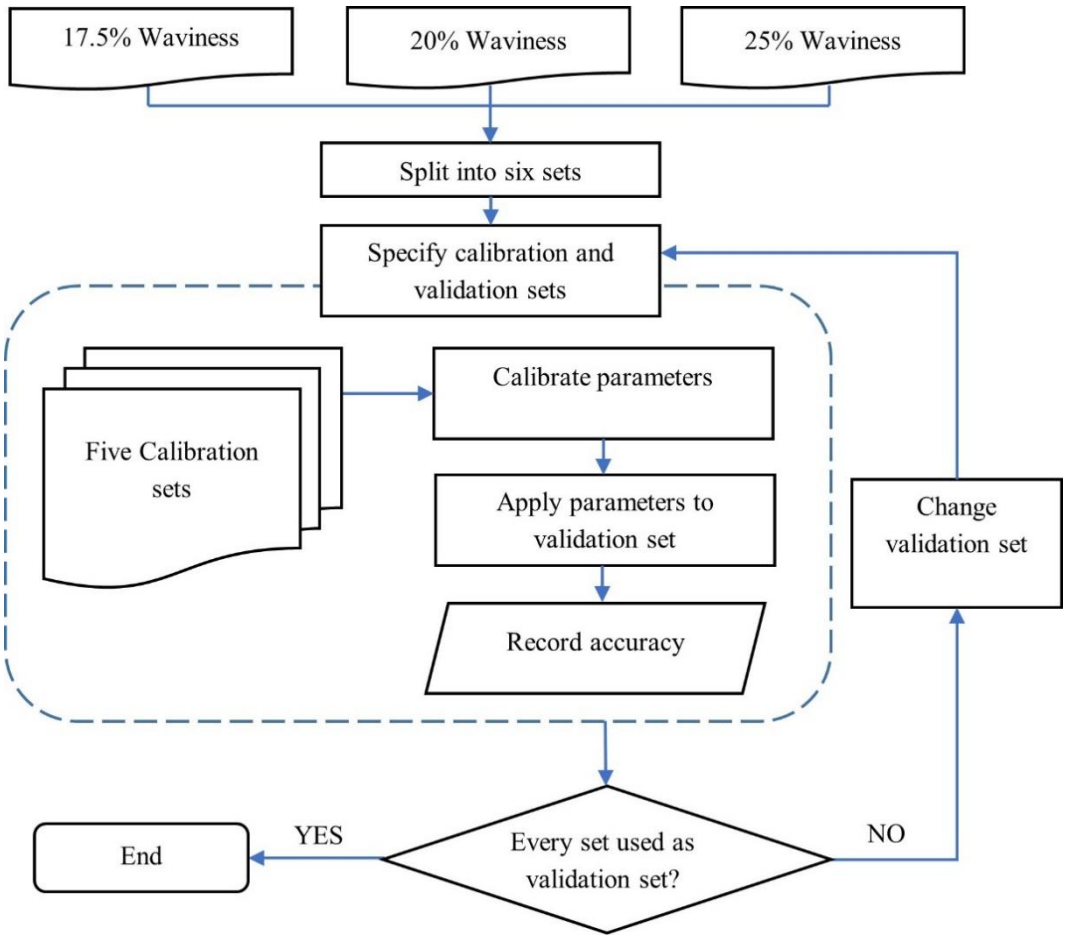

Figure 23: Flow chart showing the SLOOCV procedure used to calibrate the ultrasound facet size and the coefficient of thermal expansion.

5.4. Results

An example of an orientation map obtained using the FFT based algorithm is shown in Figure 22(b), which indicates that the fibre waviness region was successfully characterised resulting in a fibre orientation map. Figure 22(c) shows a sketch of fibre alignment on the front surface of the finite element model after importing the fibre orientation map into Abaqus. To evaluate the performance of the three algorithms for identifying fibre orientation from C-scan data, they were applied to a 100×100-pixel exemplar ultrasound facet, $f(x, y)$, for which the orientation was created by rotating 30° anticlockwise the image of the top 0°

ply of a non-wavy specimen, as shown in Figure 24(a). Figure 24(b) to (d) are images for each algorithm applied to Figure 24(a), and the angular distributions $a(\theta)$ were calculated based on these images. For a better comparison of the angular distributions from the RT, FFT and SF algorithms, they were normalized by calculating,

$$z(\theta) = \frac{a(\theta) - \mu}{\sigma} \tag{25}$$

where $z(\theta)$ is the normalized angular distribution from the RT, FFT and SF, $a(\theta)$ is the original angular distribution from the RT, FFT and SF, μ and σ are the mean and standard deviation of $a(\theta)$. These were then plotted in Figure 24(e). The three peak values in Figure 24(e) achieved by the RT and FFT are both at 30 degrees, and at 24 degrees for the SF.

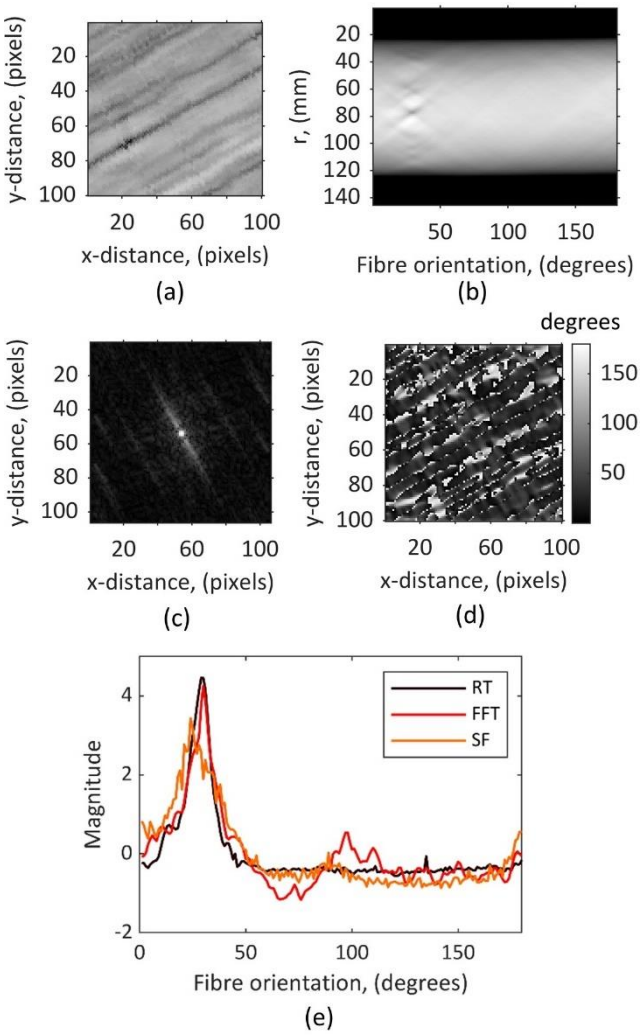

Figure 24: A facet of ultrasound data from a specimen without fibre waviness (a) where the image has been rotated by 30°. Images after performing RT (b), FFT (c), and SF (d). Normalised angular distributions for performing RT, FFT and SF (e).

Calibration results for the first iteration are shown in Figure 25, illustrating the effects of facet size and the value of the coefficient of thermal expansion on the average Euclidean distances between the measured and predicted residual strains. The curves show the mean value of the Euclidean distances between the feature vectors representing the predicted and measured residual strains for each specimen in the five calibration sets at a specific facet size and value of the coefficient of thermal expansion. The relationship between the minimum coefficients of thermal expansion and facet size is shown in Figure 26. The minimum of each curve in Figure 25 was plotted in Figure 27 as a function of facet size in order to identify the global minimum and hence optimum facet size. For RT, FFT and SF algorithms, the minimum Euclidean distances were achieved when length dimension of the facet was 45 pixels, 35 pixels and 15 pixels respectively.

Validation of the calibrated models was performed using the six validation sets and each set had three specimens with 17.5%, 20% and 25% fibre waviness, yielding 18 validations in total. The calibrated values of the coefficient of thermal expansion and the facet size were used to generate the models to be validated. Each validation included three comparisons of measured residual strains with predicted residual strains obtained from models using the RT, FFT and SF based algorithm respectively, using the protocol described by the CEN Workshop Agreement 16799:2014 [82]. One example of validation is shown in Figure 28. Figure 28(a) shows the measured residual strains for a specimen with 25% nominal fibre waviness, and Figure 28(b) to (d) show the predicted residual strains for the specimen based on models using the RT, FFT, and SF based algorithms. The residual strain maps were treated as images and decomposed using discrete Chebyshev polynomials of order 10, resulting in 66 coefficients collated into feature vectors. The image decomposition technique was applied to reduce data dimensionality, i.e. from 10^3 pixels to 10^1 coefficients, and to allow for a straightforward comparison using the feature vectors rather than comparing images pixel by pixel. The feature vectors were used to reconstruct the original images and assess the quality of the representation of the original images by calculating the root mean squared residual between the original image and the reconstructed image. Comparisons of the feature vectors representing measurements and the predictions are shown in Figure 28(e). To determine if the simulation was an adequate representation of the experiment, the root mean squared residual and measurement uncertainty were used to define an acceptance band, which is graphically shown as the two dashed lines in diagrams shown in Figure 28(e). The acceptance band is defined as,

$$S_M = S_E \pm 2\sqrt{u_{meas}^2 + u_E^2} \tag{26}$$

where S_M is the feature vector describing the predicted residual strains, S_E is the feature vector representing the measured residual strains, u_E is the root mean squared residual for the measured strains, and u_{meas} is the measurement uncertainty. A perfect correlation between the measurements and a prediction would result in all of the points being located in the acceptance band and in a straight line. However, in Figure 28(e), there was one data point for each of the RT, FFT, and SF which fell outside the acceptance region.

Three models used for predictions of residual strains generated results which were deemed unacceptable in the validation process, these were all associated with one specimen containing 25% nominal waviness. The validation diagram for these three models is shown in Figure 28. The comparisons of residual strains between the predicted data and the measured data indicate that whilst the distribution in the high strain areas were similar, differences existed in the magnitude of strains. Each validation set contained three specimens with 17.5%, 20% and 25% nominal waviness, thus the averages and standard error of the Euclidean distances were investigated as a function of the nominal waviness, as shown in Figure 29. The Euclidean distance between the predicted and measured strains increased with the increase in nominal waviness in the specimens. At lower values of nominal waviness: 17.5% and 20%, the Euclidean distances achieved by the RT, FFT, and SF were approximately the same, however, at the highest nominal waviness of 25%, the Euclidean distances achieved by the SF were larger, indicating less agreement.

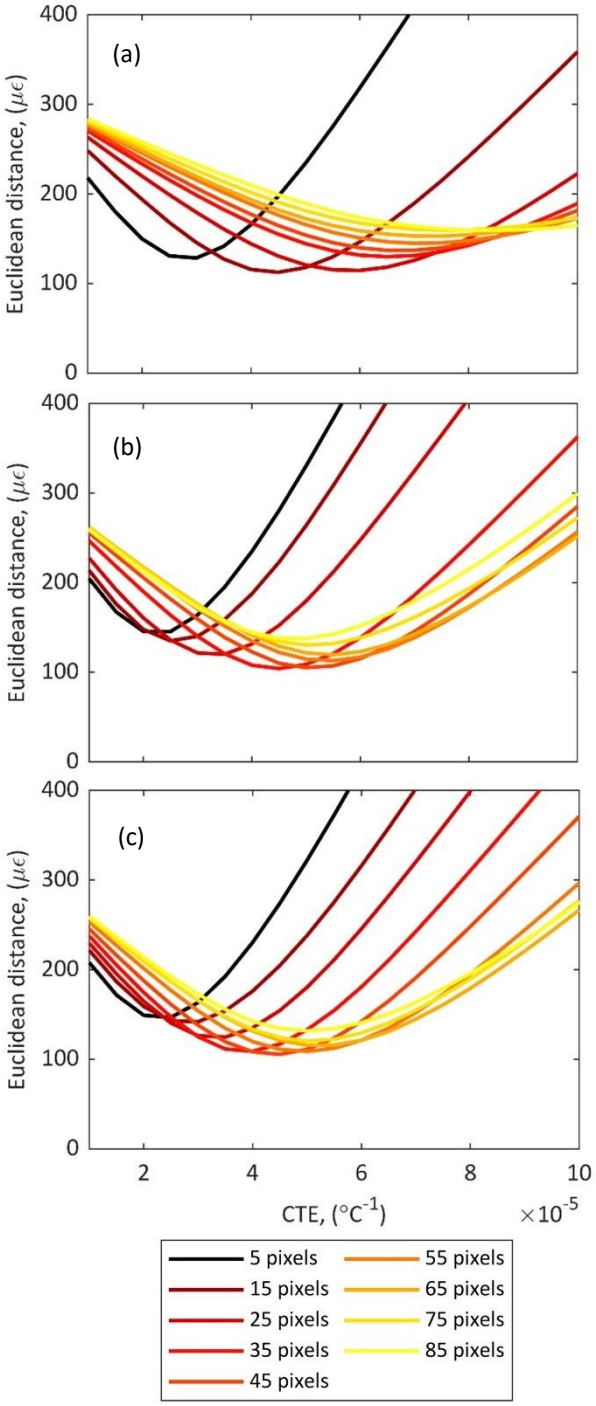

Figure 25: Summary of one calibration iteration using (a) RT, (b) FFT, (c) SF algorithm, showing the influence of CTE and facet size on the Euclidean distance between feature vectors representing the predicted and measured residual strain maps. Each curve represents the average Euclidean distance of the five calibration sets containing 15 specimens for each facet size.

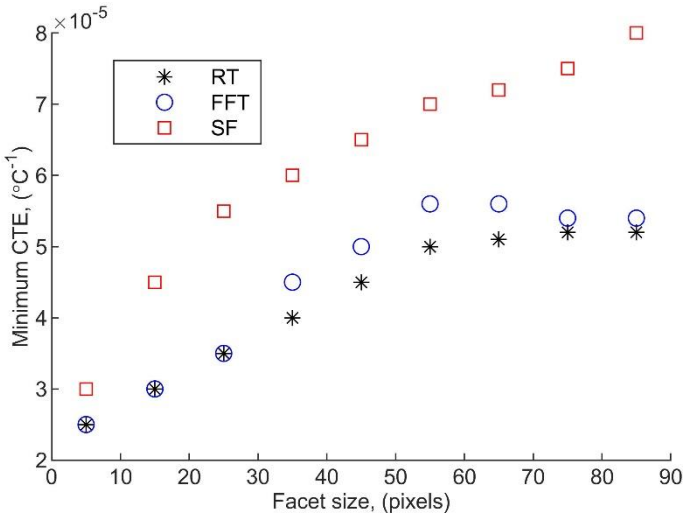

Figure 26: Minimum coefficients of thermal expansion from Figure 25 plotted against facet size for the algorithms based on the Radon transform, Fourier transform, and Sobel filters.

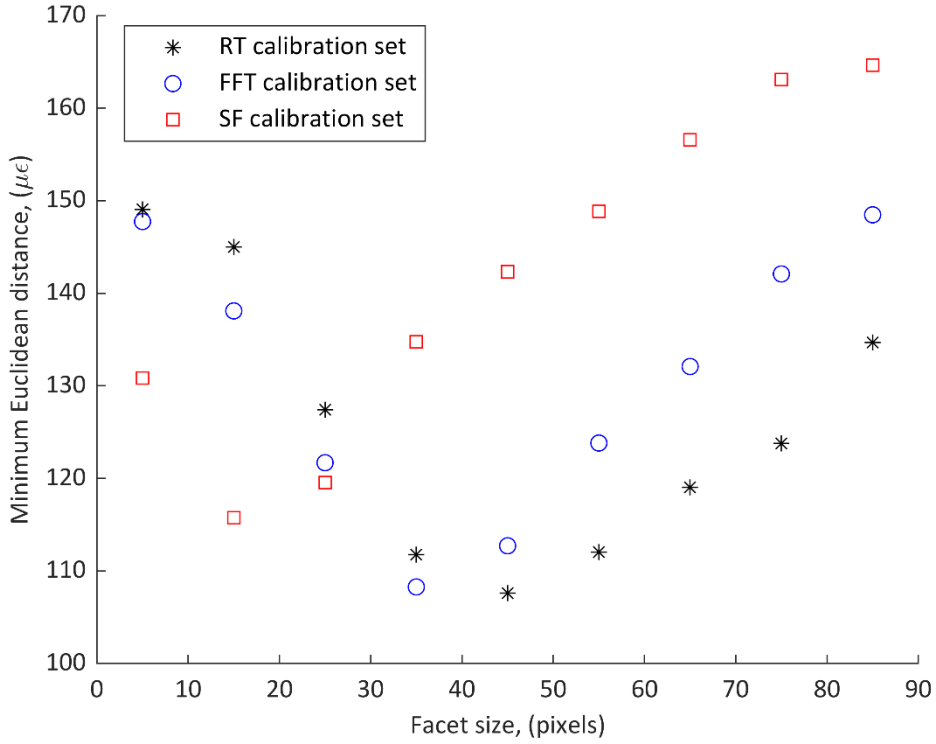

Figure 27: Minimum Euclidean distances from Figure 25 plotted against facet size for the algorithms based on the Radon transform, Fourier transform, and Sobel filters.

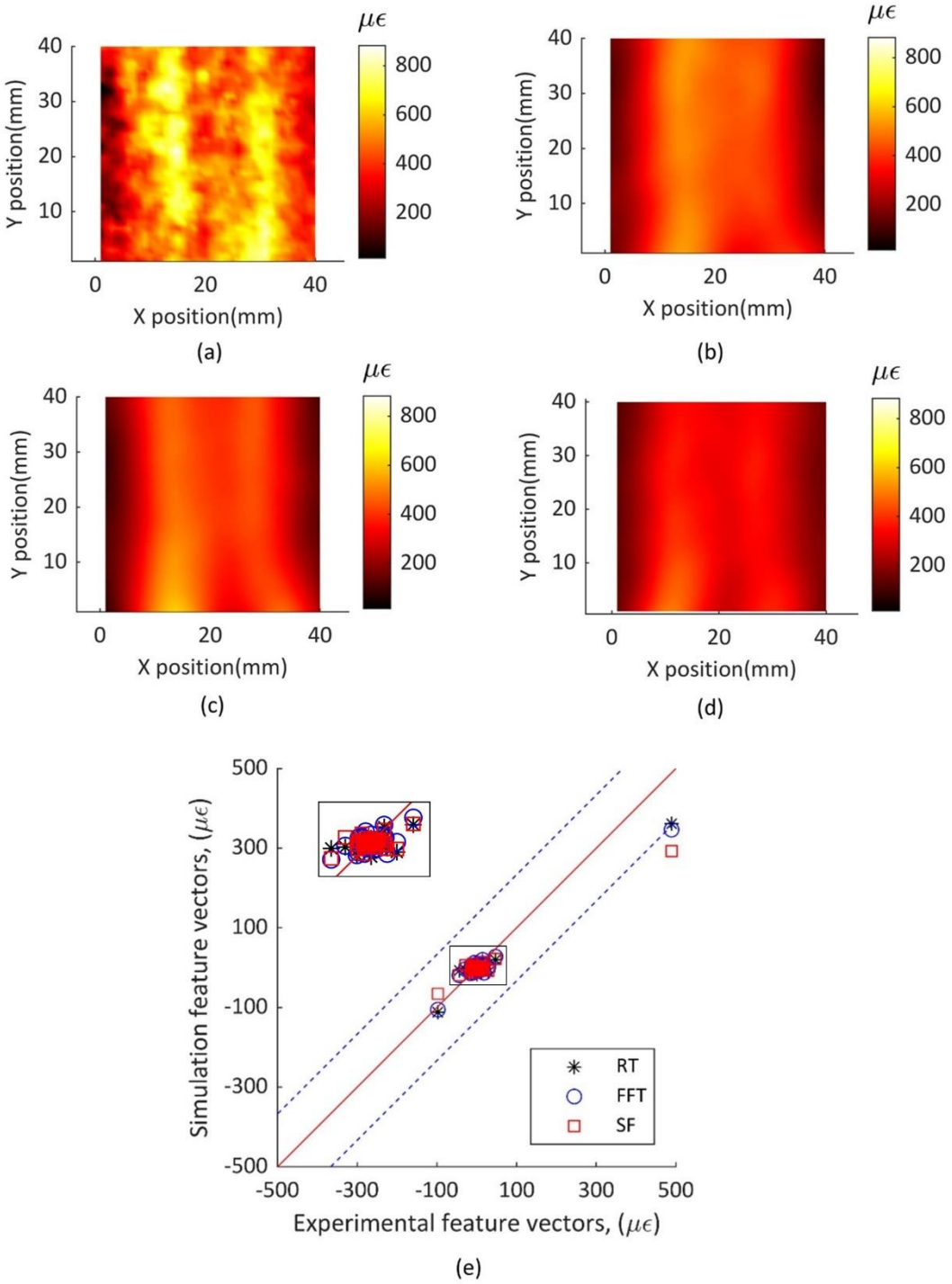

Figure 28: Experimentally measured residual strains for a specimen with 25% nominal fibre waviness (a), predicted residual strains for the specimen using the Radon transform (b) Fourier transform (c) Sobel filters (d), and the validation diagram (e) showing that three points fell outside the acceptance region. The validation diagram was plotted as the three feature vectors representing the predicted strains against the feature vector representing the measured strain. Each feature vector consisted of 66 coefficients of the Chebyshev polynomials used to decompose the strain maps (a)~(d). The inset shows an enlarged version of the boxed region on the main graph.

For each specimen, three models were created using the RT, FFT, and SF algorithms. For each model, a Euclidean distance between the feature vectors representing the predicted

and measured residual strains was calculated that quantified the similarity between the model and the experiment. The performance comparisons of the three algorithms could be made based on the prediction accuracy of residual strains. The best performing algorithm for predicting the residual strains was identified by finding the minimum of the three Euclidean distances. For 10 specimens the predicted residual strains were closest to the experiment when using the RT algorithm, this is the highest success rate in providing the best predictions for any algorithm, as shown in Figure 30.

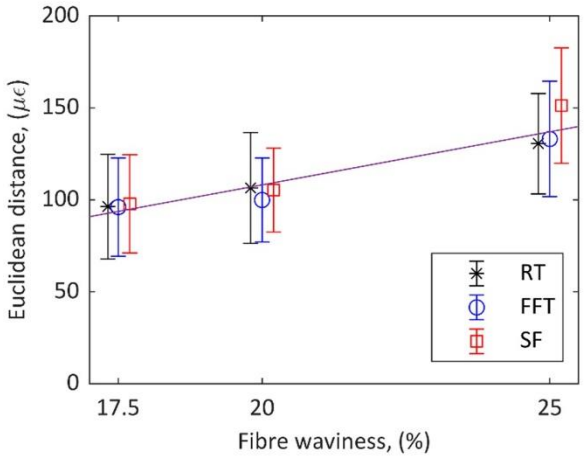

Figure 29: Average Euclidean distances between feature vectors representing predicted and measured residual strain maps from all 18 validation procedures for the RT, FFT, and SF algorithms plotted against waviness severity, with the 95% confidence intervals of the average shown as error bars. The markers are slightly offset from their true nominal waviness to aid interpretation and a trend line is plotted to show an approximately linear relationship.

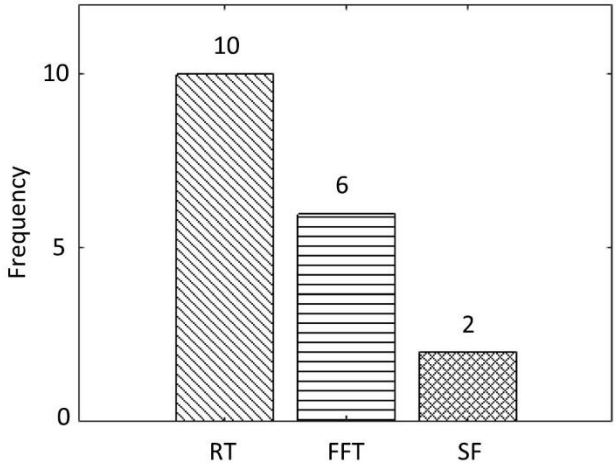

Figure 30: Frequency of minimum Euclidean distance between feature vectors representing predicted and measured residual strain maps achieved for the three algorithms applied to the 18 specimens using the optimised values of ultrasound facet size and of the coefficient of thermal expansion. Higher frequency indicates the higher success rate of the algorithm in providing the best predictions.

5.5. Discussion

5.5.1. Comparison of the RT, FFT and the SF based algorithms

Three algorithms were used to process an ultrasound facet with a known fibre orientation of 30° to assess their performance. The mechanisms of the three algorithms were different; however, all of the algorithms were able to characterise the fibre orientation of the same ultrasound facet by identifying the peak location, shown in Figure 24(e). Upon comparison, it was observed that the fast Fourier transform (FFT) based and Sobel filter (SF) based algorithms exhibited more noise in their results when compared to the Radon transform (RT) algorithm. The SF also shows a 6° deviation in peak values. This suggests that the RT algorithm was better at characterising ultrasound images for specimens with regularly aligned fibres, because it can give a more distinct peak at the correct fibre orientation with less noise.

Assessing the performance of the three algorithms on specimens with fibre waviness posed challenges due to the random variability in imaging fibre tows at the defective zones. This variability made it difficult to define a direct criterion for evaluating algorithm performance. However, the performance comparisons of the three algorithms could be made based on the prediction accuracy of residual strains. Algorithms based on the RT, FFT, and SF were applied to characterise the fibre orientations visible in ultrasound images of specimens containing fibre waviness. Finite element models of these specimens were created based on this orientation data and used to predict residual strains. To explore the influence of facet size used for determining fibre orientation, Stratified Leave-One-Out Cross-Validation (SLOOCV) was employed to estimate the prediction accuracy of the models. This was achieved by calibrating the facet size and the coefficient of thermal expansion for each algorithm. The effect of facet size can be seen in Figure 25, where the Euclidean distance between feature vectors representing the predicted and measured residual strains was used as an indicator for the quality of the result. Lower average Euclidean distances indicated a better fit of the model to reality for the given parameters. Both facet size and coefficient of thermal expansion contributed to the prediction accuracy and the relationship between them is shown in Figure 26. The correlation between facet size and CTE is due to larger facets resulting in small features in the ultrasound images being unresolved. This leads to an underestimation of fibre orientations, as also reported in [37]. Consequently, the calibration process yields higher

estimates of CTE in order to achieve the same magnitude of residual strains. The models were validated with the calibrated facet size and value of the coefficient of thermal expansion. After the validation of the models, average Euclidean distances were calculated, as shown in Figure 29. The average distance is an unbiased estimator of the predictive accuracy of the base model procedure [98]. Therefore, by identifying the predictions most similar to the experimental results, the best algorithm for characterizing fibre orientations can be determined.. The identification was achieved by finding the lowest average Euclidean distance between predictions and experimental results.

The comparison of the three algorithms was performed at two scales: fibre tows and specimen. There were 6 specimens at each of the three levels of nominal waviness, resulting in 18 specimens in total. At the fibre tow scale, the RT and FFT algorithms exhibited similar performance, with approximately equal average Euclidean distances observed at each nominal waviness level,, as shown in Figure 29. For lower values of waviness: 17.5% and 20%, the Euclidean distances obtained using the SF were close to those using the RT and FFT, where the differences among the three algorithms were within 5%. However, at the highest value of nominal waviness, the Euclidean distance achieved by the SF based models was approximately 16% larger than that achieved by the RT and FFT, which indicated that the RT and FFT slightly outperformed the SF at the highest values of nominal waviness. The results implied that the fibre tow orientations given by the SF were less accurate when dealing with complex fibre arrangements. The optimum values of calibrated parameters were used to predict the residual strains in each specimen using each of the three algorithms and the predictions compared to the measured distributions of residual strain using the Euclidean distance between their feature vectors. The performance of the three algorithms was evaluated by identifying which yielded the minimum Euclidean distance for each specimen when using the optimised parameters. The frequency with which each algorithm yielded the minimum Euclidean distance for a specimen is shown in Figure 30. At the scale of the specimens, it was found that for ten specimens the best predictions came from models based on orientation data determined using the RT algorithm, for six specimens the FFT algorithm provided the best orientation data, and only two using the SF algorithm, as shown in Figure 30. This means the RT algorithm has overall the highest success rate in predicting residual strains. Therefore, based on this data it is possible to non-subjectively rank the effectiveness

of the three different techniques for obtaining fibre orientation, with the RT as the best option to characterise fibre orientation. Similar findings were reported in [31], [35] and [36], which were based on the observations that more distinct peaks can be seen, or smaller changes in fibre alignment can be characterised, using the RT than the FFT. However, in this chapter, we draw this conclusion based on comparing the predictions for residual strains using the RT, FFT and SF, and by comparing the predictions with measurement data.

5.5.2. Validation of the models

Leave-one-out cross validation is a classical model-selection method in the machine learning field, used mainly for selecting the optimal values of calibrated parameters [99]. Its purpose is to assess the reliability of model predictions by determining the model that provides the best fit with the data [100]. In this context, 'best fit' refers to the prediction with the minimum Euclidean distance between the measurement and predictions, achieved by feeding the base finite element model with various values of the two parameters to be calibrated. The use of cross-validation helps to address the potential issue of overfitting, where a model may learn too much information from the calibration sets and subsequently struggle to predict accurately during the validation process. In other words, a model can fit the calibration sets well, but its predictions for future specimens may be poor. By employing leave-one-out cross-validation, each data point is used for both calibration and validation, ensuring a robust assessment of the model's predictive performance and enhancing its generalization capabilities. In order to achieve identically distributed data sets, all the data were stratified into three classes based on their nominal waviness before partitioning them into five calibration sets and one validation set. Thus, the otherwise sampling imbalance that may result in an over-fitting issue were eliminated. For instance, considering an extreme case, if stratification had not been applied, the five calibration sets could have had data of six specimens with 17.5%, six specimens with 20%, and three specimens with 25% nominal waviness, leaving the validation set having data from three specimens all with 25% nominal waviness. This would have led to the calibrated models providing more reliable predictions for specimens with 17.5% and 20% nominal waviness but less reliable for specimens with 25% nominal waviness. Therefore, the SLOOCV provided reliable and unbiased estimates of model performance. One drawback of SLOOCV is that for a large data set it can be a computationally expensive procedure to perform. This thesis used data from only 18 specimens and thus the

heavy computational cost was not a concern. If there were more specimens, a related technique called stratified k-folds cross validation could be used instead to reduce the computational burden [99].

The accuracy of the predicted residual strains was influenced by the level of nominal waviness in the specimens. For specimens with the highest nominal waviness, there was a possibility that the models could underestimate the magnitude of residual strains, as observed in one particular specimen where all three models provided unacceptable predictions during the validation process, as depicted in Figure 28. In this case, the magnitudes of strain are lower than the experimental data; however, the distribution in the higher strain areas can still be predicted quite well by the models based on the three algorithms. The validation diagram, shown in Figure 28(e), shows a single point fell outside of the acceptance region for each of the three algorithms. These points corresponded to the first Chebyshev polynomial, which represented the mean value of the residual strain maps. These outliers fall in the bottom right region of the validation diagram, showing that the mean value of the experimental data is larger than that of the predicted data, leading to an underestimation of the predicted residual strains. One possible cause of the underestimation by the models may be because the calibrated value of the coefficient of thermal expansion used for the 4^{th} validation set was the lowest compared to the other sets. As the residual strains were predicted by simulating a cooling process, a lower coefficient of thermal expansion would result in less contraction of the specimen, and thus lower predicted residual strains. Another possible explanation is that as nominal waviness increased from 17.5% to 25%, the accuracy of residual strain predictions declined. In other words, higher fibre waviness indicated more severe defects, making it more challenging for the algorithms to accurately determine the fibre orientation. As this orientation data is input into the models, this leads to lower accuracy predictions. Apart from the one specimen with models that generated unacceptable predictions, for the other 17 specimens, the magnitude and location of the residual strains were well predicted by their models based on the three fibre characterisation algorithms.

In this chapter, not only were three different severities of in-plane fibre waviness successfully characterised, but also the orientation data was incorporated into models to predict residual strains. The method of utilising non-destructive data to generate a model for

predicting residual strains is not limited to the ultrasound technique, it could also be applied using data obtained from other techniques, such as Eddy-current testing or X-ray computed tomography. These models could be further developed to not only predict residual strains, but also for predicting the failure of defective composite components under load, as will be discussed in Chapter 6. Furthermore, as discussed in [7], residual strains could be incorporated into these models to help predict the ultimate failure of composite components. In this chapter, only the surface strains were measured and predicted, but it shows a clear route of utilising ultrasound data to generate effective 2D models. In the future, the technique developed in this chapter could be extended to 3D models, which would be more challenging as the characterisation of the inner plies of laminates is not easy.

5.6. Summary

A technique of utilising ultrasound data to generate finite element models has been developed. These models were used for predicting residual strains in defective CFRP specimens with fibre waviness. The quality of the models was assessed by comparing feature vectors describing predicted and measured residual strain maps. The technique is shown to be robust for calibrating models and evaluating their performance. Therefore, it could be used to identify the most effective way of creating models based on non-destructive test data.

Algorithms based on the Radon transform, fast Fourier transform, and Sobel filters were shown to be capable of processing ultrasound images to generate effective models for predicting residual strains for defective specimens. Previous studies had made qualitative comparisons between these techniques. For this thesis, quantitative comparisons of the three algorithms based on image decomposition using Chebyshev polynomials were made at the fibre and the specimen scale. Based on these comparisons, the Radon transform algorithm was shown to outperform the other two.

The models were calibrated using an innovative stratified leave-one-out-cross-validation procedure which was shown to be effective in identifying the optimum value of the coefficient of thermal expansion of the material and the appropriate facet size for use in the algorithms for characterising fibre orientations. These models could be further developed to not only predict residual strains, but also for predicting the failure of defective composite components under load, which will be discussed in Chapter 6. The second objective about

developing a method for better utilising non-destructive evaluation data for characterising defects in composites thus has been achieved.

6. Failure analysis for defective specimen with in-plane fibre waviness under four-point bending test

6.1. Introduction

As identified in the knowledge gaps in Chapter 2, the failure behaviour of CFRP specimens with in-plane fibre waviness has not been fully understood. The mechanisms leading to the onset and propagation of damage prior to the first ply failure is still unclear. It has been found that little research has been conducted on the creation of finite element models to predict the failure behaviour of defective specimens with in-plane fibre waviness. Although models adopting Hashin-Rotem criterion [68] have proved to be successful in predicting buckling behaviour of specimens with artificially induced impact damage when subjected to a bending load, it is unclear whether it can be used for specimens containing fibre waviness [93].

This chapter investigates the failure behaviour of four sets of specimens containing four levels of fibre waviness: 0%, 20%, 25% and 30%. With each set having 6 specimens making 24 specimens in total. The specimens were tested in a four-point test rig until they were loaded to the first ply failure. Two DIC systems were used to record the images on both the top and bottom surface of the specimens during the bending tests. The strains and failure images obtained from DIC showed that there were two types of failures depending on the level of fibre waviness. One was delamination dominated failure. The other was micro buckling initiation, followed by crack propagation through the specimens causing fibre damage, matrix damage, and local delamination. The threshold level of fibre waviness for dividing the failure types was between 20% and 25%. For the first time the micro-buckling of fibres due to the in-plane fibre waviness was captured by the DIC cameras, and the growth of the cracks were also tracked. Hashin-Rotem criterion [68] and cohesive layer modelling were adopted in the finite element analysis for predicting the failure behaviour. It was shown that the finite element models were successful in predicting all the failure behaviour including delamination, fibre damage and matrix damage. The predicted failure progression agrees well with the measured data.

6.2. Experimental methods

6.2.1. Specimen preparation

Cross-ply carbon fibre reinforced laminates, with the same stacking sequence and material as the specimens in Section 4.2.1, were manufactured. Four different severities of in-plane fibre waviness were induced, with six specimens having each level of severity giving twenty-four specimens in total. The four level of severities were: 0%, 20%, 25%, 30%. The formers for creating the fibre waviness of 20%, 25% and 30% had central arc radii of 14.6 mm, 11.0 mm and 8.52 mm respectively. The specimens having 0% fibre waviness were created on a flat surface.

The curing and cooling procedures for manufacturing these specimens were also the same as introduced in Section 4.2.1. Each specimen in this chapter was cut to a size of 220 mm by 40 mm. The average thickness of the specimens was 3.56 mm. A typical defective specimen had in-plane fibre waviness in the top ply and the bottom ply contained no waviness. The x-direction was defined as parallel to the 0° fibres.

6.2.2. Ultrasonic Characterisation

Each specimen was tested using pulse-echo ultrasonic C-scans in order to characterise the fibre waviness in the specimens. A focused 10 MHz probe attached to a flaw detector (Epoch 4+, Olympus, Japan), was used to record the variation in amplitudes of the reflections received from the specimens. Each specimen was immersed in a water tank with the wavy side faced up, and the probe was placed vertically above the specimen with no tilt angle. The probe crystal diameter was 10 mm and the focal length was 50 mm. The probe was moved along a raster pattern by the multi-axis scanner (Midas-NDT, UK), as shown in Figure 5. The system was set to record the instantaneous amplitude from a 0.1 mm thick portion of the specimen at a depth of 0.45 mm, which is approximately equal to the depth of the first ply interface. This resulted in images showing the tows in the defective ply of the specimen. The amplitude was recorded at 0.1 mm increments along lines with a spacing of 0.2 mm. The images had a lateral spatial resolution of 10 pixels/mm.

6.2.3. Digital Image Analysis

DIC was used to measure strain on the top and bottom surface of all the specimens. The central regions on both the top and bottom surface of the specimen were selected as the

region of interest, each having a size of 60 by 40 mm. Speckle patterns were sprayed on these regions of interest. The DIC analysis was performed in a different lab from which has been describe in Chapter 5. The specimens were first sprayed white (Spray Paint, Puff Dino, Taiwan). Black speckles were then created on top using the VIC Speckle Pattern Application Kit (Correlated Solutions, USA). The nominal diameter of black speckles was 0.33 mm. The specimens were loaded to failure using a four-point bending test rig (HT-2402, Hung Ta Instrument, Taiwan), as shown in Figure 31. The load span was set to be 80 mm, while the support span was set to be 160 mm. The load cell was moved downwards at a constant speed of 0.8 mm/min. Force and displacement data were recorded every second during the loading process. The test for each specimen was stopped manually when the first ply failure occurred, which was signalled by a loud bang. The DIC system (Correlated Solutions, USA) for measuring strain on the top surface consisted of two cameras (Correlated Solutions, USA) forming an angle of 79°, while the DIC for measuring strain on the bottom surface consisted of two cameras forming an angle of 38°. The camera speed was set at 20 fps for all cameras. One light emitting diode lamp (Sunray 200, Skier, Taiwan) was used to provide illumination for the top surface, and one (Correlated Solutions, USA) for illuminating the bottom surface. The images were processed by the VIC-3D 9.0 software (Correlated Solutions, USA) using a facet size of 65 pixels and grid spacing of 11 pixels. The values of facet size and grid spacing were determined after several trials to avoid broken strain maps.

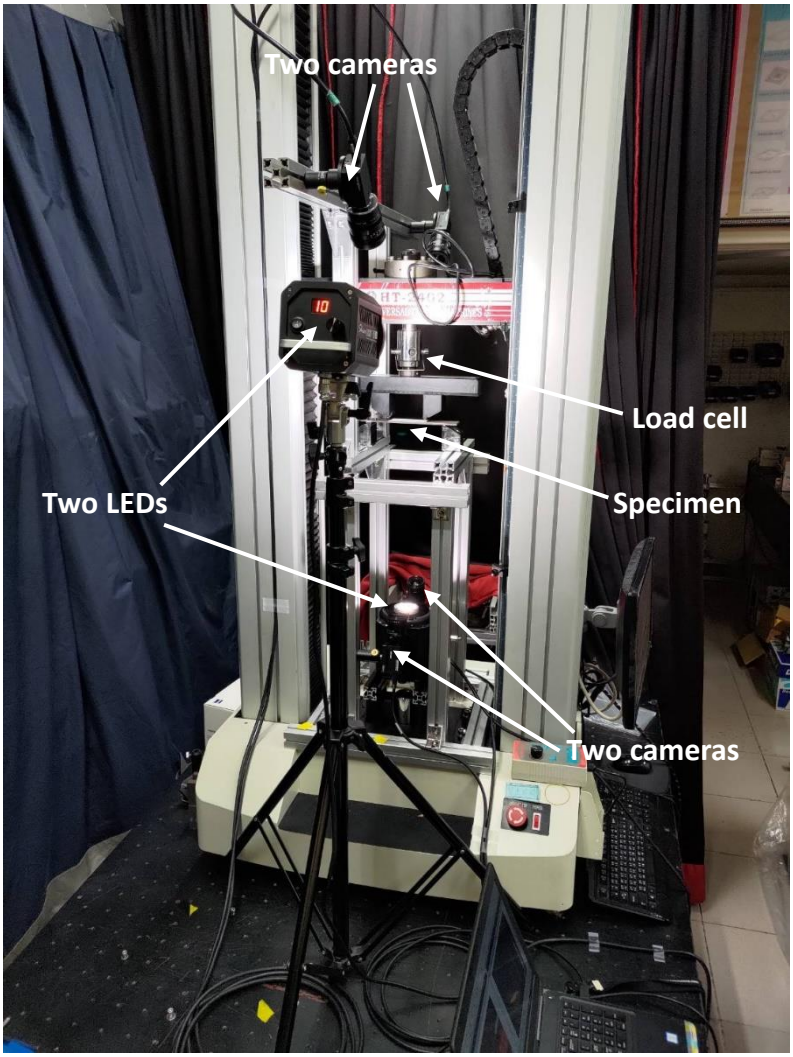

Figure 31: Four-point bending test rigs with a DIC system taking measurements from both the top and bottom surface of the specimens while being tested.

6.3. Finite element analysis

6.3.1. Simulation of the test

Abaqus 6.14 (Dassault Systèmes, France) was used to simulate the four-point bending test and to predict the failure progression. The model was created using four cylinders and a composite laminate, as shown in Figure 32. The load and support cylinders were treated as discrete rigid bodies. Surface to surface contact was simulated between each cylinder and the specimen, and the friction coefficient was set to 0.3. The boundary conditions for the two load cylinders were $U_X = U_Y = U_{RX} = U_{RY} = U_{RZ} = 0$, $U_Z = -20$ mm. The boundary conditions for the two support cylinders were $U_X = U_Y = U_Z = U_{RX} = U_{RY} = U_{RZ} = 0$. Since the four-point bending test was considered as a quasi-static process, so Abaqus/Standard was used, with the non-linear geometry option toggled on. Arbitrary

Lagrangian-Eulerian (ALE) analysis was used to prevent large distortions of elements at the central region.

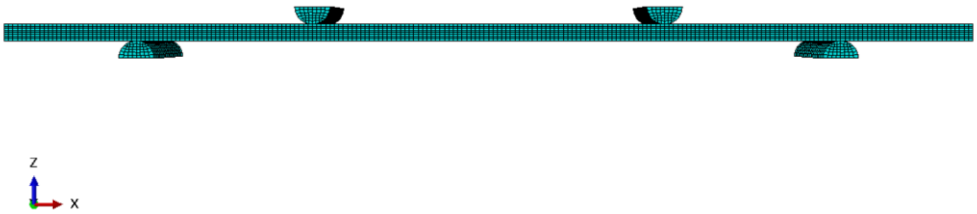

Figure 32: Finite element model for simulating the four-point bending test.

The CFRP laminates were created as shown in Figure 32. Each specimen was discretised into 8 layers, and each layer was discretised into 35,200 elements, with each element having a uniform size of 0.5 mm. Therefore, each specimen was simulated using 281,600 C3D8R elements. These elements were initially given the transversely isotropic material properties shown in Table 3 [101]. Tensile tests were performed on unidirectional laminates that were made of the same materials, and thus E_{11} in Table 3 was replaced by an expreimentally obtained value: 130.30 GPa, and E_{22}, E_{33} were replaced by 16.8 GPa. Other than the three Young's modulus properties, the other property inputs in the Abaqus model were all from Table 3. It was found that E_{11} was the dominant property that affect the simulation results, and the other properties were less effective, thus it is acceptable to use the other properties in Table 3. A better simulation would be achieved when all the property inputs were experimentally obtained instead of using values from literatures.

Table 3: Mechanical parameters of the lamina [101].

Parameters	Units	Values
Longitudinal tensile modulus, E_{11}	GPa	156.00
Transverse tensile modulue, E_{22}, E_{33}	GPa	8.35
In-plane shear modulus, G_{12}	GPa	4.20
Out-of-plane shear modulus, G_{13}	GPa	4.20
Out-of-plane shear modulus, G_{23}	GPa	2.52
Major Poisson's ratio, ν_{12}	-	0.33
Through thickness Poisson's ratio, ν_{13}	-	0.33
Through thickness Poisson's ratio, ν_{23}	-	0.55
Longitudinal tensile strength, X_T	MPa	2500.00
Longitudinal compressive strength, X_C	MPa	1400.00
Transverse tensile strength, Y_T	MPa	75.00
Transverse compressive strength, Y_C	MPa	250.00
In-plane shear strength, S_{12}	MPa	95.00
In-plane shear strength, S_{13}	MPa	95.00
Out-of-plane shear strength, S_{23}	MPa	108.00
Fibre tensile fracture energy, G_{ft}	J/m^2	91.60
Fibre compressive fracture energy, G_{fc}	J/m^2	79.90
Matrix tensile fracture energy, G_{mt}	J/m^2	0.22
Matrix compressive fracture energy, G_{mc}	J/m^2	2.00

To predict the progressive failure behaviour of the laminates, a specially written UMAT was used. A UMAT is a user subroutine for defining a material's mechanical behaviour. The UMAT defined the initiation of the intra-lamina failure using Hashin-Rotem criterion [68] and the progressive failure behaviour by iterating the material Jacobian matrix, $\frac{\partial \Delta\sigma}{\partial \Delta\varepsilon}$. Four failure modes were considered in Hashin-Rotem criterion [68]: fibre rupture in tension; fibre buckling and kinking in compression; matrix cracking under transverse tension and shearing; matrix

crushing under compression and shearing. The Hashin-Rotem failure criterion [68] in Abaqus was governed by the following equations [102]:

Fibre tension($\hat{\sigma}_{11} \geq 0$):

$$F_f^t = (\frac{\hat{\sigma}_{11}}{X^T})^2 + \alpha(\frac{\hat{\tau}_{12}}{S^L})^2 \tag{27}$$

Fibre compression($\hat{\sigma}_{11} \leq 0$):

$$F_f^c = (\frac{\hat{\sigma}_{11}}{X^C})^2 \tag{28}$$

Matrix tension($\hat{\sigma}_{22} \geq 0$):

$$F_m^t = (\frac{\hat{\sigma}_{22}}{Y^T})^2 + (\frac{\hat{\tau}_{12}}{S^L})^2 \tag{29}$$

Matrix compression($\hat{\sigma}_{22} \leq 0$):

$$F_m^c = (\frac{\hat{\sigma}_{22}}{2S^T})^2 + \left[(\frac{Y^C}{2S^T})^2 - 1\right]\frac{\hat{\sigma}_{22}}{Y^C} + (\frac{\hat{\tau}_{12}}{S^L})^2 \tag{30}$$

In the above equation, X^T denotes the longitudinal tensile strength, X^C denotes the longitudinal compressive strength, Y^T denotes the transverse tensile strength, Y^C denotes the transverse compressive strength. α is a coefficient that determines the contribution of the shear stress to the fibre tensile initiation criterion, α equalled 1 in this thesis since in-plane shear stress is considered influential; $\hat{\sigma}_{11}$, $\hat{\sigma}_{22}$, $\hat{\tau}_{12}$ are components of the effective stress tensor, $\hat{\sigma}$ is used to evaluate the initiation criteria and is computed from:

$$\hat{\sigma} = M\sigma \tag{31}$$

where σ is the true stress and M is the damage operator:

$$M = \begin{bmatrix} \frac{1}{(1-d_f)} & 0 & 0 \\ 0 & \frac{1}{(1-d_m)} & 0 \\ 0 & 0 & \frac{1}{(1-d_s)} \end{bmatrix} \tag{32}$$

d_f, d_m, and d_s are internal damage variables that describe fibre, matrix and shear damage. They are derived from damage variables d_f^t, d_f^c, d_m^t, and d_m^c, which are given by the following equations:

$$d_f = \begin{cases} d_f^t & if \ \ \hat{\sigma}_{11} \geq 0, \\ d_f^c & if \ \ \hat{\sigma}_{11} \leq 0, \end{cases}$$

$$d_m = \begin{cases} d_m^t & if \ \ \hat{\sigma}_{22} \geq 0, \\ d_m^c & if \ \ \hat{\sigma}_{22} \leq 0, \end{cases} \tag{33}$$

$$d_s = 1 - (1 - d_f^t)(1 - d_f^c)(1 - d_m^t)(1 - d_m^c)$$

Prior to damage initiation, M is equal to the identity matrix, so $\hat{\sigma} = \sigma$. When one of the failure modes occurs, i.e., either one of the four variables: F_f^t, F_f^c, F_m^t, F_m^c is greater than 1, the corresponding damage variable: d_f, d_m, d_s is greater than 0, indicating the corresponding failure.

Once a damage initiates, the material stiffness cannot remain unchanged. The damage evolves with the degradation of the material stiffness. The response of a material is thus governed by:

$$\sigma = C_d \varepsilon^{el} \tag{34}$$

where ε^{el} is the elastic strain and C_d is the damaged stiffness matrix, which is expressed as:

$$C_d = \frac{1}{D}\begin{bmatrix} (1 - d_f)E_1 & (1 - d_f)(1 - d_m)\nu_{21}E_1 & 0 \\ (1 - d_f)(1 - d_m)\nu_{12}E_2 & (1 - d_m)E_2 & 0 \\ 0 & 0 & (1 - d_s)GD \end{bmatrix} \tag{35}$$

where $D = 1 - (1 - d_f)(1 - d_m)\nu_{12}\nu_{21}$, d_f denotes the current state of fibre damage, d_m denotes the current state of matrix damage, d_s denotes the current state of shear damage, E_1 is the Young's modulus in the fibre direction, E_2 is the Young's modulus in the matrix direction, G is the shear modulus, and ν_{12} and ν_{21} are Poisson's ratios.

The damaged stiffness matrix C_d evolves with the change in the damage variables, d_f, d_m, and d_s. After damage initiation, the damage variable for a particular mode is governed by the following equation:

$$d = \frac{\delta_{eq}^{f}(\delta_{eq} - \delta_{eq}^{0})}{\delta_{eq}(\delta_{eq}^{f} - \delta_{eq}^{0})} \tag{36}$$

where δ_{eq}^{0} is the initial equivalent displacement at which the initiation criterion for that mode was met, in other words, when one of the four corresponding variables: F_f^t, F_f^c, F_m^t, F_m^c equals to 1, and δ_{eq}^{f} is the displacement at which the material is completely damaged in this failure mode. The relationship between equivalent stress and equivalent displacement is shown in Figure 33. The equations of equivalent stress and equivalent displacement for the four failure modes are different, and they were expressed as follows:

Fibre tension($\hat{\sigma}_{11} \geq 0$):

$$\begin{aligned} \delta_{eq}^{ft} &= L^c \sqrt{\langle \varepsilon_{11} \rangle^2 + \alpha \varepsilon_{12}^2} \\ \sigma_{eq}^{ft} &= \frac{\langle \sigma_{11} \rangle \langle \varepsilon_{11} \rangle + \alpha \tau_{12} \varepsilon_{12}}{\delta_{eq}^{ft} / L^c} \end{aligned} \tag{37}$$

Fibre compression($\hat{\sigma}_{11} \leq 0$):

$$\begin{aligned} \delta_{eq}^{fc} &= \delta_{eq}^{ft} \langle -\varepsilon_{11} \rangle \\ \sigma_{eq}^{fc} &= \frac{\langle -\sigma_{11} \rangle \langle -\varepsilon_{11} \rangle}{\delta_{eq}^{ft} / L^c} \end{aligned} \tag{38}$$

Matrix tension($\hat{\sigma}_{22} \geq 0$):

$$\begin{aligned} \delta_{eq}^{mt} &= L^c \sqrt{\langle \varepsilon_{22} \rangle^2 + \varepsilon_{12}^2} \\ \sigma_{eq}^{mt} &= \frac{\langle \sigma_{22} \rangle \langle \varepsilon_{22} \rangle + \tau_{12} \varepsilon_{12}}{\delta_{eq}^{mt} / L^c} \end{aligned} \tag{39}$$

Matrix compression($\hat{\sigma}_{22} \leq 0$):

$$\delta_{eq}^{mc} = L^c \sqrt{\langle -\varepsilon_{22} \rangle^2 + \varepsilon_{12}^2} \tag{40}$$

$$\sigma_{eq}^{mc} = \frac{\langle -\sigma_{22} \rangle \langle -\varepsilon_{22} \rangle + \tau_{12}\varepsilon_{12}}{\delta_{eq}^{mc}/L^c}$$

In the above equations, L^c, is based on the element geometry and formulation: it is typically the length of a line across an element for a first-order element or half of the same length for a second-order element. The symbol $\langle\ \rangle$ in the equations above represents the Macaulay bracket operator, which is defined for every $\alpha \in R$ as $\langle \alpha \rangle = (\alpha + |\alpha|)/2$. The strain components were calculated in Abaqus and passed to the UMAT for use in the calculation of equivalent stress and equivalent displacement, and to evaluate the failure initiation.

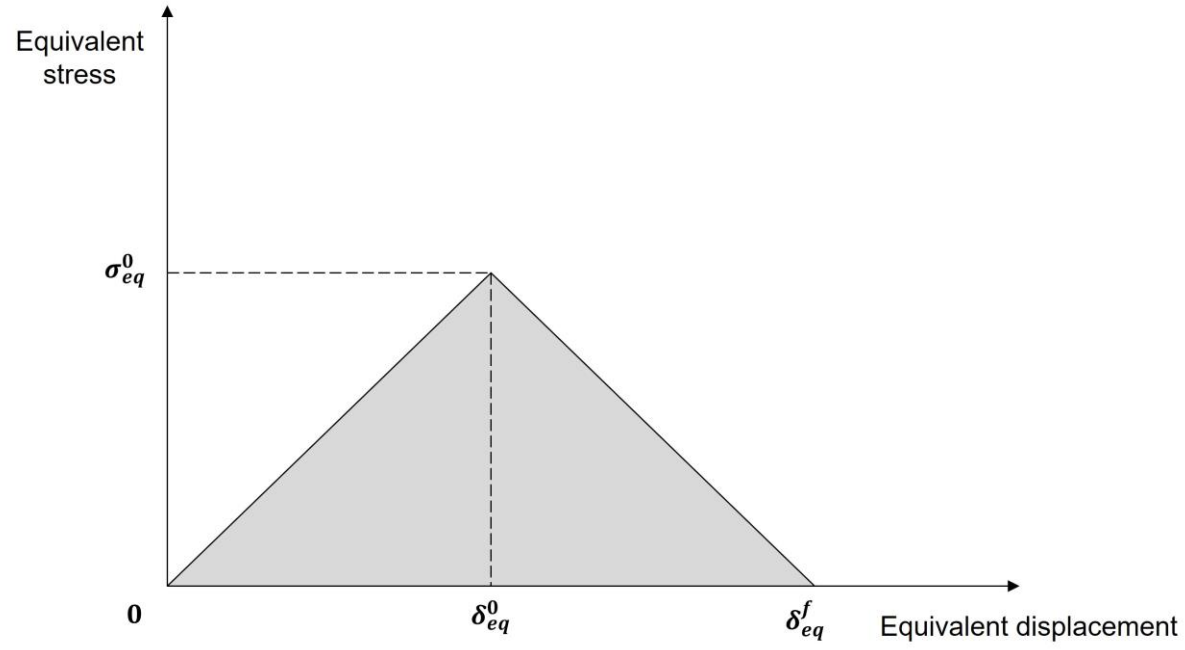

Figure 33: Equivalent stress versus equivalent displacement. The shaded area exhibits the fracture energy.

The four damage variables F_f^t, F_f^c, F_m^t, F_m^c initially have a value of 0 and then monotonically evolve from 0 to 1. With the accumulation of an applied displacement load, one type of damage at a node point may take place when one of the four variables reached 1, which is governed by Equation (27), (28), (29), and (30) respectively. The evolution of the damage is governed by the dissipation of the fracture energy in that failure mode, which corresponded to the triangular area in Figure 33.

6.3.2. Simulation of the defect

Fibre waviness was firstly characterised by the pulse-echo ultrasonic C-scans. The resultant images were analysed by the Radon transformation algorithm using a facet size of

45 pixels to obtain the fibre orientations which were transferred into finite element models. The algorithm and optimal parameter have been identified in Chapter 5. One exemplar fibre orientation map is shown in Figure 34. The defect was simulated by creating a discrete field at the centre of the top 0° ply, and the number of elements of this discrete field was the same as the number of data points in the orientation map. Then the measured local fibre orientation was assigned to each element in the discrete field.

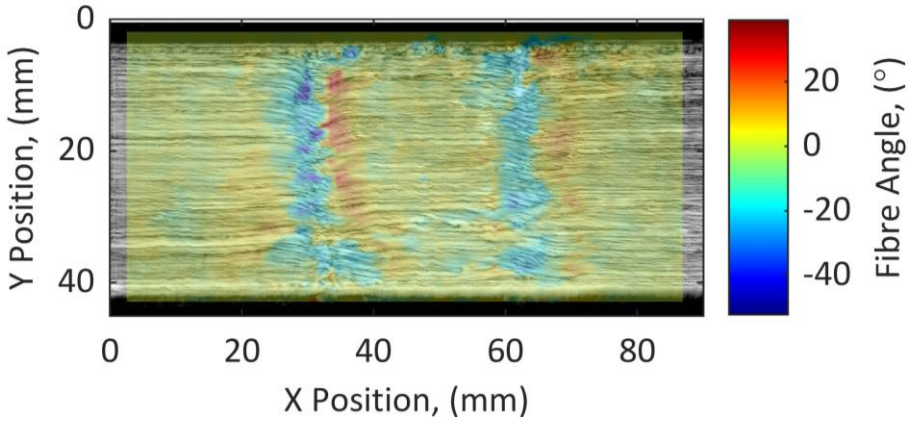

Figure 34: One exemplar fibre orientation map obtained from processing an Ultrasonic C-scan image using the Radon transformation for a specimen having 30% fibre waviness.

6.3.3. Simulation of the cohesive layers

To predict the inter-laminar failure in the laminates, a cohesive zone was used in the analysis. Cohesive behaviour is useful in modelling the bonded interfaces to predict both the initiation and propagation of the delamination in composites. In this analysis, a thin cohesive layer of COH3D8 elements was created between every two adjacent CFRP plies, and the thickness of the cohesive layer was set to 0.001 mm to represent the realistic delamination phenomenon. The constitutive response in the cohesive elements was governed by the cohesive law, which defines the traction and separation behaviour. Three failure modes can occur for the cohesive elements: normal mode, shear mode in the 1st direction and shear mode in the 2nd direction. The normal mode occurs with stress orthogonal to the local plane of the crack surface, shear mode in the 1st direction occurs with stress parallel to the crack surface but orthogonal to the crack front, and shear mode in the 2nd direction occurs with stress parallel to the crack surface and to the crack front. For the normal mode, the relationship between the normal stress and displacement is shown in Figure 35. It can be seen in Figure 35 that the penalty stiffness $K_n = \frac{N_{max}}{\delta_n^{init}}$, where N_{max} is the maximum normal stress

at the failure initiation displacement δ_n^{init}. The triangular area is the fracture energy, G_C. Thus, the displacement at the total failure point can be calculated as $\delta_n^{fail} = \frac{2G_C}{N_{max}}$. Similar triangles could be drawn for the shear mode in the first and second direction. Instead of using the maximum stress failure criterion, it has been proven more effective to use the quadratic failure criterion to predict the initiation of damage [103], and the criterion is expressed as:

$$\left(\frac{\langle\sigma_n\rangle}{N_{max}}\right)^2 + \left(\frac{\sigma_s}{S_{max}}\right)^2 + \left(\frac{\sigma_t}{T_{max}}\right)^2 = 1 \tag{41}$$

where σ_n is the nominal stress in pure normal mode, σ_s and σ_t are the nominal stresses in the first and second shear direction respectively, N_{max} is the maximum allowable stress in pure normal mode, S_{max} and T_{max} are the maximum allowable stresses in the shear mode in the first and second direction respectively.

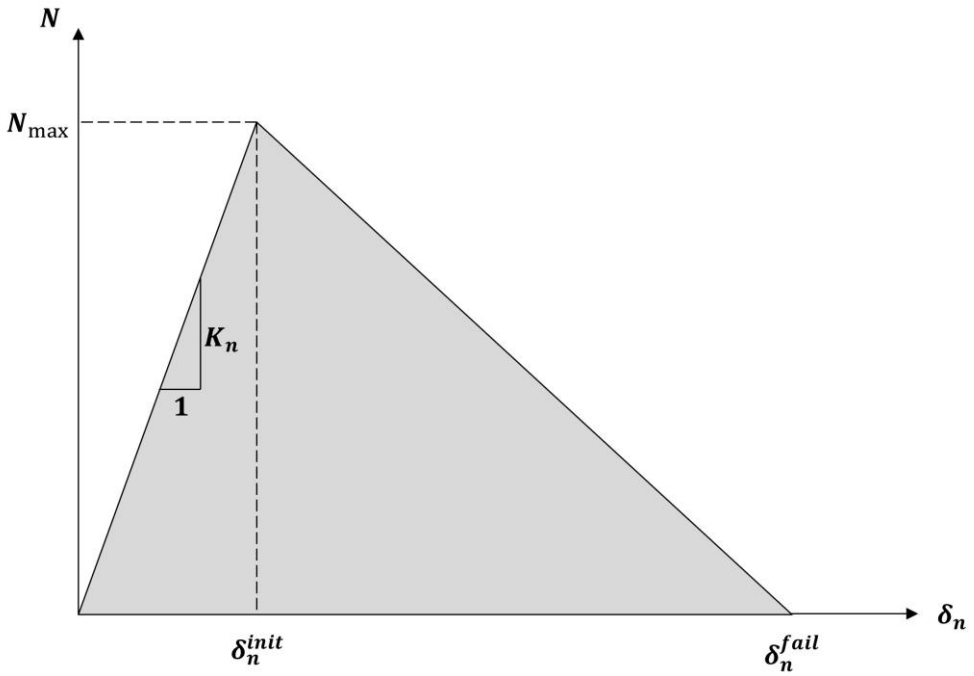

Figure 35: The normal stress versus displacement for the opening mode. The shaded area exhibits the fracture energy.

The constitutive behaviour is governed by the equations:

$$\sigma = \begin{cases} K\delta_m & \delta_m \le \delta_m^0 \\ (1-d)K\delta_m & \delta_m^0 < \delta_m < \delta_m^f \\ 0 & \delta_m \ge \delta_m^f \end{cases} \tag{42}$$

where d is a scalar damage variable, δ_m is the effective displacement for a mix mode, δ_m^0 is the effective displacement when a damage is initiated, and δ_m^f is the effective displacement at total failure. The effective displacement δ_m for the mixed mode is defined as [104]:

$$\delta_m = \sqrt{\langle \delta_1 \rangle^2 + {\delta_2}^2 + {\delta_3}^2} \tag{43}$$

where δ_1, δ_2 and δ_3 are the displacements in the three separate modes, as shown in Figure 36. The scalar damage variable d initially has a zero value. After damage has initiated, d monotonically increases from 0 to 1. The cohesive elements are fully damage when d equals 1.

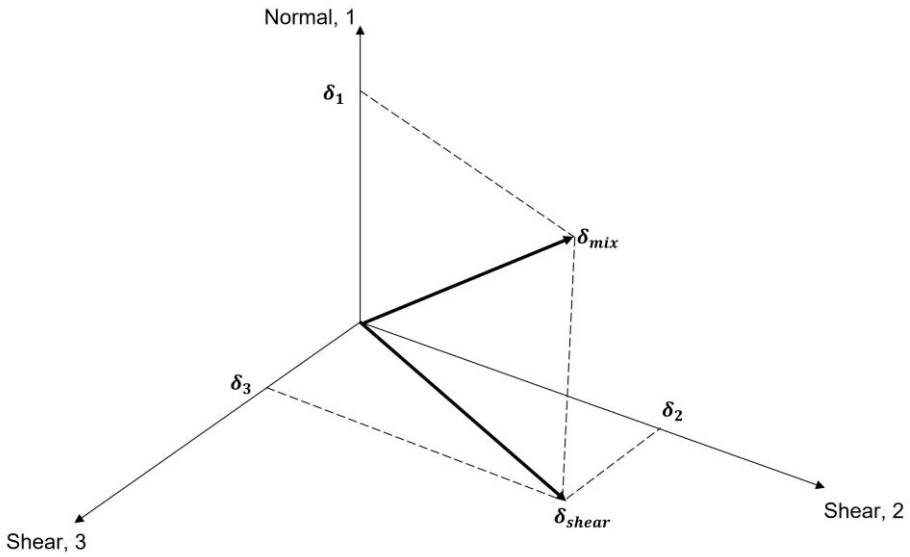

Figure 36: Effective displacement in the mixed mode.

The evolution of damage is controlled by the mixed-mode energy release rate, G_C, which according to the Benzeggagh-Kenane law [105], can be expressed as:

$$G_{\mathrm{IC}} + (G_{\mathrm{IIC}} - G_{\mathrm{IC}}) \left(\frac{G_{shear}}{G_T} \right)^{\eta} = G_C \tag{44}$$

where $G_{shear} = G_{\mathrm{IIC}} + G_{\mathrm{IIIC}}$, $G_T = G_{\mathrm{IC}} + G_{shear}$, G_{IC}, G_{IIC}, and G_{IIIC} are the critical strain energy release rate for the normal mode, the shear mode in the first and the second directions respectively. The Benzeggagh-Kenane law was used because the mixed mode fracture toughness calculated from it covers a comprehensive range of mode mixity, which can provide more accurate results [106]. The parameters for defining the behaviours of

cohesive elements are shown in Table 4 [103]. At this initial stage of the simulation, it should be acceptable to use these parameters from literature. However, one would expect that better match between experiment and simulation would be achieved if all the parameters were obtained from experimental procedures or be optimised using model updating algorithms [107]. Parameters can be obtained from the double cantilever beam test for normal mode, the end notch flexure test for shear mode in the 1st direction, and the edge crack torsion test for shear mode in the 2nd direction.

Table 4: Cohesive elements parameters [103].

$G_{\mathrm{I}C}$ (N/mm)	$G_{\mathrm{II}C}$ (N/mm)	K (N/mm^3)	σ_n (MPa)	σ_s (MPa)	σ_t (MPa)	η
0.361	1.083	10^5	20	40	40	10^{-5}

6.4 Results

6.4.1 Bending test on specimens with fibre waviness

Twenty-four CFRP laminates with four levels of in-plane fibre waviness were loaded to the first-ply failure using four-point bending tests. The ability of the laminates to carry a load varied with the waviness severity. It is shown in Figure 37 that specimens with 0% fibre waviness had the highest average ultimate bending moment, which is 48.7 Nm. The average ultimate bending moment drops with the increase of fibre waviness severity. For specimens with 30% fibre waviness, the average ultimate bending moment declines by 32% to 32.9 Nm. The error bars in Figure 37 indicate standard errors, which also decrease with the increase of waviness severity.

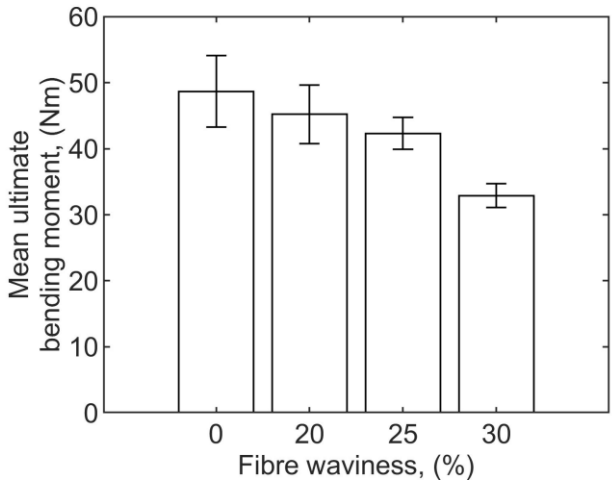

Figure 37: Comparison of mean ultimate bending moment for specimens having each level of fibre waviness.

The four-point bending tests were in displacement control, but load values were also recorded at each displacement which can reveal the load carrying abilities of the specimens. The loading scenarios were the same for the whole set of specimens. However, the force and displacement response of the specimens with different waviness varied. The force versus displacement curves can be categorised by the two types of failure behaviour. One type is for specimens with 0% and 20% fibre waviness, where force linearly increased with the increase in displacement, but after reaching a critical load the force decreased sharply. The curve shape is smooth with no discontinuities or steps. One example of this type of curve is shown in Figure 38 (left). The sharp decrease in force from the maximum indicates delamination occurring and rapidly propagating. The other type of failure behaviour is for specimens with 25% and 30% fibre waviness. For this type of failure, the force also increased linearly with the increase of displacement. However, before the force reached a critical value there was a small drop in force indicating the initiation of damage, as shown at (b) in Figure 38 (right). After the force reached the peak value, at (c) in Figure 38 (right), force reduced in steps with very small increases between successive reductions, giving a jagged curve to (d) in Figure 38 (right), as the damage propagates. The damage is identified as micro-buckling of fibres by DIC analysis, which will be discussed later. Position (d) in both Figure 38 (left) and (right) is the point when the specimens completely failed. At the elastic region, when the same displacement is applied to defective and defect-free specimens, their force responses differ. As shown in Figure 38, at an applied displacement of 6 mm, the force was approximately 1200 N for the specimen with 0% waviness, while it was approximately 1500 N for the specimen with 30% waviness.

This discrepancy could be attributed to a high amount of fibre waviness defects, which resulted in significant twisting of fibres in the top ply. Consequently, the twisted fibres acted like springs, reinforcing the top ply and enabling it to resist compressive forces during elastic loadings. However, further investigation is necessary to confirm this assumption conclusively.

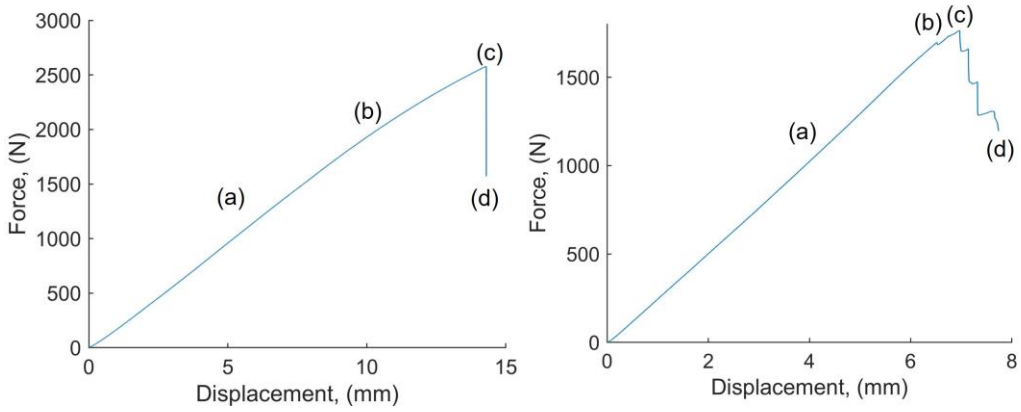

Figure 38: Force versus displacement curves for one specimen with 0% fibre waviness (left) and one specimen with 30% fibre waviness (right) during the four-point bending tests under displacement control. The data was obtained experimentally.

6.4.2 Delamination and micro-buckling analysis using DIC

DIC was used to take measurements from both the top and bottom surface of the specimens during the four-point bending tests. The camera speed was set to 20 fps, therefore the time interval between two consecutive DIC steps was 0.05 s. It was found that for specimens with 0% and 20% fibre waviness, the changes in strains during the four-point bending tests were similar. Taking the specimen being tested in Figure 38 (left) as an example, both tensile and compressive strains in the x-direction were obtained at the four loading stages (a) to (d). Changes in compressive strains in the x-direction are shown in Figure 39. The specimen experienced a slow increase in compressive strains first, then at a certain instant there appeared a sharp and sudden decline. The same phenomenon is seen in the tensile strains in the x-direction on the bottom surface, as shown in Figure 40. However, the decreasing magnitudes in the tensile strains are far less than those in the compressive strains. A decrease of 89% in compressive strains in the x-direction was observed during stage (c) to (d), compared with 29% in tensile strains. The load dropped by 39% for the exemplar 0% specimen from stage (c) to (d). It was also observed that, during the elastic region of the loadings, the magnitude of the compressive strains in the x-direction on the top surface and the tensile strains on the bottom surface are similar, with a maximum difference below 10%.

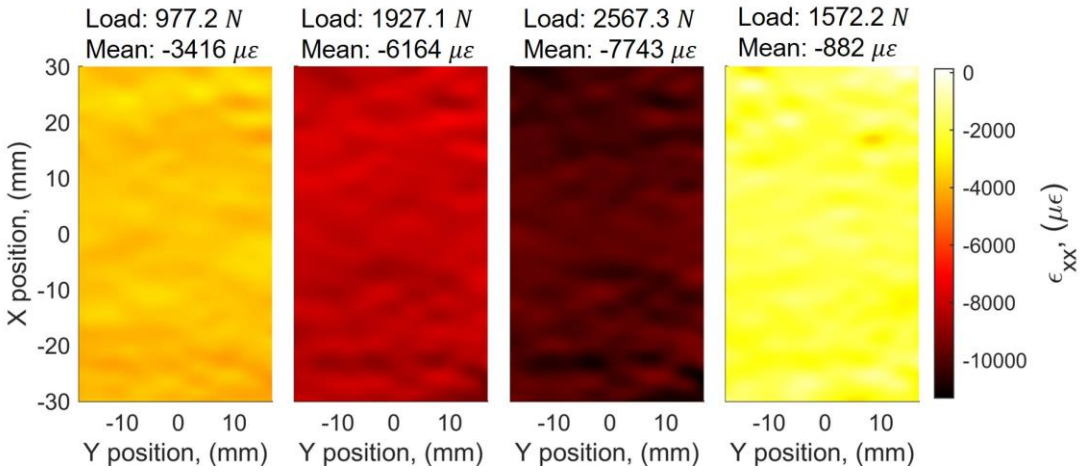

Figure 39: Compressive strains in the x-direction for the top surface of the specimen at four loading stages corresponding to (a) to (d) for the exemplar 0% specimen in Figure 38 (left).

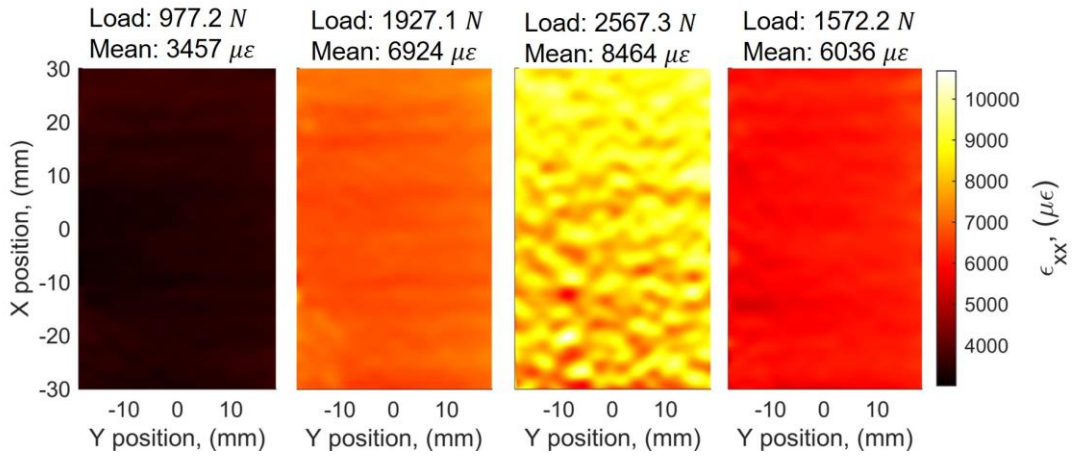

Figure 40: Tensile strains in the x-direction for the bottom surface of the specimen at four loading stages corresponding to (a) to (d) for the exemplar 0% specimen in Figure 38 (left).

For specimens having 25% and 30% fibre waviness, the change in strains is quite different compared with specimens having 0% and 20% waviness defects. Taking the specimens being tested in Figure 38 (right) as an example, both tensile and compressive strains in the x-direction were obtained at the four loading stages (a) to (d). The compressive strains in the x-direction at the four loading stages are shown in Figure 41, while the tensile strains are shown in Figure 42. It is observed that the strain distribution is less uniform than the results shown in Figure 39 and Figure 40. There are some localised high strain regions in both the compressive and tensile strain maps, which corresponded to the locations where the most severe localised fibre waviness existed. The second images from the left

corresponding to (b) in both Figure 41 and Figure 42 indicate the initiation of the micro-buckling of fibres. The third and the fourth images from the left corresponding to (c) and (d) in Figure 41 and Figure 42 show the propagation of the damage caused by micro-buckling of fibres. The fourth images in Figure 41 and Figure 42 also indicate that delamination occurred at the right side of the specimens, which accompanied a sudden decrease of the mean strain. However, the decreasing magnitudes in the tensile strains are far less than in the compressive strains. A decrease of 93% in compressive strains in the x-direction was observed during stage (c) to (d), compared with 2% in tensile strains. The load dropped by 32% for the exemplar 30% specimen from stage (c) to (d).

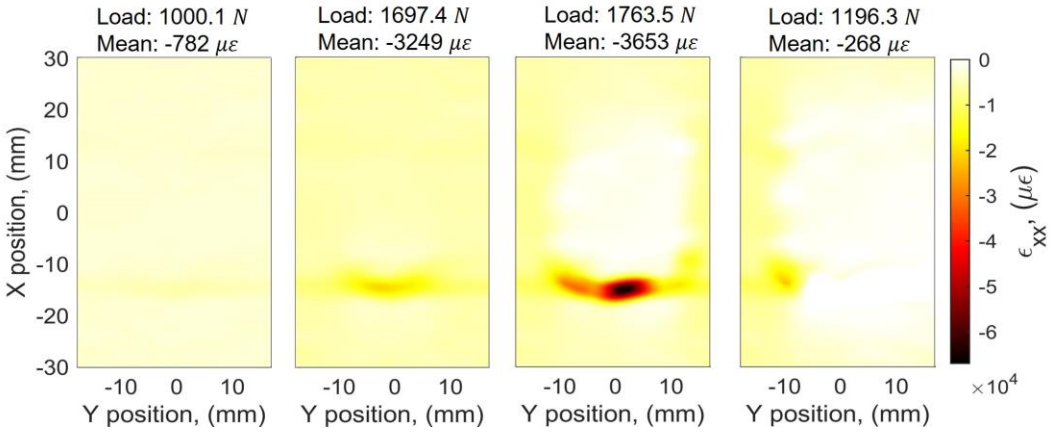

Figure 41: Compressive strains in the x-direction for the top surface of the specimen at four loading stages corresponding to (a) to (d) in Figure 38 (right) for the exemplar 30% specimen.

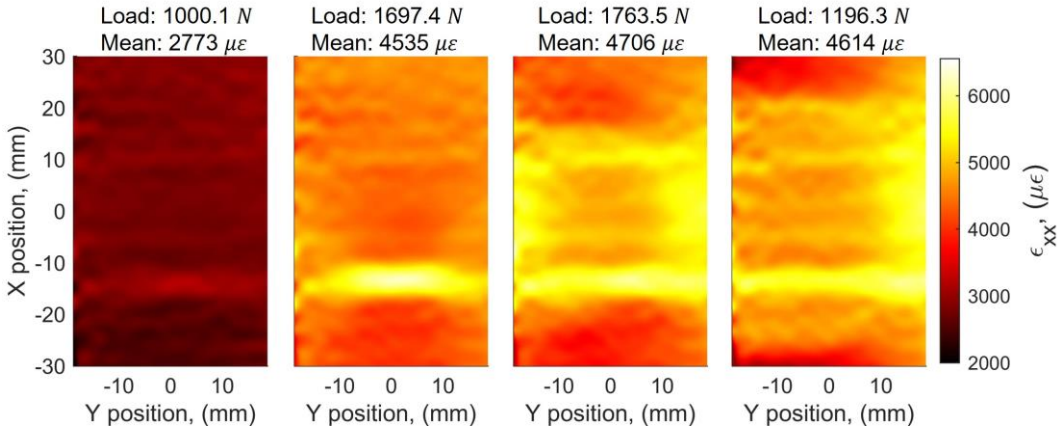

Figure 42: Tensile strains in the x-direction for the bottom surface of the specimen at four loading stages corresponding to (a) to (d) in Figure 38 (right) for the exemplar 30% specimen.

The DIC camera systems captured the damage morphology in real time. Taking one specimen with 30% fibre waviness as an example, the appearance of the first crack coincided

with first evidence of micro-buckling in the images from the DIC system, as shown in Figure 43. When the applied displacement increased from 7.1526 mm to 7.1540 mm within the time interval of 0.05 s, two tiny cracks appeared on the top surface of the specimen under compression, as indicated by the white ellipses in Figure 43. The corresponding out-of-plane displacement provides a side view of the surface morphology, which changes to have a small bump as shown in the enlarged image, indicating micro buckling occurred. The propagation of the damage on the top surface was also captured by the DIC cameras, as shown in Figure 44. The damage propagated transversely along the waviness band through the top surface in 0.7 s once the micro-buckling initiated. Both fibre failure and matrix failure are shown in the images taken by the DIC cameras. It is also visible in the strain map in Figure 44 when the load was 1746.6 N that the propagation of damage caused the left part of the top ply to delaminate, followed by the whole ply delaminating as shown in the strain map when the load was 1747.0 N. The failure progress is also shown in the raw images, where both the matrix and fibre failure are observed.

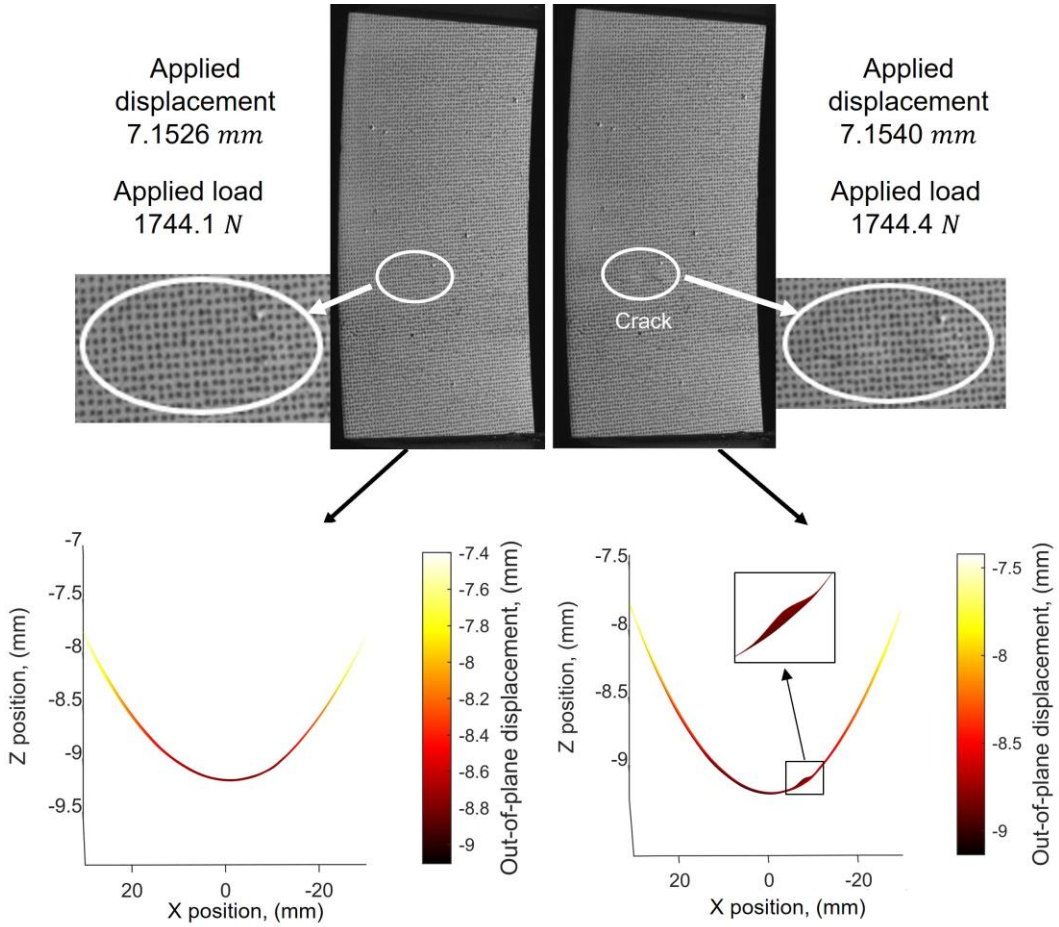

Figure 43: Real time images of initiation of micro-buckling on the top surface capture by DIC cameras, and the corresponding out-of-plane displacement showing the small bump indicating micro-buckling.

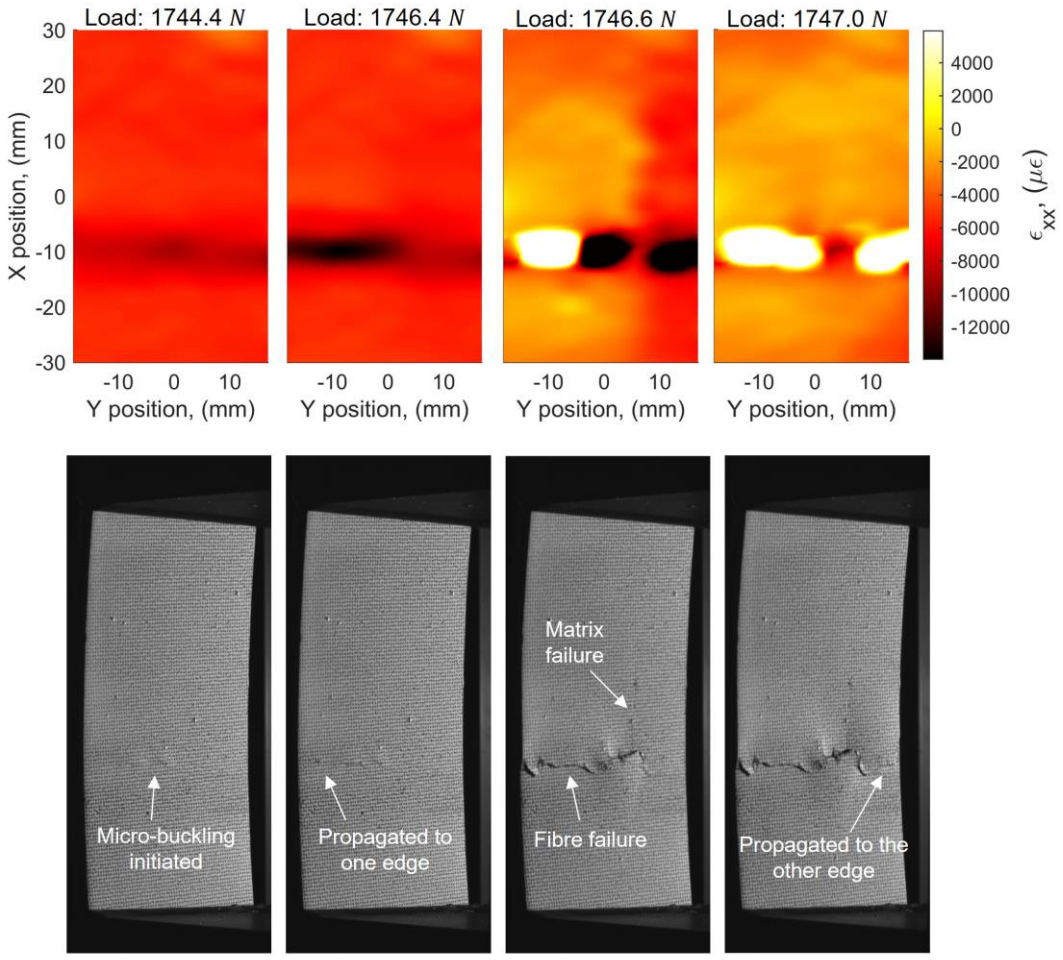

Figure 44: The compressive strains in the x-direction on the top surface showing the propagation of the damage after micro-buckling occurred, and the corresponding real-time images taken by the DIC cameras shows the failure progression.

6.4.3 Characterisation of the damage

The fractured surface was characterised in an optical microscope and SEM (scanning electron microscope). The results show the damage morphology in fine detail. The micrographs of damaged regions and the results from DIC and ultrasonic C-scan were used to reveal the failure events in a sequence, as shown in Figure 45. The data from ultrasonic C-scan was processed by the Radon transformation using a facet size of 45 pixels, and the resulting fibre orientation map is shown in Figure 45(a). The black dashed lines show paths of damage propagation. It is observed in Figure 45(a) there are positive and negative values of fibre orientations, which were defined with respect to the x-direction. The fibre orientation map was further processed by dividing it into a number of facets with a facet size of 45 pixels first, then calculating the standard deviation at each facet to reveal the variation of fibre orientations at each facet. which is shown as a map in Figure 45(b), with the maximum being

labelled as 19.5°. The initiation of micro-buckling was captured by DIC and the corresponding compressive strain in the x-direction for the top surface was calculated and shown in Figure 45(c). The micro buckling initiated at the location where the compressive strain was maximum. The optical micrograph was obtained using an optical microscope (Olympus, STM6, Japan). The specimen was prepared by removing the white paint with a 600 grit SiC abrasive paper to obtain a smooth surface, shown in Figure 45(d). The three locations shown in Figure 45(d) were inspected and the micrographs are shown in Figure 45(e) to (g). Figure 45(f) shows the micro buckling initiation site, from which damage propagated in three directions causing both fibre and matrix damage. Figure 45(e) and (g) show that matrix damage caused fibre damage and vice versa, which lead to jagged shapes along the damage propagation paths. The jagged propagation paths correlated with the jagged curve shown in Figure 38 (right).

The fracture surface of a specimen with 25% fibre waviness was inspected using a SEM (JEOL, JSM-7000F, Japan). The resultant images were shown in Figure 46. Figure 46(a) and (d) were obtained by inspecting a small area in the location shown in Figure 45(f) using the SEM. Figure 46(b) was obtained by inspecting a small area in the location shown in Figure 45(g), and Figure 46(c) was obtained by inspecting a small area in the location shown in Figure 45(e) using the SEM. It is shown in Figure 46(a) that micro buckling of fibres is a localised damage, which has an appearance like a bridge broken in half. This damage propagated to the nearby regions causing both fibre and matrix failure. The morphology of fibre breakage is shown in Figure 46(b). The damage normally did not propagate along a straight direction, but formed a jagged path, as shown in Figure 46(c). This jagged path corresponded to the jagged curve shown in Figure 38 (right). The morphology of a single fibre breakage is shown in Figure 46(d), where the neutral axis, compressive side and tensile side are labelled, showing evidence of compressive failure.

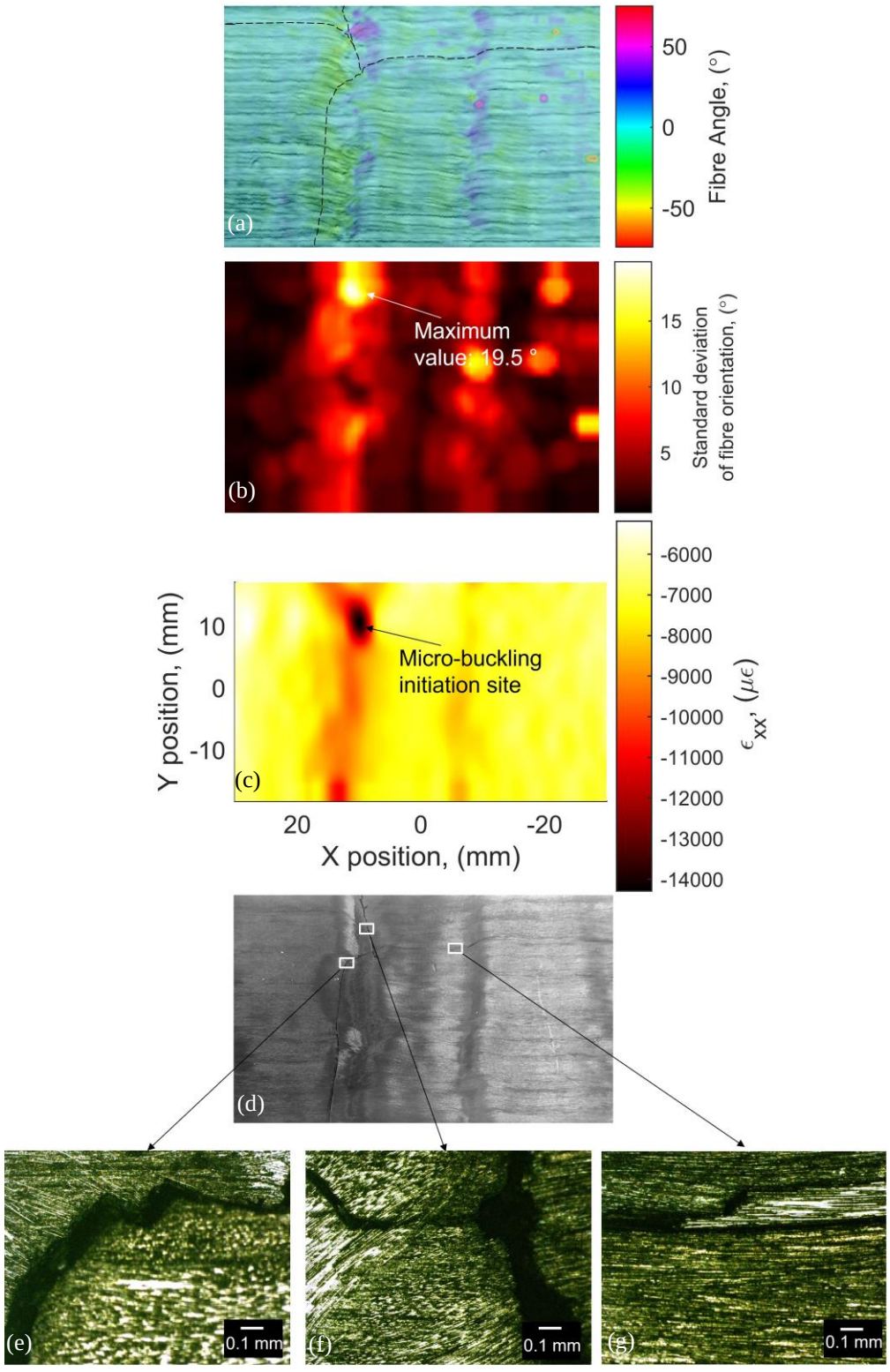

Figure 45: A fibre orientation map obtained using ultrasonic C-scan for a specimen contained 25% fibre waviness with black dashed lines showing crack propagation paths (a), standard deviations of fibre orientations at every facet based on meshing the fibre orientation map into a number of facets with a facet size of 45 pixels (b), the compressive strains in the x-direction on the top surface indicating the location of micro-buckling (c), the specimen with white paint removed (d), optical micrographs showing damage in fine detail at three locations (e)~(g).

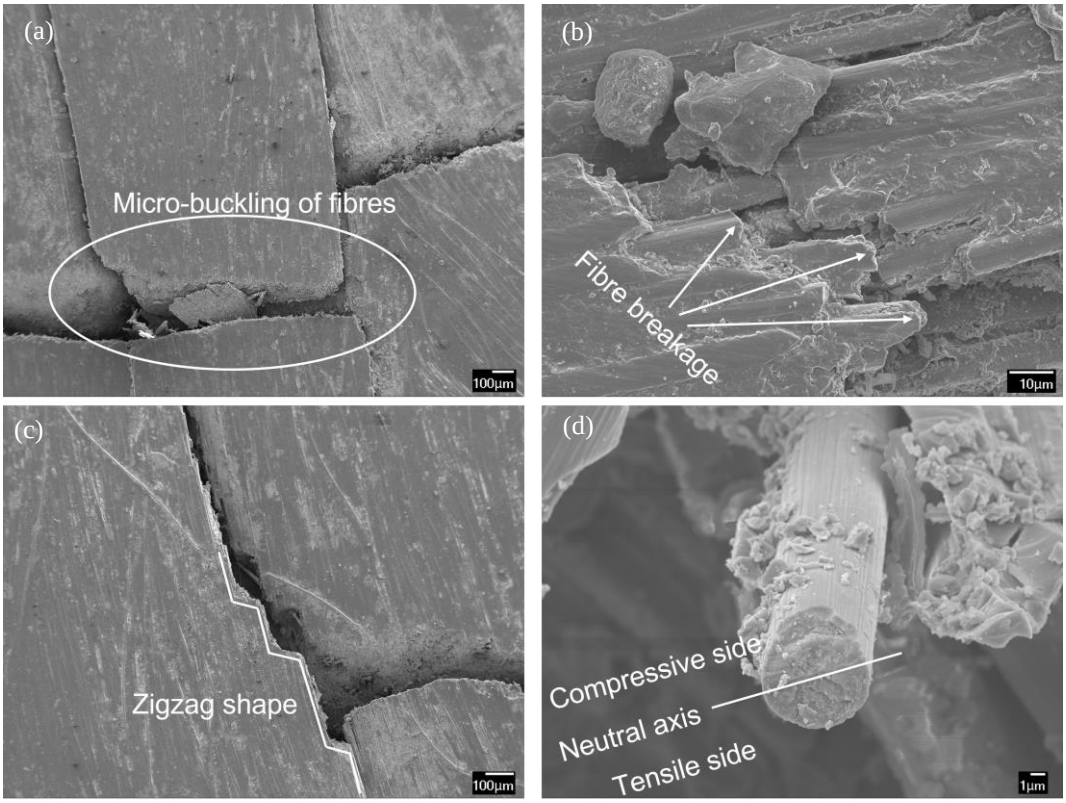

Figure 46: SEM characterisation of fracture surfaces of a specimen containing 25% fibre waviness, showing micro buckling of fibres (a), fibre breakage (b), jagged shape of a mix of fibre damage and matrix damage (c), morphology of a single broken fibre (d).

6.4.4 Finite element analysis

The prediction of failure was performed by simulating a four-point bending test using finite element analysis and the results are shown in Figure 47 to Figure 50. The results of prediction for specimens contained 0% and 20% fibre waviness were similar. Figure 47 (top) shows the predicted delamination behaviour for a specimen containing 0% fibre waviness. It is shown that the predicted delamination only occurred between the top first and second ply, which agreed well with the post-damage photo of the specimen in Figure 47 (bottom).

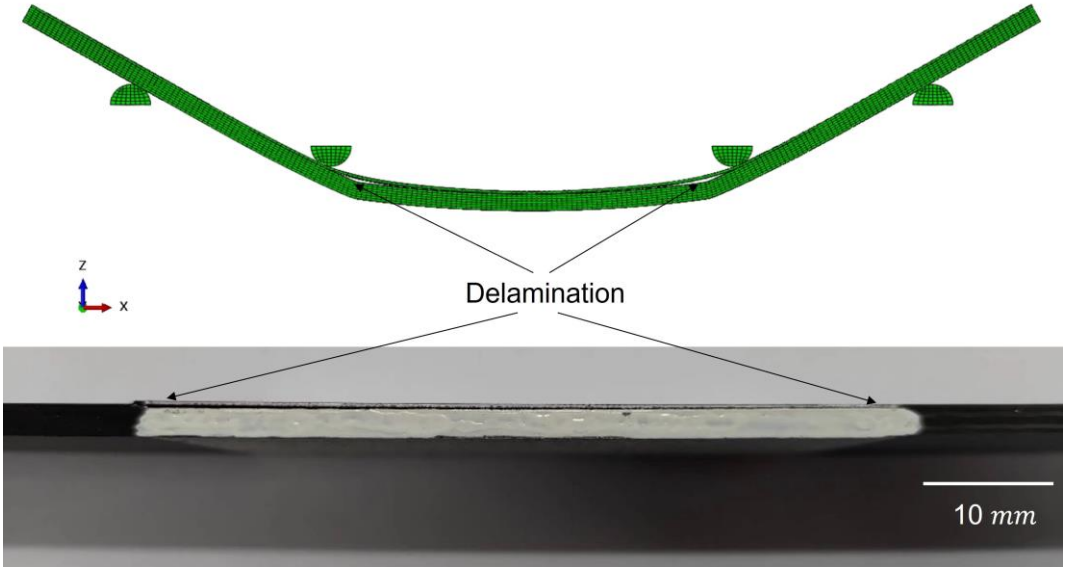

Figure 47: Prediction of delamination for a specimen containing 0% waviness (top) and the post-damage picture of the delamination (bottom).

The predicted failures for specimens contained 25% and 30% fibre waviness were similar. Figure 48 to Figure 50 are the results from simulations based on the fibre orientation map shown in Figure 34 for a specimen containing 30% fibre waviness. Figure 48 (top) shows the predicted morphology of the top surface of the specimen. The appearance of the predicted deformation is similar to the damage visible in camera images at the first ply failure, as shown in Figure 48 (bottom). Figure 49 (top) shows the values of the fibre damage indicator signifying the occurrence of micro buckling, where 0 means no damage and 1 means damaged. In comparison with the fibre damage, when the micro buckling of fibres occurred, the matrix remained undamaged, as shown by the values of matrix damage indicator in Figure 49 (middle). The compressive strains in the x-direction of the top surface of the specimen at the instant when the micro buckling occurred are shown in Figure 49 (bottom). The delamination of the defective top ply was predicted at the first ply failure, as shown by the values of cohesive layer damage indicator in Figure 50 (top). It is apparent that the central region was delaminated because the cohesive layer at this region was damaged. Figure 50 (bottom) shows an unevenly distributed strain map, where higher strains were located at the central region and lower strains located at the two sides. This indicates the occurrence of localised delamination of the central region located just between the two bands of waviness. This implied that the adhesion between plies at the central region was getting weaker than at the edge with the propagation of the initial cracks. In other words, the two bands of

waviness were acting as blockades preventing the delamination propagating from the central to the edge regions.

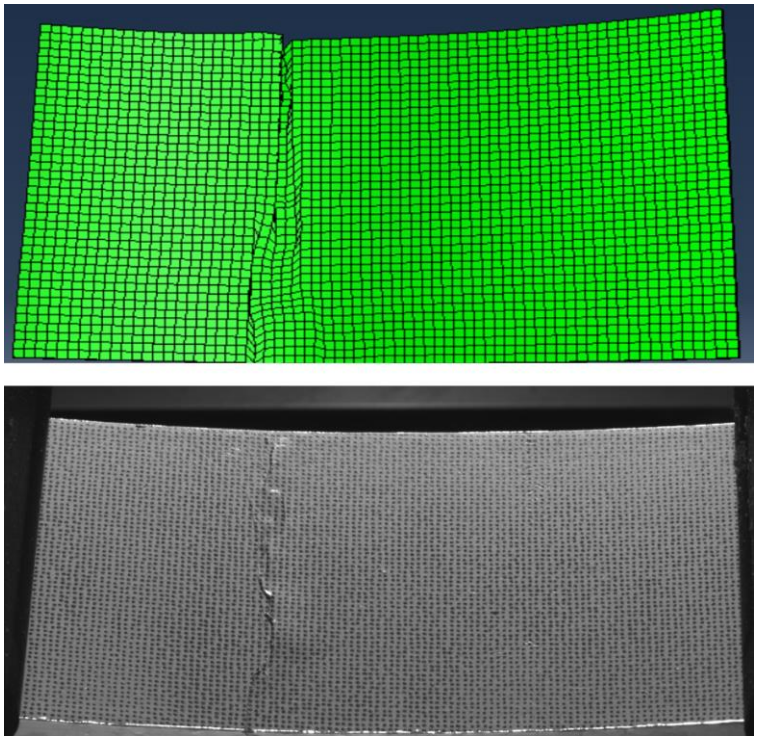

Figure 48: The predicted deformation on the top surface of a specimen containing 30% fibre waviness (top), the real-time image of the top surface of the specimen taken by one of the DIC cameras (bottom) at the first ply failure. The figures show data for the same specimen as in Figure 34.

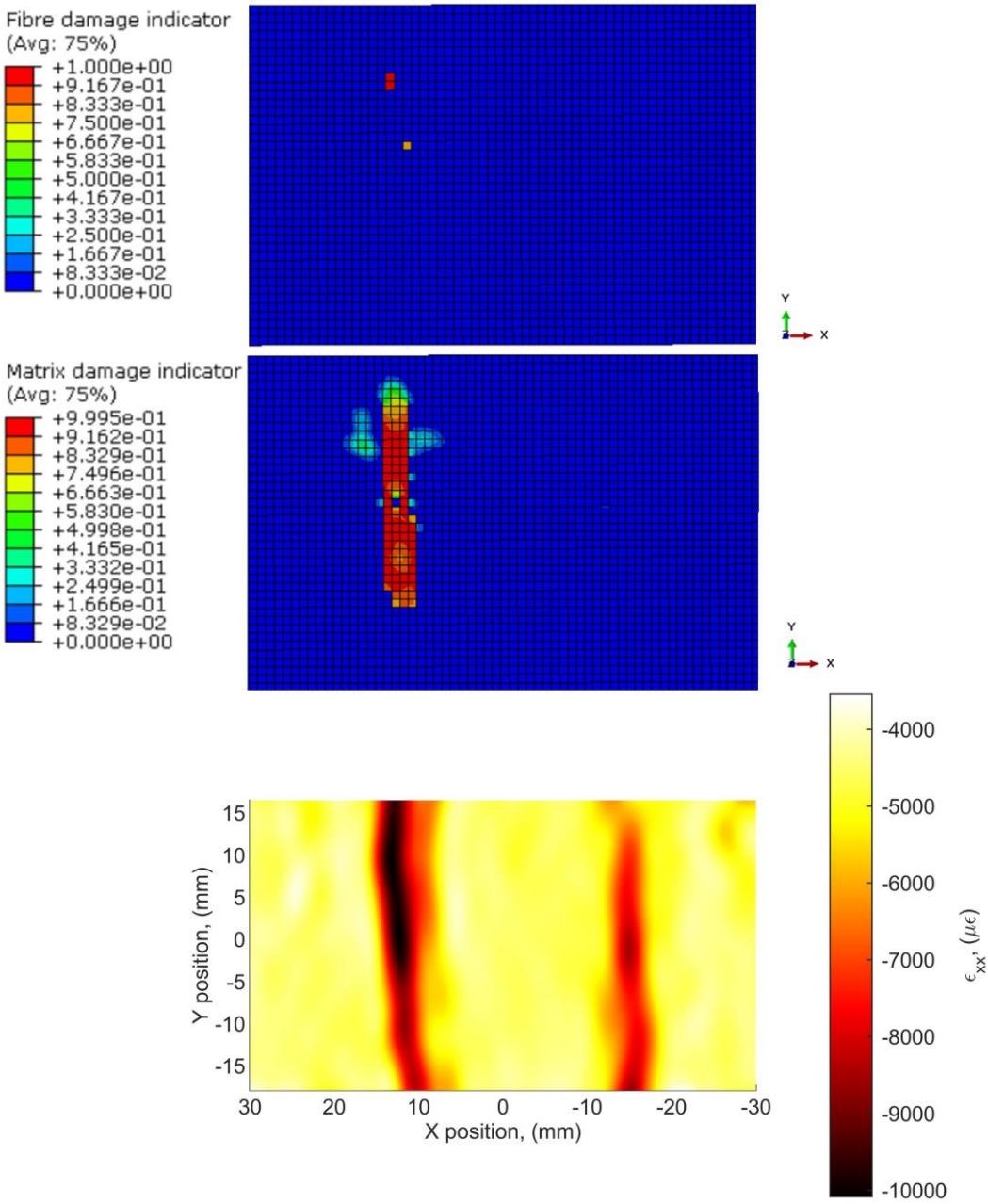

Figure 49: Prediction of fibre damage showing values of the fibre damage indicator signifying the damage status, where 0 means no damage and 1 means damaged (top); prediction of matrix damage with values of matrix damage indicator showing its damage status (middle); the corresponding compressive strains in the x-direction on the top surface (bottom) when the micro buckling of fibres occurred. The figures show data for the same specimen as in Figure 34.

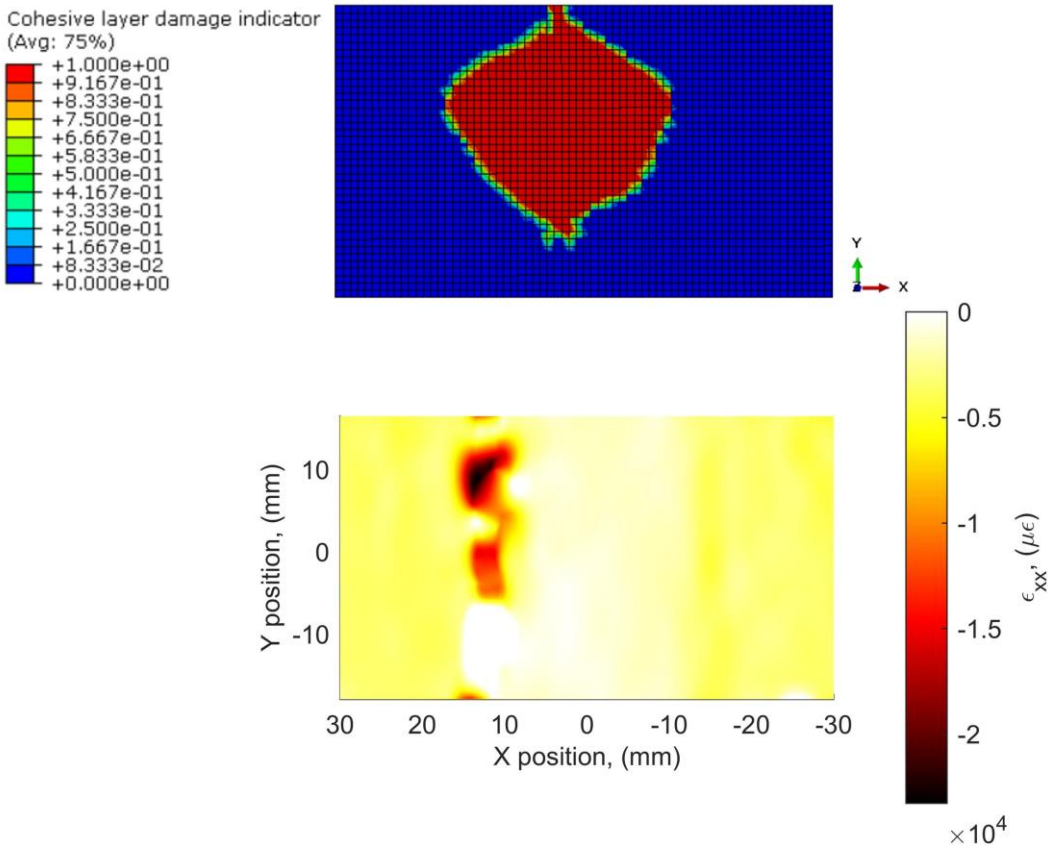

Figure 50: Prediction of delamination, showing the damage status of the cohesive layer between the top first and second ply on the compressive side (top); the corresponding compressive strains in the x-direction on the top surface (bottom). The figures show data for the same specimen as in Figure 34.

6.5 Discussion

The ability of the CFRP specimens to carry a bending load was affected by the existence of in-plane fibre waviness. Although the fibre waviness induced in the study in this chapter was located only at the central region on the top ply, the overall effect on the ultimate bending moment at the first-ply failure was significant. The mean ultimate bending moment decreased with the increase in severity of fibre waviness, as shown in Figure 37. However, there was a drastic decrease in the mean ultimate bending moment in specimens with 30% waviness. This implies that the CFRP specimen with the highest amount of fibre waviness was much weaker and damage propagated earlier. The error bars in Figure 37 also show a decreasing trend with the increase of waviness severity. The error bars were calculated based on the standard error of the bending moments at first-ply failure for every six specimens having the same amount of fibre waviness. This means that specimens with a lower amount of fibre waviness tend to have a larger standard deviation for the ultimate bending moment, while specimens with higher levels of fibre waviness have a smaller standard deviation. One

possible reason for this phenomenon is that when specimens had lower levels of fibre waviness, delamination was the dominant failure type. The initiation of delamination could occur in any region on the compressive side that is weak. However, for a specimen with 0% waviness, the weaker location was distributed stochastically thus the potential site for the initiation of delamination was random. Therefore, the initiation of delamination on specimens with 0% waviness depends on how precisely the specimens were manufactured and whether they have microscopic defects. The severity of these microscopic defects is uncontrollable thus the initiation instant of the first damage is uncertain. The randomness of initiation site of delamination meant the specimens with 0% waviness had the largest standard deviation of ultimate bending moment. When it comes to 30% fibre waviness, although the first damage changed to micro buckling of fibres rather than delamination, the initiation of the damage always occurred at the location having the largest standard deviation of fibre orientations, as shown in Figure 45(b). The initiation site of the damage and the initiation instant thus became more consistent. It can therefore be concluded that the higher the fibre waviness, the clearer will be the initiation site of the first damage, and it is more predictable when the first damage would occur. This explains why specimens with 30% waviness had the lowest standard deviation of ultimate bending moment.

It should be noted that there is a threshold level of in-plane waviness that changed the failure behaviour. In this chapter, this threshold value is between 20% and 25%. Below this threshold level of waviness, the failure progression was in the form of a delamination that occurred between the first and second ply on the compressive side. Above this threshold level of waviness, the failure progression was micro buckling of fibres that occurred first and led to in-plane cracks, then the cracks propagated transversely through the width (y-direction, that is perpendicular to the x-direction and the thickness direction) of the specimen along the waviness band, and longitudinally (x-direction) through the length of the specimen along fibre directions, as shown in Figure 45(a) and (d). The propagation of the cracks led to other types of damage including fibre breakage, matrix damage, and local delamination. It seems like the standard deviation of fibre orientation in a local region governs the initiation of micro buckling, as shown in Figure 45(b). Specimens having lower levels of waviness did not have a weaker site within the defective ply that can cause micro buckling of fibres, thus the in-plane failure would not happen and only interlaminar failure occurred. It should be noted that for

specimens with 25% and 30% fibre waviness, the maximum fibre angles were not always located at the initiation site of micro buckling. This means that the first damage was not governed by the maximum fibre angles, the same phenomenon was reported in [60]. In [60], it was found that the first damage was controlled by other waviness parameters. However, in this chapter, it has been clarified that the micro buckling of fibres was linked to the variation of fibre orientation within a local region. The variation of fibre orientation was characterized by calculating the standard deviation of fibre orientations within local square regions with a side length of 45 pixels, equalling 4.5 mm. It was shown that the micro buckling initiated exactly in the region with the maximum standard deviation, as shown in Figure 45(b) and (c). There were two bands of fibre waviness across the width of the specimen having 25% and 30% waviness defects, as shown in Figure 34 and Figure 45(a).

DIC was used to monitor and record the gradual change in strains on the top and bottom surface, and was shown to be a powerful technique that revealed the failure type and progression. It was observed that with increasing bending load, there was a drastic decrease in compressive strains on the top ply, as shown in Figure 39 and Figure 41. The decrease in compressive strains was as large as 93%, indicating that there was a large amount of strain energy released. The loss of strain energy was replaced by surface energy, which was generated by creating more surfaces in the specimen. The creation of surfaces was achieved by cracks either propagating between the first and second ply on the compressive side, also known as delamination, or propagating within a ply. There was a small decline in tensile strain on the bottom ply, which was also compensated by the crack propagation on the opposite side. Apart from the delamination failure in the specimen with 0% and 20% waviness defect, one of the big achievements in this chapter was that the micro buckling initiation and the resulting crack growth was successfully captured by DIC for specimens with high levels of waviness, as shown in Figure 43 and Figure 44. The micro buckling of fibres appeared as tiny bumps on the top surface of the specimen. After reaching the limit of the compressive strength of the fibres, the bumps broke in half and resulted in cracks, as shown in the micrographs in Figure 45(f) and Figure 46(a). These cracks then propagated in two directions: one along the waviness band across the width of the specimen, and the other one along the fibre direction along the length of the specimen. However, no matter which direction the cracks propagated, the paths were not perfectly straight. There were bifurcations in the paths

which formed jagged shapes, as shown in Figure 45(d) to (g) and Figure 46(c). These jagged shapes show a mix of fibre damage and matrix damage, indicating a quick shift between the two types of damage during the propagation of cracks. The fracture energy for fibre damage and matrix damage is different, resulting in a difference in relationship between force and displacement for fibre and matrix. Therefore, this likely corresponds to the jagged curve in Figure 38 (right). In comparison, for the delamination dominant failure, only matrix failure occurred between the first and second ply on the compressive side. Therefore, there is not any jagged sections in the force versus displacement curve in Figure 38 (left). Carbon fibres are more prone to compressive failure than tensile failure, which is due to their compressive strength being much smaller than the tensile strength, as shown in Table 3. Therefore, when a carbon fibre failed because of a compressive force, a characteristic fracture surface was formed showing half of the surface to be compressive face while the other half to be tensile, as shown in Figure 46(d).

Finite element models incorporating Hashin-Rotem criterion [68] and cohesive layer modelling were successful in predicting the failure type and progression for specimens with various level of fibre waviness. The prediction for a delamination dominant failure is shown in Figure 47. Both the prediction and the post-mortem image show that only the first ply on the compressive side delaminated. The prediction for the micro buckling cases are shown in Figure 48 to Figure 50. In Figure 48, the prediction of the deformed shape agrees well with the deformed shape captured by one of the DIC cameras. In Figure 49, at the time when micro buckling occurred, it is shown that fibres were damaged first at the more severe waviness band, as indicated by the fibre damage indicator with values of 1. While at this instant, matrix was about to damage but did not, as indicated by the matrix damage indicator with values less than 1. These predictions were consistent with the results from DIC and micrographs obtained from optical microscopy and SEM. The delamination was also predicted at the correct location compared with the strain map from DIC, as shown in the central region in Figure 50. However, the prediction is a little conservative in predicting the delamination, because the local delamination area is smaller than that shown in the strain map.

Although the failure modes, failure progression, damage locations and damage shapes have been successfully predicted, the FE models lack quantitative validations with the experimental data. This could be done by comparing the strains obtained from predictions

and experiment using the image decomposition technique described in [82]. However, because the property inputs to the FE models were from literature, they may not represent the real conditions in tests described in this Chapter. Future work needs to focus on either performing experiments to obtain the required properties, or using computational intelligence techniques, such as particle swarm optimisation, to optimise the known properties from literature [108].

The ultimate bending moment can be obtained from the four-point bending test and predicted by the FE models. As reported in [7], residual strains caused by in-plane fibre waviness was shown to be capable of predicting remnant strength of composites. In their research, a method has been established for predicting the ultimate bending moment from experimentally obtained residual strains using DIC. However, prediction of residual strains by FE models has also been made possible in this thesis, which is based on characterisation of in-plane waviness using ultrasonic C-scan data, as introduced in Chapter 4. It is thus applicable to use the predicted residual strains to predict failures in this Chapter. Since failure predictions were also performed by simulating the four-point bending tests, there will be two routes to predict the ultimate bending moment. It would be interesting to investigate the prediction accuracy of the two methods. However, this can only be explored when the property input for simulating the four-point bending test has been calibrated in the future.

6.6 Summary

In-plane fibre waviness affects failure behaviour of CFRP specimens under a bending load. There was a threshold level of waviness defect between 20% and 25% that divided the failures into two types. One was delamination dominant failure for specimens below the threshold level. The other type was a progression of micro buckling first, then cracks propagating through the specimen causing fibre damage, matrix damage, and local delamination around the waviness regions. The mean ultimate bending moment of the specimens with the same level of fibre waviness decreased with increasing fibre waviness. The mean ultimate bending moment to initiation of failure decreased by 32% for specimens having 30% waviness when compared with specimens containing no waviness. The standard deviation of the level of waviness also decreased with the increase of fibre waviness due to the reason that specimens with higher waviness had more severe weak regions and these were found to cause the first damage.

The DIC technique was shown to be effective for revealing the failure type and progression of damage in CFRP specimens. The drastic decline in compressive strains on the top surface of specimens with 0% and 20% waviness indicated the occurrence of delaminations. The micro buckling initiation and the resultant crack growth causing fibre damage, matrix damage and local delamination were all revealed in the strain maps obtained from DIC for specimens with 25% and 30% fibre waviness. The real-time images captured by the DIC cameras confirmed the corresponding failure features in the strain maps. It was found that the micro buckling of fibres did not necessarily occur at the location with the maximum fibre angle, but at a region with the maximum standard deviation of fibre orientations within the region.

Finite element models incorporating Hashin-Rotem criterion [68] and cohesive layer modelling were successful in predicting the two types of failure behaviours. Prediction for global delamination, fibre damage and matrix damage agreed well with the experimental data. One limitation is that the models are conservative in predicting the local delamination for specimens with higher levels of waviness. Quantitative validation of the models needs to be performed in the future work.

7. Discussion

The aim of the thesis was to develop experimental and numerical techniques to improve the detection, characterisation, and assessment of defective composites, with the focus on a particular type of defect: fibre waviness. To achieve this aim, three objectives were set:

- Develop a non-destructive technique for identifying and quantifying the severity of defects in composites.
- Develop a method for better utilising non-destructive evaluation data for characterising defects in composites.
- Enhance the assessment of the performance of defective composite components subjected to loads.

This chapter discusses the findings in Chapter 4, 5, and 6, and their contributions to complete the objectives. Future work is also suggested at the end of the chapter, which could be used to further improve the assessment of defective CFRP composites.

7.1 Quantifying the severity of defects in CFRP composites

Identification of defects in CFRP composites is indispensable for ensuring the safety of components in industry. However, for some defects, such as fibre waviness, quantification of the severity of the defect is more important because a criterion needs to be set to decide which level of fibre waviness is acceptable. Considering fibre waviness is an inevitable defect that is induced at the processing stage of laminates, it would be more helpful if the severity of the defect can be assessed at this stage prior to the next level of manufacturing. In other words, assessing parts is less costly than assessing an assembled component, and discarding disqualified parts is also a more economical choice than discarding a whole component. However, current non-destructive testing techniques, such as ultrasonic inspection, eddy current testing, and X-ray computed tomography, are not capable of performing fast on-site inspections. Ultrasound inspection requires a relatively smooth surface to couple transducers. Eddy current testing and X-ray computed tomography are more likely to be used in laboratories rather than in industry. Additionally, these three non-destructive techniques face some common challenges such as signal attenuation and scattering, difficulty in inspecting thick components, interpretation of large amounts of data and lacking standards for

acceptance or rejection. The last challenge should especially be considered for fibre waviness, as it is still an issue to decide whether an area of unavoidable fibre waviness is below a tolerable level. A technique based on AF-ESPI is developed in this thesis for identifying defects and quantifying their severities, an acceptance or rejection criterion thus could be created based on design criterion. The quantification was achieved by comparing the fringe patterns obtained from defective specimens and defect-free specimens at their resonant frequencies, and the difference was quantified using a specially developed algorithm for processing the patterns. The fringe patterns represented mode shapes, which were only affected by the stiffness and density distribution of the laminates. Considering the minor changes in fringe patterns caused by fibre waviness still resulted a significant differences, as shown in Figure 12 and Figure 19 respectively, it is likely that the technique developed in this thesis is applicable to the other types of defects. The assessment of the severity of fibre waviness produced by the other non-destructive testing methods are mostly based on measuring the maximum fibre angle or amplitude and wavelength of the sinusoidal functions representing the waviness shape. However, these methods are not suitable for waviness with complex morphology. Compared with these non-destructive testing techniques, the technique developed in this thesis can reveal the effect of fibre waviness and quantify the severity. Furthermore, the invisible defects such as voids, delamination, and inclusions that cannot be seen from outside and are difficult to detect by other non-destructive testing techniques, could still potentially be detected by the proposed AF-ESPI technique. This is because these invisible defects would cause a change in stiffness and density distribution, which could lead to a change in mode shapes. Therefore, it has a potential for fast on-site inspections during the fabrication of laminates, regardless of the challenges that the other non-destructive testing techniques are facing. It could be foreseen from Chapter 4 that different levels of fibre waviness will generate different values associated with the severity of the waviness defects. It is also known that residual strains caused by fibre waviness can be used to estimate the remnant strength of composites [7]. Therefore, combining the AF-ESPI based technique with the method developed in [7], it is possible to create a model that can link the quantified defects with the remnant strength. Acceptance or rejection decisions can thus be made based on the predicted remnant strength from the quantified detection of defects. Therefore, the quantification of the severity of defects makes the technique a possible choice for establishing

industrial safety standards. The first objective of this thesis thus has been completed by developing the AF-ESPI based technique.

7.2 Improvement of utilisation of ultrasound data

Although the AF-ESPI based technique is able to identify the waviness defect and quantify its severity, it cannot provide the morphology of the defect. The technique works for evaluation of product quality, but from the perspectives of designing and failure analysis, it may not be suitable. The AF-ESPI based technique could be used to identify damage, but ultrasound inspection can characterise the damage in detail. Therefore, pulse-echo ultrasonic inspection was used to characterise the geometric shape of fibre waviness. Pulse-echo ultrasonic inspection is capable of generating a full-field map of 3D fibre orientation of a component being scanned. For the experiments in this thesis, the orientation data was used in two ways. Firstly, it was used to correlate the residual strains with the misalignment of fibres, and also used as an input to finite elements models for the prediction of residual strains, which has been discussed in Chapter 5. Secondly, the orientation map was used to analyse the failure behaviours and as an input into finite element models for the failure predictions, as discussed in Chapter 6. The geometric shape of fibre waviness plays an important role in governing the performance of laminates, therefore improving the accuracy of their characterisation is crucial. Ultrasonic C-scan data is presented as a 2D image containing fibre tow features. Current algorithms for processing ultrasonic C-scan images are the fast Fourier transformation and the Radon transformation, which can be used to calculate the dominant orientation in an image. It is assumed that the fibre orientation in a very small region of the ultrasonic C-scan image is uniform, therefore the dominant orientation in this region can be obtained using the fast Fourier transformation or the Radon transformation. By repeatedly applying the algorithms at every location in the ultrasonic C-scan image, a fibre orientation map can be obtained. This small region is known as a facet and its size is an important parameter that influences the resolution of the orientation map. However, no prior study has investigated the effect of the facet size on the results, and whether one algorithm outperforms than the other when measuring the fibre orientation. In this thesis, stratified leave-one-out cross validation (SLOOCV) was used to select the optimal facet sizes for the three algorithms: the Radon transformation, the fast Fourier transformation and the Sobel filters. The selection was based on the best matching between measured residual strains with

predictions using two algorithms with different facet sizes. Image decomposition based on Chebyshev polynomials was used to reduce data dimensionalities and make the quantitative comparisons between predictions and experimental data. The results show that the Radon transformation using a facet size of 45 pixels performed best in predicting the measured residual strains, as shown in Figure 27. This is the first time that the facet size was systematically investigated when applying the Radon transformation to process ultrasound data. The results also show that the Radon transformation outperformed the fast Fourier transformation and Sobel filters in revealing the fibre orientations, as shown in Figure 30. The utilisation of ultrasound data thus has been improved by selecting the parameters and algorithms that can provide the best characterisation results.

Residual strains were considered to be correlated strongly with the ultimate strength of defective laminates with in-plane fibre waviness [7]. The measurement of residual strains can be performed by either using strain gauges or non-contact techniques, for example, DIC used in this thesis. However, no prediction of residual strains has been made for defective laminates with waviness defects. This is because the characterisation of waviness defects with complex shapes is not easy. With the improvement in the utilisation of ultrasound data, prediction of residual strains has been made possible, which could lead to higher fidelity predictions of failure. Therefore, the second objective of this thesis has been completed.

7.3 Enhancement of failure assessment

The issue of damage growth in defective CFRP composites containing fibre waviness has been largely neglected. This is due to the fast-propagating damage being difficult to detect, and the characterisation of fibre waviness is also difficult. Although some attempts have been performed using high speed cameras to capture the failure process, the relationship between structural integrity and failure progression is still lacking. Fibre waviness is considered to be one reason for stress concentration, and also the cause of initiation of damage. With the improvement in the characterisation of waviness defects, the damage initiation and propagation were linked with the misalignment of fibres. It has been found that there exists a threshold level of fibre waviness that divides the failure behaviours into two types. The first type is delamination dominant, and the second type is the progression of micro buckling causing in-plane fibre damage, in-plane matrix damage and local delamination. This finding suggests that as long as the in-plane waviness is below the threshold level,

designers should be cautious about the delamination between a defective ply with in-plane waviness and non-defective plies. For the cases when the in-plane waviness is above the threshold level, strengthening strategies should be applied on the surface to prevent the micro buckling of fibres, for example, a patch repair.

The DIC system used in Chapter 6 had cameras with relatively high frame rates and was demonstrated to be effective in detecting the initiation and propagation of damage. Although DIC coupled with high-speed cameras is popular nowadays in analysing transient processes, for example, during impact tests, it may not be suitable for this thesis. This is because the average loading time for specimens subjected to four-point bending tests was about 10 minutes. If high-speed cameras were used, and the frame rate was set to a higher value, for instance 20,000 fps, it will generate thousands of terabytes of data. It is impractical to analyse such a large amount of data in this thesis. However, standard cameras were used with the frame rate set to 20 fps. This still enabled DIC to capture all types of failure occurring in the defective laminates with in-plane fibre waviness, and even the initiation and propagation of micro buckling. In Chapter 6, two DIC systems were set up to capture the failure events on the top and bottom face of the specimen. The setup is different from a recent study [59] when cameras focused on the edges of specimens to capture the delaminations starting from edges. This is because the author expected that in-plane fibre waviness would cause in-plane damage first. With this DIC setup the delaminations were still captured by observing the drastic decrease in strains, as shown in Figure 39 and Figure 41. The failure progression was also successfully captured, from initiation of cracks caused by micro buckling in the waviness regions, to the propagation of the cracks causing fibre failure, matrix failure and local delamination, as shown in Figure 44. A substantial contribution has been made to the third objective by discovering the two failure modes based on the waviness severity and by tracking the initiation and growth of micro buckling.

7.4 Future work

To fully examine the ability of the AF-ESPI based technique to identify defects and quantify severities, more specimens with various types of defects and with different levels of severity should be manufactured and tested. The defects encountered commonly in industry but were not test in this thesis are voids, delamination, and out-of-plane fibre waviness. Low percentages of voids can test the detectability of the technique to the limit as the change of

the stiffness and density caused by small amounts of voids would be negligible. Therefore, it would be interesting to see if the technique can overcome this challenge. Besides testing on other defects, there is also an improvement needed in the design of the experimental setup. The current experimental setup included obtaining the resonant frequencies first using the hammer-based impact tests, then obtaining the mode shapes using the AF-ESPI based technique. The setup could be redesigned to be an automated system using a loudspeaker to replace the hammer and shaker, which can make the technique fully contact-free.

A DIC system with appropriate settings of camera angles and frame rate was shown to be able to capture the failure behaviour of specimens with various severities of fibre waviness. For specimens with lower level of fibre waviness, i.e., 0% and 20%, delamination was dominant. However, the onset of delamination was not captured by the DIC systems. This is because that the breakage of the bond between the two plies was faster than fibre damage and matrix damage, therefore the onset and growth of delamination occurred in such a short time that it exceeded the capture rate of the cameras. The onset and growth of delamination could be captured with high-speed cameras instead, because the frame rate can be as high as 1,000,000 fps to capture such a quick process.

The finite element models created in Chapter 6 could be further validated by comparing the predicted strains with the measured strains obtained from DIC. Image decomposition based on Chebyshev polynomials could be used to make quantitative comparisons. However, the strains predicted by using the current FE models during the bending tests did not agree well with the measurements from DIC analysis. The models could be improved by calibrating the material properties input into the FE models. Optimisation algorithms could be used to achieve the desired property input, such as particle swarm optimisation, simulated annealing or genetic algorithm. The calibration of material properties could minimise the discrepancy between the prediction and experimental data, which could lead to an optimised set of properties that meet an acceptance criterion. Then an assessment of the calibration of properties could be achieved using algorithms such as stratified leave-one-out cross validation introduced in Chapter 5.

8. Conclusions

Carbon fibre reinforced polymers have been widely used in the aerospace industry due to their high stiffness and strength. However, the performance of the materials is affected by defects induced during the processing stage. Traditional non-destructive testing techniques are able to detect the defects and provide the geometric shapes for further analysis, but they face some challenges in providing quantitative detection results rapidly. This thesis developed an AF-ESPI based technique that detected in-plane fibre waviness and quantified the severities efficiently. The technique has the potential for fast on-site inspections for detecting defects and quantifying their severities in industry. Despite having a low efficiency in detecting defects, ultrasonic C-scan can provide fibre orientation data for failure analysis and finite element modelling. However, the utilisation of ultrasound data depends on the effectiveness of the processing algorithms. This thesis compared the performance of three algorithms for processing the ultrasound data and developed a method based on stratified leave-one-out cross validation for selecting the best algorithm and the optimal parameters. This thesis also predicted the residual strains using finite element models based on the characterisation of fibre waviness using ultrasonic C-scan. Image decomposition based on Chebyshev polynomials was used to compare the predictions with experimental data. The failure behaviour of defective specimens with in-plane fibre waviness was experimentally investigated using two DIC systems. The failure modes for different level of in-plane fibre waviness were discovered and the failure progression was captured. The influence of in-plane fibre waviness on the load carrying ability of composites was also investigated. Predictions of the failure events were performed using finite element models based on processing the ultrasonic C-scan data.

Major contributions to knowledge have been presented in this thesis. Two journal papers covering the contributions have been published: [109] and [110]. A further paper based on Chapter 6 is planned. The major contributions are as follows:

A technique for identifying the defects and quantifying the severity based on AF-ESPI and modal analysis has been developed. The technique included using hammer-based impact tests to obtain resonant frequencies. Then the mode shapes were obtained at these resonant frequencies for defective and defect-free specimens. The difference in mode shapes

between the defective and defect-free specimens was quantified, which enabled the identification of the defects. It was also found that the effect of waviness defects on the resonant frequencies was not significant. This work has been published in *Optics and Lasers in Engineering* [110].

A technique for selecting the most effective algorithm and the optimal parameters for processing ultrasound data has been developed, which can be used to generate fibre orientation maps to investigate failure behaviours of composite components subjected to load and create finite element models to predict the performance of the components. This technique was based on comparing the measured residual strains obtained from DIC analysis with the predicted residual strains obtained from finite element analysis. The finite element models were created based on the characterised fibre orientation data using three algorithms with different facet sizes. By applying the algorithm based on stratified leave-one-out cross validation and using image decomposition to make quantitative comparisons, the Radon transformation with a facet size of 45 pixels was shown to provide the best predictions. The technique is thus useful in providing the best algorithm in analysing the ultrasound data to provide fibre orientation maps for further analysis. This work has been published in the *Journal of Nondestructive Evaluation* [109].

An investigation on the failure behaviour of defective specimens with various level of in-plane fibre waviness has been performed. Four-point bending tests were performed to load the specimens to the first-ply failure. A threshold level of fibre waviness that divided the failure into two types was discovered, which was found to be between 20% and 25% of nominal waviness. Below the threshold value, the failure type was delamination dominated. Above the threshold micro buckling of fibres occurred first in the defective ply at the waviness band with the more severe misalignment, then propagated through the ply causing fibre breakage and matrix damage, and propagated along the ply interface causing local delaminations. The failure progression was successfully captured using two DIC systems taking measurements from both the top and bottom faces of specimens with the frame rate of the cameras setting to 20 fps. The variation of fibre orientations has a significant influence on the initiation site of micro buckling, with the location having the maximum standard deviation of fibre orientations found to be more prone to micro buckling.

Overall, this thesis improves the detection, characterisation, and assessment of defects in composites. Specifically, this thesis provides a method that could quantify the risks of defective components by providing the detection of defects quantitatively; this thesis develops an approach to better utilise non-destructive characterisation data to reveal the deviations of components from their initial design; this thesis presents a failure analysis of composites subjected to loads to exploit the capability of the stereoscopic DIC technique in providing transient details of failure events to reveal the failure mechanisms. More importantly, this thesis could help decision makers in industry to develop strategies to determine the necessity of repairs and replacement of composite components.

References

1. Games S, inventor; Owens Illinois Glass Co, assignee. Method and apparatus for making glass wool. United States. 1933.

2. Bunsell AR, Harris B. Hybrid carbon and glass fibre composites. Composites. 1974;5(4):157-64.

3. Mehdikhani M, Gorbatikh L, Verpoest I, Lomov SV. Voids in fibre-reinforced polymer composites: A review on their formation, characteristics, and effects on mechanical performance. Journal of Composite Materials. 2019;53(12):1579-669.

4. Liu SK, Sun W, Jing H, Dong ZX. Debonding Detection and Monitoring for CFRP Reinforced Concrete Beams Using Pizeoceramic Sensors. Materials. 2019;12(13).

5. Krishnamoorthy A, Mercy JL, Vineeth KSM, Salugu MK. Delamination Analysis of Carbon Fibre Reinforced Plastic (CFRP) Composite plates by Thermo graphic technique. Materials Today-Proceedings. 2015;2(4-5):3132-9.

6. Kimura M, Watanabe T, Takeichi Y, Niwa Y. Nanoscopic origin of cracks in carbon fibre-reinforced plastic composites. Scientific Reports. 2019;9.

7. Christian WJR, DiazDelaO FA, Atherton K, Patterson EA. An experimental study on the manufacture and characterization of in-plane fibre-waviness defects in composites. Royal Society Open Science. 2018;5(5).

8. Wang W-C, Su C-W, Liu P-W. Full-field non-destructive analysis of composite plates. Composites Part A: Applied Science and Manufacturing. 2008;39(8):1302-10.

9. Gibson RF. Principles of Composite Materials Mechanics. 2 ed. Boca Raton: CRC Press; 2007.

10. Kulkarni P, Mali KD, Singh S. An overview of the formation of fibre waviness and its effect on the mechanical performance of fibre reinforced polymer composites. Composites Part A-Applied Science and Manufacturing. 2020;137.

11. Potter KD. Understanding the origins of defects and variability in composites manufacture. ICCM International Conferences on Composite Materials. 2009.

12. Parlevliet PP, Bersee HEN, Beukers A. Residual stresses in thermoplastic composites - A study of the literature - Part I: Formation of residual stresses. Composites Part A-Applied Science and Manufacturing. 2006;37(11):1847-57.

13. Pottavathri SB. Effect of in-plane fibre tow waviness in the strength characteristics of different fibre reinforced composites. Kansas, United States: Wichita State University; 2015.

14. Bogetti TA, Gillespie JW, Lamontia MA. Influence of Ply Waviness on the Stiffness and Strength Reduction on Composite Laminates. Journal of Thermoplastic Composite Materials. 1992;5(4):344-69.

15. Hsiao HM, Daniel IM. Elastic properties of composites with fibre waviness. Composites Part A: Applied Science and Manufacturing. 1996;27(10):931-41.

16. Garnich MR, Karami G. Finite Element Micromechanics for Stiffness and Strength of Wavy Fibre Composites. Journal of Composite Materials. 2004;38(4):273-92.

17. Zhu J, Wang J, Zu L. Influence of out-of-plane ply waviness on elastic properties of composite laminates under uniaxial loading. Composite Structures. 2015;132:440-50.

18. Lee SK, Kim MW, Park CJ, Chol MJ, Kim G, Cho J-M, et al. Effect of fibre orientation on acoustic and vibration response of a carbon fibre/epoxy composite plate: Natural vibration mode and sound radiation. International Journal of Mechanical Sciences. 2016;117:162-73.

19. Kumar Samal P, Pruthvi IS, Suresh BS. Effect of fibre orientation on vibration response of glass epoxy composite beam. Materials Today: Proceedings. 2021;43:1519-25.

20. Chan WS, Wang JS. Influence of Fibre Waviness on the Structural Response of Composite Laminates. Journal of Thermoplastic Composite Materials. 1994;7(3):243-60.

21. Wu C, Gu Y, Luo L, Xu P, Wang S, Li M, et al. Influences of in-plane and out-of-plane fibre waviness on mechanical properties of carbon fibre composite laminate. Journal of Reinforced Plastics and Composites. 2018;37(13):877-91.

22. Sitohang RDR, Grouve WJB, Warnet LL, Koussios S, Akkerman R. An experimental approach to reproduce in-plane fibre waviness in thermoplastic composites test coupons using a reverse forming method. Journal of Composite Materials. 2021;56(4):561-74.

23. Yurgartis SW. MEASUREMENT OF SMALL-ANGLE FIBRE MISALIGNMENTS IN CONTINUOUS FIBRE COMPOSITES. Composites Science and Technology. 1987;30(4):279-93.

24. Creighton CJ, Sutcliffe MPF, Clyne TW. A multiple field image analysis procedure for characterisation of fibre alignment in composites. Composites Part A-Applied Science and Manufacturing. 2001;32(2):221-9.

25. Sutcliffe MPF, Lemanski SL, Scott AE. Measurement of fibre waviness in industrial composite components. Composites Science and Technology. 2012;72(16):2016-23.

26. Kratmann K, Sutcliffe M, Lilleheden L, Pyrz R, Thomsen O. A novel image analysis procedure for measuring fibre misalignment in unidirectional fibre composites. Composites Science and Technology. 2009;69(2):228-38.

27. Yoshimura A, Hosoya R, Koyanagi J, Ogasawara T. X-ray computed tomography used to measure fibre orientation in CFRP laminates. Advanced Composite Materials. 2016;25(1):19-30.

28. Schmidt C, Schultz C, Weber P, Denkena B. Evaluation of eddy current testing for quality assurance and process monitoring of automated fibre placement. Composites Part B: Engineering. 2014;56:109-16.

29. Mizukami K, Mizutani Y, Todoroki A, Suzuki Y. Detection of in-plane and out-of-plane fibre waviness in unidirectional carbon fibre reinforced composites using eddy current testing. Composites Part B: Engineering. 2016;86:84-94.

30. Li X. Eddy Current Techniques for Non-destructive Testing of Carbon Fibre Reinforced Plastic (CFRP) [Dissertation]: University of Manchester; 2012.

31. Smith RA, Nelson LJ, Mienczakowski MJ, Challis RE. Automated analysis and advanced defect characterisation from ultrasonic scans of composites. Insight. 2009;51(2):82-7.

32. Smith RA, Nelson LJ, Xie N, Fraij C, Hallett SR. Progress in 3D characterisation and modelling of monolithic carbon-fibre composites. Insight. 2015;57(3):131-9.

33. Kratmann KK, Sutcliffe MPF, Lilleheden LT, Pyrz R, Thomsen OT. A novel image analysis procedure for measuring fibre misalignment in unidirectional fibre composites. Composites Science and Technology. 2009;69(2):228-38.

34. Ayres C, Bowlin GL, Henderson SC, Taylor L, Shultz J, Alexander J, et al. Modulation of anisotropy in electrospun tissue-engineering scaffolds: Analysis of fibre alignment by the fast Fourier transform. Biomaterials. 2006;27(32):5524-34.

35. Hughes RR, Drinkwater BW, Smith RA. Characterisation of carbon fibre-reinforced polymer composites through radon-transform analysis of complex eddy-current data. Composites Part B-Engineering. 2018;148:252-9.

36. Schaub NJ, Kirkpatrick SJ, Gilbert RJ. Automated Methods to Determine Electrospun Fibre Alignment and Diameter Using the Radon Transform. BioNanoScience. 2013;3(3):329-42.

37. Yang X, Ju B-f, Kersemans M. Ultrasonic tomographic reconstruction of local fibre orientation in multi-layer composites using Gabor filter-based information diagram method. NDT & E International. 2021;124.

38. Sutton MA, Wolters WJ, Peters WH, Ranson WF, McNeill SR. Determination of displacements using an improved digital correlation method. Image and Vision Computing. 1983;1(3):133-9.

39. Pan B, Dafang W, Yong X. Incremental calculation for large deformation measurement using reliability-guided digital image correlation. Optics and Lasers in Engineering. 2012;50(4):586-92.

40. Schreier H, Orteu J-J, Sutton MA. Image Correlation for Shape, Motion and Deformation Measurements. New York: Springer; 2009.

41. Catalanotti G, Camanho PP, Xavier J, Dávila CG, Marques AT. Measurement of resistance curves in the longitudinal failure of composites using digital image correlation. Composites Science and Technology. 2010;70(13):1986-93.

42. Godara A, Raabe D. Influence of fibre orientation on global mechanical behavior and mesoscale strain localization in a short glass-fibre-reinforced epoxy polymer composite during tensile deformation investigated using digital image correlation. Composites Science and Technology. 2007;67(11-12):2417-27.

43. Sun CT. Delamination Behaviour of Composite. New York: Woodhead Publishing; 2008.

44. Sun XC, Hallett SR. Failure mechanisms and damage evolution of laminated composites under compression after impact (CAI): Experimental and numerical study. Composites Part A: Applied Science and Manufacturing. 2018;104:41-59.

45. Wykes C. Use Of Electronic Speckle Pattern Interferometry (ESPI) In The Measurement Of Static And Dynamic Surface Displacements. Optical Engineering. 1982;21(3).

46. Yang L, Xie X, Zhu L, Wu S, Wang Y. Review of electronic speckle pattern interferometry (ESPI) for three dimensional displacement measurement. Chinese Journal of Mechanical Engineering. 2014;27(1):1-13.

47. Leendertz JA. Interferometric displacement measurement on scattering surfaces utilizing speckle effect. Journal of Physics E: Scientific Instruments. 1970;3(3):214-8.

48. Coggrave CR. Wholefield Optical Metrology: Surface Displacement Measurement. 2002.

49. Moore AJ, Tyrer JR. Two-dimensional strain measurement with ESPI. Optics and Lasers in Engineering. 1996;24(5-6):381-402.

50. Zhang ZY, Richardson MOW, Wisheart M, Tyrer JR, Petzing J. ESPI non-destructive testing of GRP composite materials containing impact damage. Composites Part A: Applied Science and Manufacturing. 1998;29(7):721-9.

51. Pagliarulo V, Palummo R, Rocco A, Ferraro P, Ricciardi MR, Antonucci V. Evaluation of delaminated area of polymer/Carbon Nanotubes fibre reinforced composites after flexural tests by ESPI. 2014 IEEE Metrology for Aerospace (MetroAeroSpace); Benevento, Italy: IEEE; 2014.

52. Romero G. Study of a vibrating plate: comparison between experimental (ESPI) and analytical results. Optics and Lasers in Engineering. 2003;40(1-2):81-90.

53. Wang W-C, Hwang C-H, Lin S-Y. Vibration measurement by the time-averaged electronic speckle pattern interferometry methods. Appl Opt. 1996;35(22):4502-9.

54. Dai X, Shao X, Geng Z, Yang F, Jiang Y, He X. Vibration measurement based on electronic speckle pattern interferometry and radial basis function. Optics Communications. 2015;355:33-43.

55. Wang W-C, Hsu J-S. Investigation of vibration characteristics of bonded structures by time-averaged electronic speckle pattern interferometry. Optics and Lasers in Engineering. 2010;48(10):958-65.

56. Davies GAO, Olsson R. Impact on composite structures. The Aeronautical Journal. 2016;108(1089):541-63.

57. Mukhopadhyay S, Jones MI, Hallett SR. Compressive failure of laminates containing an embedded wrinkle; experimental and numerical study. Composites Part A: Applied Science and Manufacturing. 2015;73:132-42.

58. Mukhopadhyay S, Jones MI, Hallett SR. Tensile failure of laminates containing an embedded wrinkle; numerical and experimental study. Composites Part A: Applied Science and Manufacturing. 2015;77:219-28.

59. Sitohang RDR, Grouve WJB, Warnet LL, Akkerman R. Effect of in-plane fibre waviness defects on the compressive properties of quasi-isotropic thermoplastic composites. Composite Structures. 2021;272.

60. Sitohang RDR, Grouve WJB, Warnet LL, Wijskamp S, Akkerman R. The relation between in-plane fibre waviness severity and first ply failure in thermoplastic composite laminates. Composite Structures. 2022;289.

61. Jenkin CF. Report on Materials of Construction Used in Aircraft and Aircraft Engines. London: H. M. Stationery Off.; 1920.

62. Waddoups ME. Advanced Composite Material Mechanics for the Design and Stress Analyst. Ft. Worth, Texas; 1967.

63. Hill R. A theory of the yielding and plastic flow of anisotropic metals. Proceedings of the Royal Society of London Series A Mathematical and Physical Sciences. 1948;193(1033):281-97.

64. Tsai SW. Strength Theories of Filamentary Structures Fundamental Aspects of Fibre Reinforced Plastic Composites. New York: Wiley-InterscienE; 1968.

65. Azzi VD, Tsai SW. Anisotropic strength of composites. Experimental Mechanics. 1965;5(9):283-8.

66. Tsai SW, Wu EM. A General Theory of Strength for Anisotropic Materials. Journal of Composite Materials. 1971;5(1):58-80.

67. Tsai SW, Hahn HT. Introduction to Composite Materials. 1980.

68. Hashin Z, Rotem A. A Fatigue Failure Criterion for Fibre Reinforced Materials. Journal of Composite Materials. 1973;7(4):448-64.

69. Kaddour AS, Hinton MJ. Maturity of 3D failure criteria for fibre-reinforced composites: Comparison between theories and experiments: Part B of WWFE-II. Journal of Composite Materials. 2013;47(6-7):925-66.

70. Santosh KC, Lamiroy B, Wendling L. Dtw–Radon-Based Shape Descriptor for Pattern Recognition. International Journal of Pattern Recognition and Artificial Intelligence. 2013;27(03).

71. Ping Tian D. A review on image feature extraction and representation techniques. International Journal of Multimedia and Ubiquitous Engineering. 2013;8(4):385-96.

72. Susan S, Agrawal P, Mittal M, Bansal S. New shape descriptor in the context of edge continuity. CAAI Transactions on Intelligence Technology. 2019;4(2):101-9.

73. Wang W, Mottershead JE, Sebastian CM, Patterson EA. Shape features and finite element model updating from full-field strain data. International Journal of Solids and Structures. 2011;48(11-12):1644-57.

74. Zhang D, Lu G. Review of shape representation and description techniques. Pattern Recognition. 2004;37(1):1-19.

75. Arbter K, Snyder WE, Burkhardt H, Hirzinger G. Application of affine-invariant Fourier descriptors to recognition of 3-D objects. IEEE Transactions on Pattern Analysis and Machine Intelligence. 1990;12(7):640-7.

76. Kauppinen H, Seppanen T, Pietikainen M. An experimental comparison of autoregressive and Fourier-based descriptors in 2D shape classification. IEEE Transactions on Pattern Analysis and Machine Intelligence. 1995;17(2):201-7.

77. Zhang D, Lu G. A comparative study on shape retrieval using Fourier descriptors with Different shape signatures. Journal of Visual Communication and Image Representation. 2001.

78. Dalitz C, Brandt C, Goebbels S, Kolanus D. Fourier descriptors for broken shapes. EURASIP Journal on Advances in Signal Processing. 2013;2013(1).

79. Patki AS, Patterson EA. Decomposing Strain Maps Using Fourier-Zernike Shape Descriptors. Experimental Mechanics. 2011;52(8):1137-49.

80. Lampeas G, Pasialis V, Lin X, Patterson EA. On the validation of solid mechanics models using optical measurements and data decomposition. Simulation Modelling Practice and Theory. 2015;52:92-107.

81. Sebastian C, Hack E, Patterson E. An approach to the validation of computational solid mechanics models for strain analysis. The Journal of Strain Analysis for Engineering Design. 2012;48(1):36-47.

82. CEN Workshop Agreement 16799:2014 'Validation of computational solid mechanics models'. 2014.

83. Dantec Dynamics | Precision Measurement Systems & Sensors [Available from: https://www.dantecdynamics.com/solutions/stress-strain-espi-dic/digital-image-correlation-dic/dic-standard-3d/].

84. Gonzalez R, Woods R. Digital image processing. 4 ed. New York: Pearson; 2018.

85. Bradley D, Roth G. Adaptive Thresholding using the Integral Image. Journal of Graphics Tools. 2011;12(2):13-21.

86. Ester M, Kriegel HP, Sander J, Xu X. A density-based algorithm for discovering clusters in large spatial databases with noise. Proceedings of the Second International Conference on Knowledge Discovery in Databases and Data Mining. 1996(KDD-96):226-31.

87. Schubert E, Sander J, Ester M, Kriegel HP, Xu X. DBSCAN Revisited, Revisited: Why and How You Should (Still) Use DBSCAN. ACM Transactions on Database Systems. 2017;42(3):1-21.

88. Kauppinen H, Seppanen T, Pietikainen M. An Experimental comparison of Autoregressive and Fourier-based Descriptors in 2-D Shape Classification. IEEE Transaction on Pattern Analysis and Machine Intelligence. 1995;17:201-7.

89. Nelson LJ, Smith RA. Fibre direction and stacking sequence measurement in carbon fibre composites using Radon transforms of ultrasonic data. Composites Part A-Applied Science and Manufacturing. 2019;118:1-8.

90. Timoshenko SP, Woinowsky KS. Theory of Plates and Shells. New York: McGraw-Hill; 1959.

91. Morokov E, Levin V, Chernov A, Shanygin A. High resolution ply-by-ply ultrasound imaging of impact damage in thick CFRP laminates by high-frequency acoustic microscopy. Composite Structures. 2021;256.

92. Sobel I, Feldman G. 'A 3×3 isotropic gradient operator for image processing', presented at the Stanford Artificial Intelligence Project (SAIP), 1968, and referenced in History and Definition of the Sobel Operator, by Irwin Sobel. 2014.

93. Gong WR, Chen JL, Patterson EA. Buckling and delamination growth behaviour of delaminated composite panels subject to four-point bending. Composite Structures. 2016;138:122-33.

94. Barnes JA, Simms IJ, Farrow GJ, Jackson D, Wostenholm G, Yates B. Thermal expansion behaviour of thermoplastic composite materials. Journal of Thermoplastic Composite Materials. 1990;3:66-80.

95. Parlevliet PP, Bersee HEN, Beukers A. Residual stresses in thermoplastic composites-A study of the literature- Part II: Experimental techniques. Composites Part A-Applied Science and Manufacturing. 2007;38(3):651-65.

96. Ran ZG, Yan Y, Li JF, Qi ZX, Yang L. Determination of thermal expansion coefficients for unidirectional fibre-reinforced composites. Chinese Journal of Aeronautics. 2014;27(5):1180-7.

97. Aggarwal CC, Hinneburg A, Keim DA. On the Surprising Behavior of Distance Metrics in High Dimensional Space. Lecture Notes in Computer Science In: Van den Bussche, J, Vianu, V (eds) Database Theory — ICDT 2001. 2001;1973.

98. Linhart H, Zucchini W. Model selection. New York: John Wiley & Sons; 1986.

99. Raschka S, Mirjalili V. Python Machine Learning. Second ed. Birmingham: Packt Publishing Ltd.; 2017.

100. Steele K, Werndl C. Model-Selection Theory: The Need for a More Nuanced Picture of Use-Novelty and Double-Counting. British Journal for the Philosophy of Science. 2018;69(2):351-75.

101. Gao G, An L, Giannopoulos IK, Han N, Ge E, Hu G. Progressive Damage Numerical Modelling and Simulation of Aircraft Composite Bolted Joints Bearing Response. Materials (Basel). 2020;13(24).

102. Dassault Systèmes Simulia Corp. SIMULIA User Assistance 2021. ABAQUS Documentation. 2021.

103. Calvo JV, Feito N, Miguélez MH, Giner E. Modeling the delamination failure under compressive loads in CFRP laminates based on digital image correlation analysis. Composite Structures. 2022;287.

104. Camanho PP, Davila CG. Mixed-Mode Decohesion Finite Elements for the Simulation of Delamination in Composite Materials. NASA/TM. 2002;No. 211737.

105. Benzeggagh ML, Kenane M. Measurement of mixed-mode delamination fracture toughness of unidirectional glass/epoxy composites with mixed-mode bending apparatus. Composites Science and Technology. 1996;56(4):439-49.

106. Camanho PP, Dávila CG. Mixed-mode decohesion finite elements for the simulation of delamination in composite materials. 2002.

107. Mottershead JE, Link M, Friswell MI. The sensitivity method in finite element model updating: A tutorial. Mechanical Systems and Signal Processing. 2011;25(7):2275-96.

108. Marwala T. Finite-element-model updating using computional intelligence techniques: Applications to structural dynamics: Springer; 2010.

109. Li X, Patterson EA, Wang W-C, Christian WJR. Prediction of Residual Strains Due to In-Plane Fibre Waviness in Defective Carbon-Fibre Reinforced Polymers Using Ultrasound Data. Journal of Nondestructive Evaluation. 2022;42(1).

110. Li XN, Sung PC, Patterson EA, Wang WC, Christian WJR. Identification of defects in composite laminates by comparison of mode shapes from electronic speckle pattern interferometry. Optics and Lasers in Engineering. 2023;163.